

Probabilistic Modeling of Shallow Landslides at Regional Scales

Ronda L. Strauch

A dissertation

submitted in partial fulfillment of the
requirements for the degree of

Doctor of Philosophy

University of Washington

2017

Reading Committee:

Ekran Istanbuluoglu, Chair

Jessica D. Lundquist

Daniel Miller

Program Authorized to Offer Degree:

Department of Civil and Environmental Engineering

©Copyright 2017

Ronda L. Strauch

University of Washington

Abstract

Probabilistic Modeling of Shallow Landslides at Regional Scales

Ronda L. Strauch

Chair of the Supervisory Committee:
Associate Professor Erkan Istanbuluoglu
Department of Civil and Environmental Engineering

Mountainous areas are challenging to manage and maintain access due to their remoteness and steep topography. Shifting hydrologic regimes from changing climate are projected to intensify these challenges. Of particular concern are the effects and uncertainties from climate change on hillslope stability that may lead to increased landslides, which adds sediment to streams, elevates flooding, and impacts downstream natural and built resources. This dissertation aimed to improve mapping landslide hazard by integrating process-based and data-driven statistical models. To achieve this, we organized the dissertation into four chapters that begins with motivation and background (Chapter 1) and a climate change vulnerability assessment to access over a large regional area (Chapter 2). Chapter 3 describes a new probabilistic model of shallow landsliding based on a physical model that is coupled with a macro-scale hydrologic model and a soil evolution model explicitly addressing spatial and temporal uncertainty. This physical model is integrated with a statistical model relating observed landslides with local site factors

predisposing a hillslope to fail to produce regional-scale landslide hazards from initiation, transportation, and deposition processes (Chapter 4).

Concerns about hillslope stability were identified during one of the largest climate change adaptation efforts undertaken on federal lands. This effort included a transportation vulnerability assessment conducted with research scientists and federal land managers of two national parks and two national forests in north-central Washington, USA. During this assessment documented in Chapter 2, one of the top four infrastructure sensitivities recognized was increased damage associated with landslides from projected higher winter soil moisture caused by changes in seasonal precipitation and snow accumulation. Numerous strategies were identified to increase resistance and resilience of the transportation system to this impact pathway, including information needs such as “site-specific stability analysis based on soil and geologic information” and “identification of areas sensitive to high landslide frequency.” This dissertation takes on these information priorities by developing regional landslide models and demonstrates the models in one of the four jurisdictions: North Cascades National Park Complex (NOCA), Washington.

Chapter 3 of the dissertation describes our development of a hydro-climatological approach to modeling of regional shallow landslide initiation that integrates spatial and temporal dimensions of parameter uncertainty. The physically-based model estimates annual probability of landslide initiation by solving the infinite slope stability equation coupled to steady-state topographic flow routing using a Monte Carlo approach. The uncertainty of soil depth often ignored in landslide hazard modeling is address by a soil development model, and subsurface flow recharge is

obtained from the Variable Infiltration Capacity macro-scale hydrologic model. Thus, the model design allows for use of future hydrologic projections to estimate changing landslide probability as climate and landscape evolve. The model is available as a component in Landlab, an open-source, Python-based landscape earth systems modeling environment. It is designed to be easily reproduced and applied in various locations utilizing HydroShare cyberinfrastructure; therefore, it can be implemented in the other three federal jurisdictions and elsewhere.

To better understand landslide transport and deposition impacts, we develop empirically-based probability hazard maps from a statistically-derived susceptibility index explained in Chapter 4 of this dissertation. This empirical model integrates the influence of seven site attributes on observed landslides, inventoried by NOCA park personnel, using a frequency ratio approach. The attributes assessed included: elevation, slope, curvature, aspect, land use-land cover, lithology, and topographic wetness index. The physically-based and empirically-based models were then combined to produce an integrated probabilistic map of landslide hazard for initiation, transport, and deposition processes. Thus, these maps identify locations of high and low probability of landslide impacts within the NOCA that can be used by land managers in their design, planning, and maintenance. Improved tools such as these with incorporated uncertainty can be used to reduce system vulnerabilities and lead to adaptations that allow continue use of natural areas with reduced risks.

Dedication

Dedicated to my husband, Bradley Strauch, and
our two lovely daughters Katryn and Kristen for their unending support and love.

Acknowledgements

Graduate school is a tough journey made easier by those around you. I was blessed to have a wonderful committee of experts and motivational mentors: Dr. Erkan Istanbuluoglu, Dr. Jessica Lundquist, Dr. Daniel Miller, Dr. Joseph Wartman, and Dr. Alison Duvall. Certain individuals stand out in encouraging, nudging, and standing by me during my journey: Dave L. Peterson, David Hartwell, Regina Rochefort, and Stuart Paulus. Lastly, I would have never embarked on this adventure if it wasn't for Alan Hamlet, who took a chance on me and created a new road for me to follow.

I am eternally grateful for my fellow students and hydrology postdocs for all their support and friendship, especially Nicoleta Christea, Omer Yetemen, Sai Siddhartha Nudurupati, Christina Bandaragoda, Susan Dickerson-Lange, Chris Frans, Claire Beveridge, Zhuoran Duan, Jimmy Phuong, and Amanda Manaster.

I am grateful to the Northwest Climate Science Center, the National Science Foundation, and National Park Service for the financial support of this research and my development as a researcher. Additionally, I appreciate the support from staff at UW Climate Impact Group (CIG), particularly Amy Snover, Se-Yeun Lee, Guillaume Mauger, Ingrid Tohver, and Robert Norheim who facilitated my growth in understanding climate science.

Published Material

At the time of this writing, Chapter 2 has been published in a peer-reviewed journal, and I would like to acknowledge Springer Netherlands, publisher of *Climatic Change*, for granting permission to reproduce the article in this dissertation.

The citation for this published material is:

Strauch, R.L., Raymond, C.L., Rochefort, R.M. Hamlet, A.F., and Lauver, C. (2015) Adapting transportation to climate change on federal lands in Washington State, U.S.A. *Climatic Change* 130: 185. doi:10.1007/s10584-015-1357-7

Chapter 3 is under review as a discussion paper in *Earth Surface Dynamics*, which is an open access journal and permission to reproduce is included under a Creative Commons 4.0 by-nc-nd license.

Strauch, R., Istanbuluoglu, E., Nudurupati, S. S., Bandaragoda, C., Gasparini, N. M., and Tucker, G. E. (2017) A hydro-climatological approach to predicting regional landslide probability using Landlab, *Earth Surf. Dynam. Discuss.*, <https://doi.org/10.5194/esurf-2017-39>, in review.

Chapter 4 is currently in preparation for submittal to journal.

Table of Contents

List of Figures	xi
List of Tables	xv
Chapter 1. Introduction	1
1.1 Motivation.....	1
1.2 Background.....	2
1.3 Dissertation Structure.....	3
References.....	3
Chapter 2. Adapting transportation to climate change on federal lands in Washington State, U.S.A.	6
Abstract.....	6
2.1 Introduction.....	6
2.2 Approach and methods	8
2.3 Results.....	10
2.3.1 Vulnerability assessment	10
2.3.2 Adaptation.....	15
2.4 Summary and Discussion.....	18
Acknowledgments.....	18
References.....	19
Chapter 3. A hydro-climatological approach to predicting regional landslide probability using Landlab	22
Abstract.....	22
3.1 Introduction.....	22
3.1.1 Geomorphology and Modeling Background	23
3.1.2 Approach Overview	25
3.2 Methodology.....	26
3.2.1 Probabilistic approach to landslide initiation.....	26
3.2.2 Model Development in Landlab	27
3.2.3 Hydrologic Data Processing	29
3.2.4 Soil Depth Evolution Model	30
3.2.5 Reproducibility	31
3.3 Model application	32
3.3.1 Study Area	32
3.3.2 Model Input Fields.....	35
3.4 Results and Discussion	39
3.4.1 Geomorphic Analysis and Soil Evolution.....	39
3.4.2 Probability of Failure	44
3.4.3 Model Evaluation.....	53
3.4.4 Model Limitations.....	57
3.5 Conclusion	57
3.6 Data and Model Availability.....	58
Acknowledgements.....	59
References.....	59
User Manual	68

Chapter 4. A new approach to mapping landslide hazards: integration of statistical and process-based models in the North Cascades of Washington, U.S.A.	84
Abstract	84
4.1 Introduction	84
4.2 Methodology	87
4.2.1 Frequency Ratio	87
4.2.2 Model application	88
4.2.2.1 Study Area	88
4.2.2.2 Study domain and Parameters.....	89
4.3 Results and Discussion	92
4.3.1 Frequency Ratio Analysis	92
4.3.2 Susceptibility Index	96
4.3.3 Model Comparison.....	98
4.3.4 Landslide Hazard Maps	101
4.4 Conclusions	104
Acknowledgements.....	105
References.....	105

List of Figures

Chapter	Page
Figure Number	
Chapter 2	
Figure 2.1. The national forests and national parks that comprise the core of the North Cascadia Adaptation Partnership (NCAP) landscape cover a total land area of 2.4 million ha and are surrounded by several other municipal, state, federal, private, and tribal ownerships.	8
Figure 2.2. Projected shift in watershed basin type in the NCAP landscape from historical (upper panel) to the 2040s (2030-2059) and 2080s (2079-2099) (lower panels). Basins represent the spatial resolution of 10-digit hydrologic unit codes (HUC), or the 5th level watershed classification as delineated by the U.S. Geological Survey. Basin classification is defined by the percent (shown in legend) of cool season (Oct. – Mar.) precipitation captured in the April 1 snow water equivalent (SWE). Future projections were modeled using the A1B emission scenario and an ensemble of 10 GCMs. Inset graph shows the percent of each basin type for each time period.	11
Figure 2.3. Shifting trend in the 100-year flood statistic in watersheds within the NCAP landscape. Flood level is designated as the annual peak flow with an estimated 100-year return frequency (Q100). The flood statistic represents the ratio of Q100 in 2020s, 2040s, and 2080s to historical (1916-2006) levels. Ratios > 1 indicate increasing peak flows in the future (purple). Ratios < 1 indicate decreasing peak flows (beige). Gray lines show roads and trails.	12
Figure 2.4. Kilometers of roads and trails in each hydrologic basin type within the two national parks (a) and two national forests (b) across the NCAP landscape during three time periods: historic, 2040s, and 2080s.	14
Figure 2.5. Percentage change in total soil moisture content on December 1 within the NCAP landscape for 2040s (2030-2059), compared with historical levels (1916-2006), calculated as $[(\text{future} - \text{historical}) / \text{historical}] * 100$ (a) . Average change in date at which 90% of SWE is melted from historical date (upper panel) and the 2040s date compared to historical dates (bottom panels) (b) . Future projections modeled using A1B emission scenario and three model configurations, an ensemble of 10 GCMs and two individual GCMs projecting less warming and drier conditions (PCM1) and more warming and wetter conditions (MIROC 3.2) than ensemble mean. Gray lines show roads and trails.	16
Chapter 3	
Figure 3.1. Workflow for landslide modeling using the Landlab LandslideProbability component. The user creates input parameter fields (purple box). The model driver (gray) imports Landlab, Python libraries, and model parameters fields: instantiates (e.g., create an instance) the RasterModelGrid and the component; and runs utilities and methods of Landlab (blue inside dashed box).	28
Figure 3.2. North Cascades National Park Complex (NOCA) in northern Washington state, U.S.A: (a) 30-m DEM of the domain overlain by debris avalanches and major water bodies; (b) slope derived from DEM; and (c) mean annual precipitation (1981-2010 average) mapped at 800-m resolution from PRISM (PRISM Climate Group, 2004).	34

Figure 3.3. (a) Example debris avalanches (cyan) mapped in three areas within NOCA. Contours are in 100-m intervals. Aerial image source from World Imagery, Esri Inc.; (b) elevation distribution of the relative frequency of mapped debris avalanche source areas (upper 10%); and (c) High elevation rock and glacier mapped surrounding Spiral Glacier in North Cascades showing a bedrock glacier cirque with thin barren soils and moraine deposits (photo by John Scurlock with permission). 35

Figure 3.4. Distributed parameters used in the landslide model over NOCA, including: (a) LULC classified from NLCD (USGS, 2014); (b) root cohesion based on LULC; (c) soil depth from SSURGO; and (d) transmissivity based on SSURGO soil depth. Mapped values in (b) through (d) represent the mode values used in the parameter distributions. Insert shows zoomed-in area with 100 m contours. 38

Figure 3.5. Slope-contributing area (S-CA) plot for North Cascades National Park Complex. Mean S for bins of CA are indicated by blue dots and cyan dots for all cells and debris avalanche (DA) cells, respectively. DA source cells (orange triangles) are the single highest elevation grid cell within mapped debris avalanches (gray). Slope stability curves plot the solution of Eq. (1a) for FS=1, given C^* and $\phi=34^\circ$. Above each curve landscape is unstable for a given C^* . Saturation line (red curve) separates partially saturated areas (left) from saturated areas (right). Vertical lines divide the plot into geomorphic process domains in relation to CA of the landscape (e.g., Montgomery 2001). Cyan horizontal line at 17° generally separates potential landslide dominated areas from fluvial dominated areas. 40

Figure 3.6. Illustration of the soil evolution model run using (a, b) steep slope class and forest vegetation and (c, d) moderately steep slope class and shrub vegetation. (a, c) Modeled mean annual erosion rates plotted with respect to soil depth, along with soil depth histogram for a representative convergent location. (b, d) Temporal evolution of soil depth and FS for a representative convergent location with: (a) $S=40^\circ$ and $Curv=-0.01$; and (b) $S=29^\circ$ and $Curv=-0.01$ 43

Figure 3.7. Relative histograms of soil depths within NOCA: (a) SSURGO-SD and (b) mode of M-SD, with respective spatial mean and coefficient of variation (COV). Example location ($\sim 6 \text{ km}^2$) within NOCA: (c) SSURGO-SD and (d) M-SD. Mapped debris avalanches are outlined in cyan and contours are at 100-m. 44

Figure 3.8. Landslide annual P(F) map for NOCA overlain with mapped debris avalanches for simulations with: (a) SSURGO-SD; (b) M-SD; (c) M-SD LT. Zoomed-in areas are shown for greater detail in the lower panel in the same order and according to number designated. Purple areas are considered chronically unstable and areas excluded from analysis are shown as gray. Contours are at 100 m. Aerial images of zoomed-in areas are provided in Fig. 3. 45

Figure 3.9. Illustration of highly unstable steep areas: (a) High resolution (0.3 m) imagery of a NOCA mountain (World Imagery, Esri Inc.) compared to (b) P(F) simulated by M-SD with mapped debris avalanches. Contours at 100 m. Notice the barren areas below retreating glaciers with high P(F). 46

Figure 3.10. (a) Cumulative distribution and (b) relative frequency of P(F) (bin size $\Delta P(F)=0.025$) mapped over NOCA from Landlab simulations using SSURGO-SD and two M-SD scenarios. Labels indicate dominant controls on the distribution of P(F) in (b). Fraction of area is used for cumulative spatial probability, plotted using the Weibull plotting position. Return Period for landslides are illustrated only for SSURGO-SD. 48

Figure 3.11. Modeled landslide return period simulations with M-SD LT for NOCA overlain with mapped debris avalanches, including zoomed in areas at top for greater detail. Cumulative distribution of return periods for SSURGO-SD, M-SD, and M-SD LT scenarios, plotted on a log-log scale using the Weibull plotting position..... 49

Figure 3.12. S-CA plot colored by the P(F) simulated with from the M-SD LT. Source cells (orange triangles) are the single highest-elevation grid cell within mapped debris avalanches. Comparable to Fig. 5. High probabilities plot over low probabilities. 50

Figure 3.13. Elevation (200 m bands or bin) influence on: **(a)** vegetation cover fraction for NOCA, taken as fraction of vegetation type within each elevation band, **(b)** mean P(F) using SSURGO-SD and two M-SD scenarios, along with compact box-whisker plots for P(F) of M-SD LT scenario where circles-dot symbol represents median (outliers not shown, greater than 1.5 interquartile distance) overlaid with hypsometric curve for NOCA, and **(c)** mean soil depth for SSURGO-SD and M-SD products with mean slope. Mean values calculated within each 200-m elevation band. 52

Figure 3.14. **a)** Relative histogram of source areas in upper 10% elevation of debris avalanches (DAs) and for 50,000 grid cells outside DAs. Cumulative distributions of P(F) plots limited to $P(F) \leq 0.2$, or return period ≥ 5 years, to highlight detail in simulation using SSURGO-SD, M-SD, and M-SD LT at: **b)** low (<1,200 m), **c)** mid (1,200 to 1,800 m), and **d)** high (>1,800 m) elevations as depicted in a). Thicker lines represent probabilities for source areas of (DAs) and thin lines represent probabilities for cells outside DAs. 54

Figure 3.15. **a)** ROC curves and **b)** SR curves for simulations using SSURGO-SD, M-SD, and M-SD long-term (LT). Comparison represent P(F) for the upper 10% of DA as observed landslides to a random sample of 5,000 cells outside DAs. Thresholds for simulated probabilities associated with positive classification of a source areas declines along the curves from lower left to upper right. Black diagonal line on a 1:1 line represents the case of a trivial or random classification model. 56

Chapter 4

Figure 4.1. Primary landslide features showing source, transport, and deposition areas illustrated over aerial image from Google Earth taken July 2016. Location in North Cascades National Park Complex about 4 km north of Newhalem, Washington. 86

Figure 4.2. Four landslide types mapped within North Cascades National Park Complex (NOCA) in Washington, U.S.A. The number and their total area of each type is given in parentheses. Insert provides example of mapping over aerial image from Google Earth..... 90

Figure 4.3. FR value for different bins of seven SAs based on: **a)** all landslide types mapped within the NOCA study domain, **b)** debris avalanche landslide types only, and **c)** source areas of debris avalanches represented by the highest 20% of the mapped debris avalanche. The vertical blue dashed line refers to the FR value of 1.0, denoting when no association is found with mapped landslides 94

Figure 4.4. Vegetation cover fraction in NOCA on each aspect, taken as the fraction of vegetation type within each 200-m elevation band. Aspects categorized here as: **a)** north (0° to 45° and 315° to 360°), **b)** east (45° to 135°), **c)** south (135° to 225°), and **d)** west (225° to 315°), covering 23%, 23%, 26%, and 28% of NOCA, respectively. Yellow highlighted area represents the strongest elevation association for debris avalanche source areas. 95

Figure 4.5. Cumulative distributions (*column 1*) and relative frequency plots (*column 2*) of Susceptibility Index (SI) for all grid cells included in the analysis and the grid cells mapped as part of a mapped landslide. Probability $P(LSr|SIr)$ (*column 3*) calculated from the ratio of the number of landslide cells to the number of all cells with each SI bin (0.5 size) with fitted curves. Rows represent three analyses of mapped landslides: **a)** all landslide types, **b)** debris avalanches only, and **c)** debris avalanche source areas. 97

Figure 4.6. a) Comparison of rescaled $P(LSr|SIr)$ from empirical model for debris avalanche source areas with the mean probability of landslide initiation $P(F)$ from the physical model within 0.5 size bins of SI (rescaled by dividing by maximum). Portion of NOCA showing: **b)** $P(F)$ from physical model; and **c)** same area showing only $P(F)$ corresponding to the two regions of SI (region 1: $SI \leq 9$; region 2: $SI > 9$, depicted in (a)) overlain on hillshade. Location of the portion of NOCA shown as box in Fig. 4.7. 99

Figure 4.7. Comparison of probabilities derived from empirical model for: **a)** all landslide types and **b)** debris avalanches overlain with the average probability from the physical model for grid cells within each 0.5 bins of SI. 100

Figure 4.8. Maps of probability of landslide impact derived from empirical model based on: **a)** all landslide types, **b)** debris avalanches, and **c)** and source areas of debris avalanches. Boxes indicates close-up areas shown below with overlain landslide types on hillshade. Gray areas excluded from analysis. 100

Figure 4.9. Maps of probability of landslide impact based on: **a)** empirical model of all landslide types, **b)** physical model from Strauch et al. (2017), and **c)** integrated model for the North Cascades National Park Complex. Box indicates close-up locations in Fig. 10. Gray areas excluded from analysis and blue areas depict water. 102

Figure 4.10. Section of NOCA showing probability of landslide impact from: **a)** empirical model based on all landslide types, **b)** physical model, and **c)** integrated map derived from highest per pixel value from either empirical model (a) or physical model (b) overlain with mapped landslides; **d)** aerial image sourced from World Imagery, Esri Inc. of same area overlain with landslides. Location shown as box in Fig. 4.9. 103

Figure 4.11. Cumulative distribution of the probability of landslide impact $P(LS)$ for the empirical model using all landslide types (blue), the physical model (black), and the integrated model (red) for: **a)** all grid cells in study domain and **b)** grid cells inside landslides. Data for landslides curve for the physical model in (b) is limited to only debris avalanche source areas. 104

List of Tables

Chapter	Table Number	Page
Chapter 2		
None		
Chapter 3		
Table 3.1. Parameters defined for vegetation and soil types in the study region. For spatially continuous parameters, values represent the statistics for the model domain with (<i>mean</i>) values in parentheses		36
Table 3.2. Model parameters used in the soil evolution model		42
Chapter 4		
Table 4.1. Landslides mapped as part of landform mapping study used in hazard analysis.....		90
Table 4.2. Classification of Washington Department of Natural Resources surface geology from generally weaker (1) to stronger (7) material along with aerial percentages within NOCA in parentheses.....		92

Chapter 1. Introduction

1.1 Motivation

During the past few decades, federal agencies in the United States that manage large areas of land have become increasingly challenged by aging infrastructure and changing environmental conditions along with increased public demands (Raymond et al., 2014; Albano et al., 2014; Peterson et al., 2011). Maintaining access to natural areas of rugged terrain is demanding and hydrologic extremes are a recurrent source of infrastructure damage (Tohver et al., 2014; Meyer 2008; NRC 2008). Uncertainty in how changing climate will alter demands on managing resources and built infrastructure is particularly concerning to agencies (Hayhoe and Kopp 2016; Mauger 2011; Millar et al. 2007). During a workshop with numerous agencies convened to discuss these concerns, managers identified several impacts from climate change potentially affecting their ability to deliver historical benefits and services in the future in Washington state (Strauch et al. 2014). One of the greatest angst among managers was the potential for increased landslides with projected increases in soil moisture (Hamlet et al. 2007), which can have considerable effects to downstream aquatic and built resources (Baum et al., 2008; Istanbuloglu and Brass 2007; Pollock 1998). For example, intense storms in autumn 2003 and 2006 caused flooding and landslides throughout the Washington, leading to millions of dollars in damage to roads and trails and a 6-month closure of Mount Rainier National Park, followed by years of repairs.

In the Western U.S., landslides are a major mechanism of landscape change (Perron 2017). Most landslides initiate on hillslopes, evolve into debris flows, and deliver sediment to streams (Benda and Dunne 1997; Iverson et al 1997). The initiation process is typically controlled by soil and root cohesion, soil internal friction angle, local slope, and subsurface flow pore-pressure. Changes in pore-pressure, typically from heavy or continuous rain and snowmelt, can quickly affect the stability of a slope and have been responsible for triggering more landslides than any other factor (Crozier 1986). Landslide hazards in the Western U.S. are expected to grow with climate change (Coe 2016), but to date, geologic landslide research has been typically conducted independently from hydroclimate research (Corominas et al., 2012; Lee 2005; Chung and Fabbri 2003). Prior research has frequently focused on headwater catchments, and this research's dependence on highly-localized measurements prevents it from being extended to regional and hydroclimate scales. There is need to unify geologic and hydroclimatic research to provide regional-scale landslide prediction for resource management and climate adaptation strategies.

We are frequently faced with situations and choices that involve randomness and uncertainty. We want to make sense of the situation, make better choices, and more clearly understand the world around us. We can't predict uncertain events with certainty, but perhaps we can apply a probability perspective that allows us to understand the uncertainty surrounding us. Whether we're an engineer or scientist, uncertainty plays a role in our understanding, design, and hypotheses. This dissertation seeks to better understand the undefined and changeable phenomenon of landslides, particularly concerning to decision makers. I attempt to shed light and provide insights and tools to help them cope with uncertainty and advance informed judgements, strategies, and policies.

My research focuses on developing a regional-scale distributed numerical model in conjunction with landslide observations across the Washington's North Cascades mountains. North Cascades experience landslides across a wide a range of climates, vegetation, and topography (Mustoe and Leopold 2014). Thus, research in this region is relevant to mountain areas across the globe. The project develops the modeling technology and shows proof-of-concept simulations relevant to addressing management and planning questions. The technology employed in this study advances landslide hazard identification for risk assessments and provides decision support tools for land management over large regions now and into the future. Specific landslide related research questions addressed by this research include the following:

- 1) What are the relative roles of location (geology, topography, slope) vs. climate (recharge rates) on landslide location and relative frequency?
- 2) How well does a new, transformative model combining the methods of geotechnology, geology, and hydroclimate prediction reproduce past spatial-temporal patterns and frequencies of landslides?

1.2 Background

Heightened awareness and concerns regarding potential impacts to built and natural resources from climate change motivates the need for better information on impacts to guide potential adaptations strategies (Snover et al. 2007). Information on where and when impacts may occur is critical. In particular, the propagating effects of climate dynamics on geomorphology through ecohydrology is vital to understand geohazards at management-relevant spatial and temporal scales. Assessing risk and vulnerability begins with understanding the impact and uncertainties. Vulnerability assessments benefit from input from both scientist and managers, which combines theoretical knowledge with institutional knowledge and practices (Wall and Meyer 2014; Mickalak et al. 2013; Peterson et al. 2011). Collaborations among scientist and resource managers can help identify relevant data, specific impacts, and interpret results (Kloprogge and Van der Sluijs 2006). Thus, in the research presented in this dissertation, we worked closely with resource managers to strengthen the source of data, decipher patterns in modeling results, and produce tools and products beneficial to their management directives.

A key challenge in landslide assessments and use by practitioners is the complexity of the assessments themselves: finding and acquiring the relevant data, processing and analyzing the data, mapping and interpreting results, and sharing the results in a format practical for authorities and decision makers. There is a plethora of data available and we have emerged into e-science computationally-intensive environment requiring an integrated cyberinfrastructure to process, collaborate, and share information to better understand complex systems such as hillslope stability (Borgman et al., 2015; Newman et al. 2003). It can be daunting to identify and acquire distributed data on site characteristics, triggering factors, landslide inventories, and elements at risk, especially at a large geographic scale. The isolated, sporadic and relatively small scale of landslides compared to other hazards such as floods, makes an inventory quite tedious, particularly in remote locations (Van Westen et al. 2005). Additionally, science and products based on a finite suite of data in time and space becomes less useful as conditions and theories change. This is true for landslide assessments where the precondition of sites can change due to disturbances such as fire (Luce et al. 2012) and triggers can transform in the case of continued climate change (Crozier 2010). Landslides themselves alter the local hazard. Therefore, a robust landslide model should: (1) be flexible enough to incorporate changes in intrinsic and extrinsic

conditions, such as vegetation and climate; (2) account for spatial variability in model parameters and forcings, (3) integrate spatial and temporal dimensions of uncertainty to quantify landslide probability, and (4) be reproducible and customizable to fit the needs of scientist and managers (Tarboton et al. 2014; Horsburgh et al. 2016).

Land management and regulatory agencies need maps of areas affected by landslides as well as the chances of landslide impacts to consider in project, policies, and decision making, including mitigation and adaptation measures (Corominas et al. 2014). Landslide hazard maps and analyses need to be quantitative to support risk assessments (Van Westen et al. 2005). It is also important to identify impacts from different types of landslides and various components of landslides (i.e., initiation, transport, and deposition). Our modeling approach combines the advantages of empirically-based landslide hazard assessment with the strength of mechanistic, process-based stability analysis typically applied at small scales but driven by the dynamic climatology provided by a macro-scale hydrological model. The aim of this landslide assessment approach is to create a parsimonious model that requires relatively few, broadly available, and spatially distributed input data. Data uncertainty due to spatial and temporal variability of parameters continues to be one of the major challenges in predicting landslides over broad regions (Sidle and Ochiai, 2006; Baum et al., 2014; Anagnostopoulos et al., 2015). To capture uncertainty in these data, we employ a Monte Carlo approach in the physical model and estimate probabilities of landslide impacts, which systematically accounts for uncertainty and variability in stability analysis (Hammond et al., 1992) and more appropriately represents complex systems (Berti et al., 2012).

1.3 Dissertation Structure

My dissertation is structured as three main chapters, following this introduction chapter. The motivation for researching landslide hazards was generated from contemporary concerns about recent damage to transportation infrastructure and potential future escalating damage as climate changes. Chapter 2 details a vulnerability assessment that triggered more in-depth research on landslides from knowledge gained in workshops with federal agencies tasked with managing access to public lands. Chapter 3 takes on the challenge identified in the workshop and develops a physical model of probability of shallow landslide initiation. This model is developed in Landlab, an open-source earth system modeling toolkit, to meet the four objectives of robust landslide model identified above. To address concerns about landslide features other than source areas, Chapter 4 describes an empirical landslide model and how this was integrated with the physical model to produce a probabilistic landslide hazard map for impacts from initiation, transport, and deposition zones.

References

- Anagnostopoulos, G.G., Fatichi, S., and Burlando, P.: An advanced process- based distributed model for the investigation of rainfall- induced landslides: The effect of process representation and boundary conditions, *Water Resources Research*, 51(9): 7501-7523, 2015.
- Albano, C.M., Angelo, C.L., Strauch, R.L., and Thurman, L.L. (2013) Potential effects of warming climate on visitor use in three Alaskan national parks. *Park Sc.* 30(1): 36-44
- Baum, R.L., Galloway, D.L., and Harp, E.L. (2008) Landslide and land subsidence hazards to pipelines: U.S. Geological Survey Open-File Report 2008-1164, 192 pp

- Baum, R.L., Schulz, W.H., Brien, D.L., Burns, W.J., Reid, M.E., and Godt, J.W.: Plenary: Progress in Regional Landslide Hazard Assessment—Examples from the USA, In: *Landslide Science for a Safer Geoenvironment*, Springer International Publishing, 21-36, 2014.
- Benda, L. and Dunne, T.: Stochastic forcing of sediment supply to channel networks from landsliding and debris flow, *Water Resour. Res.* 33(12): 2849-2863, 1997.
- Berti, M., Martina, M.L.V., Franceschini, S., Pignone, S., Simoni, A., and Pizziolo, M.: Probabilistic rainfall thresholds for landslide occurrence using Bayesian approach, *Journal of Geophysical Research* 117:F04006, 2012.
- Borgman, C., Darch, L., Sands, P., Pasquetto, T., Golshan, A., Wallis, E., & Traweek, I. (2015). Knowledge infrastructures in science: Data, diversity, and digital libraries. *International Journal on Digital Libraries*, 16(3), 207-227.
- Chung, C. J. F., & Fabbri, A. G. (2003). Validation of spatial prediction models for landslide hazard mapping. *Natural Hazards*, 30(3), 451-472.
- Coe, J. A. 2016. Landslide hazards and climate change: A perspective from the United States. In: *Slope safety preparedness for impact of climate change*, Chapter: 14. Eds. K. Ho, S. Lacasse, L. Picarelli. CRC Press, Boca Raton, FL. pp.479-523
- Corominas, J., Van Westen, C., Frattini, P., Cascini, L., Malet, J. P., Fotopoulou, S., ... & Pitilakis, K. (2014). Recommendations for the quantitative analysis of landslide risk. *Bulletin of engineering geology and the environment*, 73(2): 209-263.
- Crozier, M. J. (2010) Deciphering the effect of climate change on landslide activity: A review. *Geomorphology*. Vol. 124: 260-267.
- Hamlet, A. F., Mote, P. W., Clark, M. P., & Lettenmaier, D. P. (2007). Twentieth-century trends in runoff, evapotranspiration, and soil moisture in the western United States. *Journal of Climate*, 20(8), 1468-1486.
- Hammond, C., Hall, D., Miller, S., and Swetik, P.: Level 1 stability analysis (LISA), documentation for Version 2.0. USDA, For. Serv., Moscow, ID, Intermountain Res. Sta. Gen. Tech. Rep. INT-285, 1992.
- Hayhoe, K., and Kopp, R. E. (2016). What surprises lurk within the climate system?. *Environmental Research Letters*, 11(12), 120202.
- Horsburgh, J.S., Morsy, M.M., Castronova, A.M., Goodall, J.L., Gan, T., Yi, H., Stealey, M.J., and Tarboton, D. G.: HydroShare: Sharing Diverse Environmental Data Types and Models as Social Objects with Application to the Hydrology Domain, *JAWRA Journal of the American Water Resources Association*, 52(4): 873-889, <http://dx.doi.org/10.1111/1752-1688.12363>, 2016.
- Istanbulluoglu, E., & Bras, R. L. (2006). On the dynamics of soil moisture, vegetation, and erosion: Implications of climate variability and change. *Water Resources Research*, 42(6).
- Kloprogge P, Van der Sluijs, J (2006) The inclusion of stakeholder knowledge and perspective in integrated assessment of climate change. *Climatic Change* 75: 359-389.
- Lee, S. (2005). Application of logistic regression model and its validation for landslide susceptibility mapping using GIS and remote sensing data. *International Journal of Remote Sensing*, 26(7), 1477-1491.
- Luce, Charles; Morgan, Penny; Dwire, Kathleen; Isaak, Daniel; Holden, Zachary; Rieman, Bruce. 2012. Climate change, forests, fire, water, and fish: Building resilient landscapes, streams, and managers. Gen. Tech. Rep. RMRS-GTR-290. Fort Collins, CO: U.S. Department of Agriculture, Forest Service, Rocky Mountain Research Station. 207 p.
- Maurer M, Roalkvam, CL, and Salsibury, SL (2011) Climate Impacts Vulnerability Assessment. Washington State Department of Transportation Report, Olympia, 70 pp
- Michalak J, Withey JC, Lawler JL (2013) Climate adaptation planning for British Columbia provincial parks. Prepared for North Pacific Landscape Conservation Cooperative. University of Washington, Seattle, WA
- Millar CI, Stephenson NL, Stephens SL (2007) Climate change and forests of the future: managing in the face of uncertainty. *Ecol Appl.* 17: 2145–2151

- Mustoe, G. E., & Leopold, E. B. (2014). Paleobotanical evidence for the post-Miocene uplift of the Cascade Range. *Canadian Journal of Earth Sciences*, 51(8), 809-824.
- National Research Council (NRC) (2008) Potential impacts of climate change on U.S. transportation: Special report 290. Transportation Research Board, National Research Council, The National Academies Press, 280 pp
- Newman, H., Ellisman, M., & Orcutt, J. (2003). Data-intensive e-science frontier research. *Communications of the ACM*, 46(11), 68-77.
- Perron, J. T. (2017). Climate and the Pace of Erosional Landscape Evolution. *Annual Review of Earth and Planetary Sciences*, 45(1).
- Peterson DL, Millar CI, Joyce LA, et al (2011) Responding to climate change in national forests: a guidebook for developing adaptation options. Gen. Tech. Rep. PNW-GTR-855. Portland, OR: U.S. Department of Agriculture, Forest Service, Pacific Northwest Research Station
- Pollok, M. M. (1998) Biodiversity, In: R. J. Naiman and R. E. Bilby (eds.) *River Ecology and Management: Lessons from the Pacific Coastal Ecoregion*, pp. 430–452, Springer-Verlag, New York.
- Raymond CL, Peterson DL, Rochefort RM (2014) Climate Change Vulnerability and Adaptation in the North Cascades Region, Washington. Gen Tech Rep PNW-GTR-892. Portland, OR: U.S. Department of Agriculture, Forest Service, Pacific Northwest Research Station
- Snover AK, Whitely Binder L, Lopez J, Willmott E, Kay J, Howell D, and Simmonds J (2007) Preparing for Climate Change: A Guidebook for Local, Regional, and State Governments. In association with and published by ICLEI – Local Governments for Sustainability, Oakland, CA
- Strauch RL, Raymond CL, Hamlet AF (2014) Climate change, hydrology, and access in the North Cascade Range. In: Raymond CL, Peterson DL, and Rochefort RM (eds) *Climate change vulnerability and adaptation in the North Cascade Region*, Washington. Gen Tech Rep PNW-GTR-892. Portland, OR: U.S. Department of Agriculture, Forest Service, Pacific Northwest Research Station
- Suffling R, Scott D (2002) Assessment of climate change effects on Canada's national park system. *Environ Monit Assess.* 74(2):117-139
- Tarboton, D.G., Idaszak, R., Horsburgh, J.S., Heard, J., Ames, D., Goodall, J.L., Band, L., Merwade, V., Couch, A., Arrigo, J., Hooper, R., Valentine, D., and Maidment, D.: *HydroShare: Advancing Collaboration through Hydrologic Data and Model Sharing*, in D. P. Ames, N. W. T. Quinn and A. E. Rizzoli (eds), *Proceedings of the 7th International Congress on Environmental Modelling and Software*, San Diego, California, USA, International Environmental Modelling and Software Society (iEMSs), ISBN: 978-88-9035-744-2, 2014.
- Tohver, I, Hamlet AF, and Lee S (2014) Impacts of 21st century climate change on hydrologic extremes in the Pacific Northwest region of North America. *J Amer Water Resour Assoc* 1-16, DOI: 10.1111/jawr.12199
- Wall T, Meyer M (2014) Risk-Based Adaptation Frameworks for Climate Change Planning in the Transportation Sector. Transportation Research Board of the National Academies, Washington, D.C.

Chapter 2. Adapting transportation to climate change on federal lands in Washington State, U.S.A.

R. L. Strauch¹, C. L. Raymond², R. M. Rochefort³, A. F. Hamlet⁴, and C. Lauver⁵

¹Civil and Environmental Engineering, University of Washington, Seattle, WA, USA

²Environmental Affairs & Real Estate Division, Seattle City Light, Seattle, WA, USA

³North Cascades National Park Service Complex, National Park Service, Sedro-Woolley, WA, USA

⁴Civil and Environmental Engineering and Earth Sciences, University of Notre Dame, Notre Dame, IN, USA (previously at University of Washington, Seattle, WA)

⁵Pacific Northwest CESU, National Park Service, University of Washington, Seattle, WA, USA

Note: This chapter has been published in its current form as an article in Climatic Change (Strauch et al., 2015); the only differences are in the section, figure, and table numbering. It is used here by permission of Springer Netherlands.

Abstract

Research scientists collaborated with federal land managers of two national parks and two national forests to conduct a climate change vulnerability assessment and to identify adaptation strategies for a transportation network covering 28,900 km of roads and trails in north-central Washington, U.S.A. The assessment employed observations of sensitivity and response to climatic variability, downscaled climate projections, literature reviews, current management policies and practices, expert knowledge, and stakeholder engagement. Primary pathways for climate impacts focused on projected increases in extreme high flows and flooding, elevated winter soil moisture and landslide hazards, and loss of snowpack. The biggest impacts to roads and trails are expected from temperature-induced changes in hydrologic regimes that enhance autumn flooding and reduce spring snowpack. Projected higher winter soil moisture caused by changes in seasonal precipitation and snow accumulation could reduce slope stability. Earlier snowmelt may lengthen the snow-free season for visitor use and agency operations. Infrastructure age, design, maintenance, location, use, and limited redundancy along with funding policies and management, influence the sensitivities of the transportation system. Vulnerabilities were identified based on when and where these sensitivities to changes in climate may emerge. Adaptation strategies and tactics identified to address these vulnerabilities included: upgrading stream crossing and drainage design, changing use and maintenance, relocating or closing roads and trails, modifying funding policies, and expanding public engagement. Many adaptation options are “no regrets” approaches to changes in climate projected for the 2040s and 2080s that can be applied to other resource sectors and mountainous regions.

2.1 Introduction

During the past century, roads and trails in the United States in remote locations were built to extract furs, minerals, timber, and energy. Travel along roads and trails is now primarily associated with recreation, and is the principal means by which the public visits the nation’s parks and forests (Louter 2006). Safe and strategic access to and within public lands is vital for facilitating recreational enjoyment, education, managing natural resources, and responding to

emergencies. However, maintaining roads and trails in areas of rugged terrain is challenging, and hydrologic extremes are a recurrent source of infrastructure damage. Climate variability strongly influences the timing and location of land management activities and visitor use. Because climate change has the potential to affect whether or not specific land areas will deliver historical benefits and services in the future, understanding the extent and magnitude of climate change impacts on travel on federal lands is needed to minimize consequences. The U.S. Forest Service (USFS) and National Park Service (NPS) are adapting transportation planning and management activities as part of a broader effort to ensure sustainability (USDI NPS 2010; USDA FS 2010).

A multi-agency partnership was created in 2010 among four federal jurisdictions in Washington State that share common borders and a vision to address climate change impacts that cross jurisdictional boundaries (Raymond et al. 2013, 2014; Strauch et al. 2014). The North Cascadia Adaptation Partnership (NCAP) includes Mount Rainier National Park (MORA), North Cascades National Park Complex (NOCA), Mount-Baker Snoqualmie National Forest (MBSNF), and Okanogan-Wenatchee National Forest (OWNF). These contiguous federal lands occupy over 24,000 km² in north-central Washington and contain 28,900 km of roads and trails (Fig. 2.1). The NCAP landscape is part of the Cascade Range, oriented north to south with high topographic relief (184 m to 4392 m). Mean annual temperatures are similar on both sides of the Cascade Range, but the eastside has higher seasonal variability. Abundant mountain precipitation supports over 67,000 km of streams and rivers and vegetation dominated by coniferous forest, except at the elevation extremes where vegetation transitions to shrubs and meadows.

The NCAP identified climate change effects on the transportation system as a high priority because of recent impacts associated with extreme storms and the importance of access to public lands. For example, intense storms in autumn 2003 and 2006 caused flooding and landslides throughout the NCAP landscape, leading to millions of dollars in damage to roads and trails, a 6-month closure of MORA, followed by years of repairs. Transportation infrastructure is increasingly compromised by interrelated climate change impacts (Schwartz et al. 2014; Maurer et al. 2011). However, adaptation strategies in the transportation sector have received less attention than mitigation for transportation-related greenhouse gas emissions (GHG) emissions (Chapman 2007; NRC 2008). This paper describes a vulnerability assessment that examines transportation adaptation in the context of the NCAP landscape. The context is unique compared to urban and suburban transportation systems because of the multiple federal lands, large contiguous geographic area in rugged terrain, extensive network of mostly dirt roads and trails, and relatively low average daily travel on many routes. Furthermore, there is an emphasis on visitor uses and seasonal access, protection of aquatic species, and maintenance rather than expansion of infrastructure with minimal development pressures.

Mountain ecosystems are acutely sensitive to climate change (IPCC 2007), and some portions of the Pacific Northwest (PNW) are particularly sensitive to climate-induced loss of snowpack and

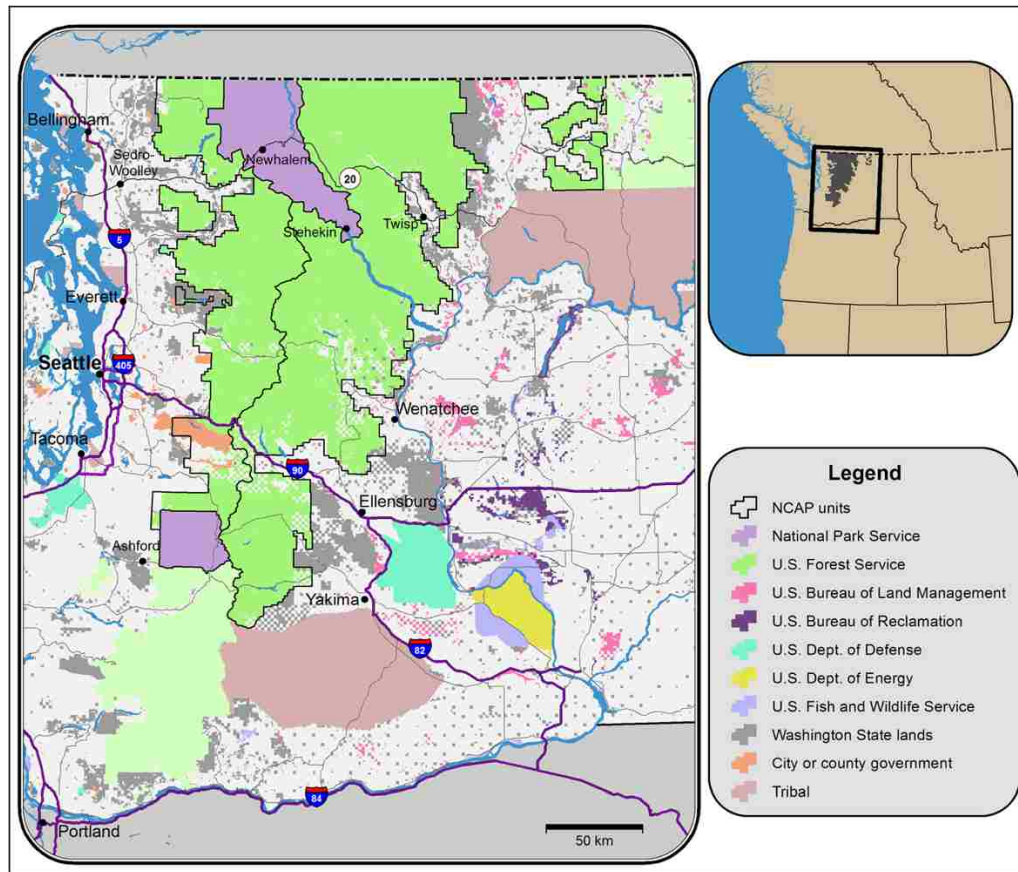


Fig. 2.1 The National forests and national parks that comprise the core of the North Cascadia Adaptation Partnership (NCAP) landscape cover a total land area of 2.4 million ha and are surrounded by several other municipal, state, federal, private, and tribal ownerships

changes in hydrologic regime (Elsner et al. 2010; Mote and Salathé 2010; Hamlet et al. 2013). In the PNW, warming observed over the 20th century (+0.7 °C since 1906) is expected to continue and intensify, with annual average temperatures 3.2 °C warmer by the 2050s compared with historical (1950–1999) averages and greater warming projected later in the century (Snover et al. 2013). Climate models project little change in annual precipitation, but seasonal precipitation is projected to change with more precipitation in autumn, winter, and spring, and less in summer (Mote and Salathé 2010). Precipitation intensity is also projected to increase (Snover et al. 2013). Snowpack is projected to decline further in Washington with reductions in April 1st snow-water equivalent (SWE) of 38 to 46 % by 2040 compared with historical averages (Elsner et al. 2010). Warming and changes in seasonal precipitation in the NCAP landscape generally result in increased soil moisture and streamflow in autumn and winter and higher peak flows (Hamlet and Lettenmaier 2007; Hamlet et al. 2013; Mantua et al. 2010).

2.2 Approach and methods

Collaboration among scientists and agency resource managers is vital to understanding specific impacts on access and to identifying climate change adaptation strategies (Kloprogge and Van der Sluijs 2006). Accordingly, the NCAP held a workshop on climate change, hydrology, and access that convened resource managers, scientists, engineers, and representatives of recreation groups to assess vulnerabilities of access to climatic variability and change (see supplemental).

Resource managers identified impacts of current climate on the transportation system and trends in recent impacts associated with extreme weather and climate change. Scientists supported the vulnerability assessment by focusing on three pathways by which climate change directly influences access in mountain landscapes: (1) extreme high flows and flooding, (2) less snow and extended warm season, and (3) elevated winter soil moisture and landslide hazard. These pathways were considered the most relevant to the NCAP landscape by workshop participants given current impacts and sensitivities, topography, and climate.

Projections of average temperature and precipitation in the vulnerability assessment were generated from an ensemble of 10 global climate models (GCMs) based on the A1B GHG emissions scenario, which aligns with the current emission trajectory (Nakićenović and Swart 2000). Ensemble averages report the central tendency of the projections; two additional GCMs (PCM1 and MIROC 3.2) were used to provide a range of future climates based on variations in model sensitivity from the 10 GCMs. PCM1 simulates relatively lower increases in annual temperature and slightly drier conditions in the PNW for the 2040s (“least warming and drier”). MIROC 3.2 simulates relatively larger increases in annual temperature and wetter conditions (“most warming and wetter”) (Littell et al. 2011). Downscaled projections of temperature and precipitation were applied as monthly changes to meteorological inputs to the Variable Infiltration Capacity (VIC) macroscale hydrologic model (Liang et al. 1994; Elsner et al. 2010). The VIC model implementation provided hydrologic information at 1/16th degree resolution (about 34 km² grid cell), and routed flows were used for projected changes in streamflow (Hamlet et al. 2013; Tohver et al. 2014). Details on these datasets are available in Hamlet et al. (2013) and Littell et al. (2011). Snowpack simulations were available from a high-resolution version of the VIC model implemented at 800-m resolution (Mauger 2011).

In similar studies, extreme flooding was defined as the 100-year flood (the annual peak flow with a 1 % probability of exceedance, or Q100) and changes to Q100 were reported as a ratio of future Q100 to historical Q100 (Tohver et al. 2014). Projections of hydrologic variables were provided for the 2020s, 2040s, and 2080s using GCM statistics from a 30-year time window to generate 91 years of climate-adjusted data (see Tohver et al. 2014). Hydrologic response was characterized by basin type determined from simulated spring snowpack and cool season precipitation (Hamlet et al. 2013): (1) rain-dominant, (2) mixed-rain-and-snow, and (3) snowmelt-dominant, depending on percentage of winter precipitation entrained in spring snowpack (<10 %, 10–40 %, and >40 %, respectively). Although VIC does not simulate slope stability failures or landslides, projections of soil moisture from VIC were used as an indicator of landslide hazard. The PNW typically experiences highest precipitation in November and December, and climate models project increases in future autumn precipitation in Washington (Mote and Salathé 2010). Therefore, the percent change in VIC projections of total column soil moisture on December 1 were used to indicate future slope stability associated with elevated soil moisture (Crozier 1986). To understand the influence of snow on seasonal access, the change in date when 90 % of snow is melted in spring was assessed.

Using these impact pathways and climate projections, scientists, engineers, and resource managers identified vulnerabilities of infrastructure to climate change. Vulnerability was qualitatively determined by the exposure, sensitivity, and adaptive capacity of the transportation system to changing climate. Exposure was determined using spatial data on projected changes in

hydrologic processes relevant to access. Sensitivity was determined by assessing qualities of the transportation system that influence the degree to which it could be affected by climate change, including location, design, use, management, current condition, and recreation patterns. Adaptive capacity was determined by reviewing the ability of current management practices and policies to respond and adjust to the influence of climate. Vulnerabilities were based on expert local knowledge and current climate-related impacts, combined with projections of changes in climate and hydrologic regimes. These vulnerabilities were refined with further literature review, data analysis, and discussions among scientists and agency staff (Snover et al. 2007; Peterson et al. 2011). The assessment process was a first step in identifying vulnerabilities by agencies within NCAP that have limited financial and personnel capacity for climate change planning. Thus, a more parsimonious process was followed similar to Michalak et al. (2013) rather than a prescribed risk management framework often used in the transportation sector (Wall and Meyer 2013; Maurer et al. 2011).

Based on initial vulnerabilities identified at the workshop, participants identified adaptation strategies, and opportunities and barriers to implementing strategies within institutional processes, policies, and practices. Workshop participants focused on three adaptation strategies: 1) creating resistance (i.e., “hardening”), 2) increasing resilience, and 3) enabling systems to respond to a changing climate (Millar et al. 2007). On-the-ground tactics were identified for implementing general strategies. Given current climate change uncertainties and the limited capacity of both agencies for adaptation planning, the group identified “no regrets” actions as likely first steps towards adaptation, but also recognized the value of actions addressing sizeable impacts or reducing long-term consequences. No regrets actions satisfy other agency goals, such as species protection or improved ecological function, with the co-benefit of reducing the impacts of climate change (Peterson et al. 2011).

2.3 Results

2.3.1 Vulnerability assessment

2.3.1.1 Climate change exposure

Flooding in the PNW is a function of precipitation intensity and duration, freezing elevation during storms (which determines where precipitation falls as rain or snow), and effects of temperature and precipitation on seasonal snow and soil moisture (Hamlet and Lettenmaier 2007; Tohver et al. 2014). The flood regime is largely determined by basin types, which are projected to shift as climate changes (Fig. 2.2). Within the NCAP landscape, 26 watersheds are currently rain-dominant basins, containing 19 % of the landscape’s 19,591 km of roads, 34 are currently mixed-rain-and-snow basins with 48 % of roads, and 27 are snowmelt-dominant with 33 % of roads. By the 2040s, the ensemble projections are for equal number (39) of rain- dominant and mixed-rain-and-snow basins; only 9 are projected to remain snowmelt-dominant. Autumn and winter flood hazard in the Cascade Range is projected to increase with more autumn and winter precipitation, coupled with warmer temperatures that raise freezing elevations, effectively increasing basin area during storms (Hamlet and Lettenmaier 2007; Mantua et al. 2010; Tohver et al. 2014). The largest increases in flood hazard are expected in mixed- rain-and-snow basins where current mid-winter temperatures are within a few degrees of freezing (Hamlet et al. 2013; Tohver et al. 2014). Most of the coldest snowmelt-dominant basins at high elevation in the NCAP landscape are expected to continue to experience peak flows in spring, but with smaller and earlier peak flows by the 2040s. Some snowmelt- dominant basins may experience a small

increase in flooding due to more snowpack resulting from persistent cold mid-winter temperatures and more cool-season precipitation.

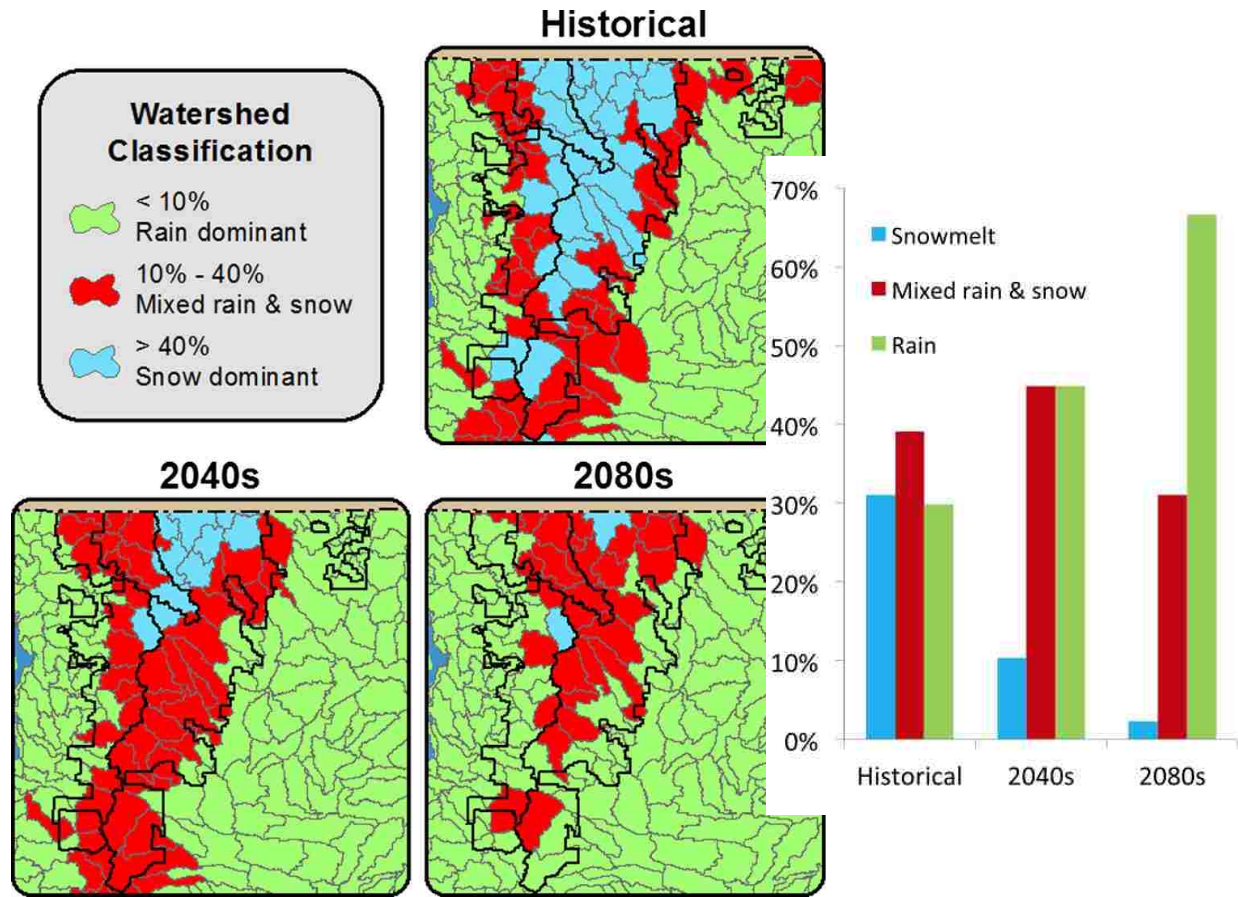


Fig. 2.2 Projected shift in watershed basin type in the NCAP landscape from historical (*upper panel*) to the 2040s (2030–2059) and 2080s (2079–2099) (*lower panels*). Basins represent the spatial resolution of 10-digit hydro-logic unit codes (HUC), or the 5th level watershed classification as delineated by the U.S. Geological Survey. Basin classification is defined by the percent (shown in legend) of cool season (Oct.–Mar.) precipitation captured in the April 1 snow water equivalent (SWE). Future projections were modeled using the A1B emission scenario and an ensemble of 10 GCMs. Inset graph shows the percent of each basin type for each time period

By the 2080s, only two basins within the NCAP landscape may remain snowmelt-dominant, but contain less than 1 % of the roads. Many of the current mixed-rain-and-snow basins may transition to rain-dominant basins in the future, shifting annual peak flows that historically occurred during spring snowmelt to rainy periods in autumn and early winter (Tohver et al. 2014). Extreme floods (e.g., Q100) are also projected to increase throughout much of the NCAP landscape, particularly by the 2080s. The highest increases are projected for the east side of the Cascade crest, where Q100 is projected to be more than double the historical value in several watersheds (Fig. 2.3).

Shifts in basin type and Q100 are expected to alter flood exposure of roads and trails, although the rate and magnitude of change (i.e., road kilometers associated with shifting basin type) and

associated management cost may differ by jurisdiction (Fig. 2.4). For example, 78 % of NOCA roads and 37 % of OWNF roads are currently in snowmelt-dominant basins; however, by the 2080s, all roads are projected to be in mixed-rain-and-snow or rain-dominant basins. The cost associated with altered flood exposure would be greater for OWNF than for NOCA because it contains more roads.

Climate projections support the hypothesis that landslide-triggering conditions may increase in winter because 1) more precipitation is projected to fall as rain rather than snow, 2) soil moisture is projected to increase in winter due to loss of snowpack and increased soil infiltration in autumn and early winter, and 3) increasingly intense winter storms are projected (Salathé et al.

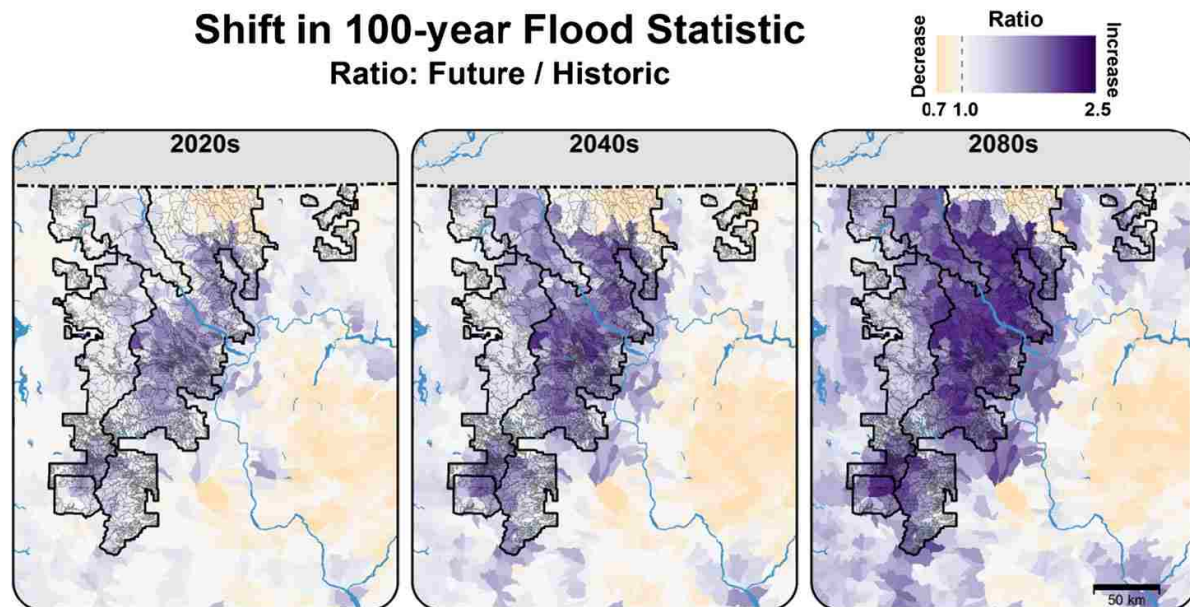


Fig. 2.3 Shifting trend in the 100-year flood statistic in watersheds within the NCAP landscape. Flood level is designated as the annual peak flow with an estimated 100-year return frequency (Q100). The flood statistic represents the ratio of Q100 in 2020s, 2040s, and 2080s to historical (1916–2006) levels. Ratios >1 indicate increasing peak flows in the future (*purple*). Ratios <1 indicate decreasing peak flows (*beige*). *Gray lines* show roads and trails

2014; Hamlet et al. 2013; Dominguez et al. 2012). These effects would likely vary with elevation because higher elevations typically have steeper slopes and more precipitation during storms. By the 2040s, December 1 soil moisture is projected to be higher throughout the NCAP landscape, particularly at higher elevations and in the east central area, which may become more vulnerable to landslides in late autumn and early winter (Fig. 2.5a).

Projected declines in SWE will likely influence the timing of access to mountain roads and trails in the NCAP landscape. Although decadal climatic variability also affects SWE on shorter timescales, April 1 SWE has declined over the 20th century due to observed warming and precipitation change, and is projected to continue to decline (Hamlet et al. 2005; Mote et al. 2008). Throughout the NCAP landscape, the date when 90% of winter snow has melted is projected to be earlier than historical dates, especially west of the Cascade crest and at low elevation (Fig. 2.5b).

2.3.1.2 Climate change sensitivity and impacts

Impacts on access with exposure to climate change, particularly the shifts in hydrologic processes, depend on the sensitivity of the transportation network to these exposures. The condition of roads and trails varies as a function of age, maintenance, surface treatment, and use. Many roads and trails were built decades ago and are near the end of their design life span. Advanced design of materials, alignment, drainage, and subgrade that are required standards today were generally not available when much of the road network was built. New culverts and bridges are often wider or higher (or both) than historical structures to meet hydraulic regulations or more stringent design standards. Consequently, new or replaced infrastructure is likely to be less sensitive to climate change, especially if climate change is explicitly considered in the design.

Lack of redundancy in a transportation network can cause systemic operational sensitivity when damage disconnects critical links in the system. The transportation system in the NCAP landscape lacks redundancy in national parks. Numerous roads and trails, especially at high elevation, provide sole access to recreation areas. Many roads and trails are built on steep slopes or along river corridors, which are sensitive locations impacted by landslides, washouts, and flooding. Management of roads and trails (e.g., planning, funding, maintenance, response) differs by agency, which can affect sensitivity of the transportation system. For example, snow removal operations by one jurisdiction can influence when a road is open, affecting when a connecting road in another jurisdiction can open.

The integrity and operation of the transportation network in the NCAP landscape are affected by stream channel migration and scour, landslides, and debris flows, which make it difficult to maintain fixed crossing structures and operational travel routes near streams. Projected increases in peak streamflows elevate flood risk, and sediment transport increase risks to structures, roads, and trails (MacArthur et al. 2012). Individual intense storms during any season can overwhelm the water-holding capacity of soil and concentrate high velocity flows into channels that erode soils, remove vegetation, and initiate debris flows, which may be particularly pronounced below receding glaciers (Pelto and Riedel 2001; Huggel 2009). During floods, roads and trails can become preferential flow paths for floodwaters. Landslide impacts to infrastructure may expand due to projected changes in soil moisture and precipitation form and intensity, particularly in autumn and winter. Landslide hazard may also increase with tree mortality caused by fire and insect outbreaks because tree mortality reduces root adhesion with soil and decreases interception and evapotranspiration, further increasing soil moisture (Schmidt et al. 2001; Neary et al. 2005; Martin 2006).

Climate change effects on access may create public safety concerns. A longer snow-free season may extend visitor use in early spring and late autumn at higher elevations (Suffling and Scott 2002; Albano et al. 2013). Earlier snowmelt may reduce snow-related closures for a greater portion of the year and allow visitors to reach trails and camps earlier in the spring. Trailheads, which start at lower elevations, may be snow-free earlier, but hazards associated with melting snow bridges, avalanche chutes, and frozen snowfields may persist at higher elevations. In addition, greater variability in cool-season precipitation and increased flooding (Hamlet and

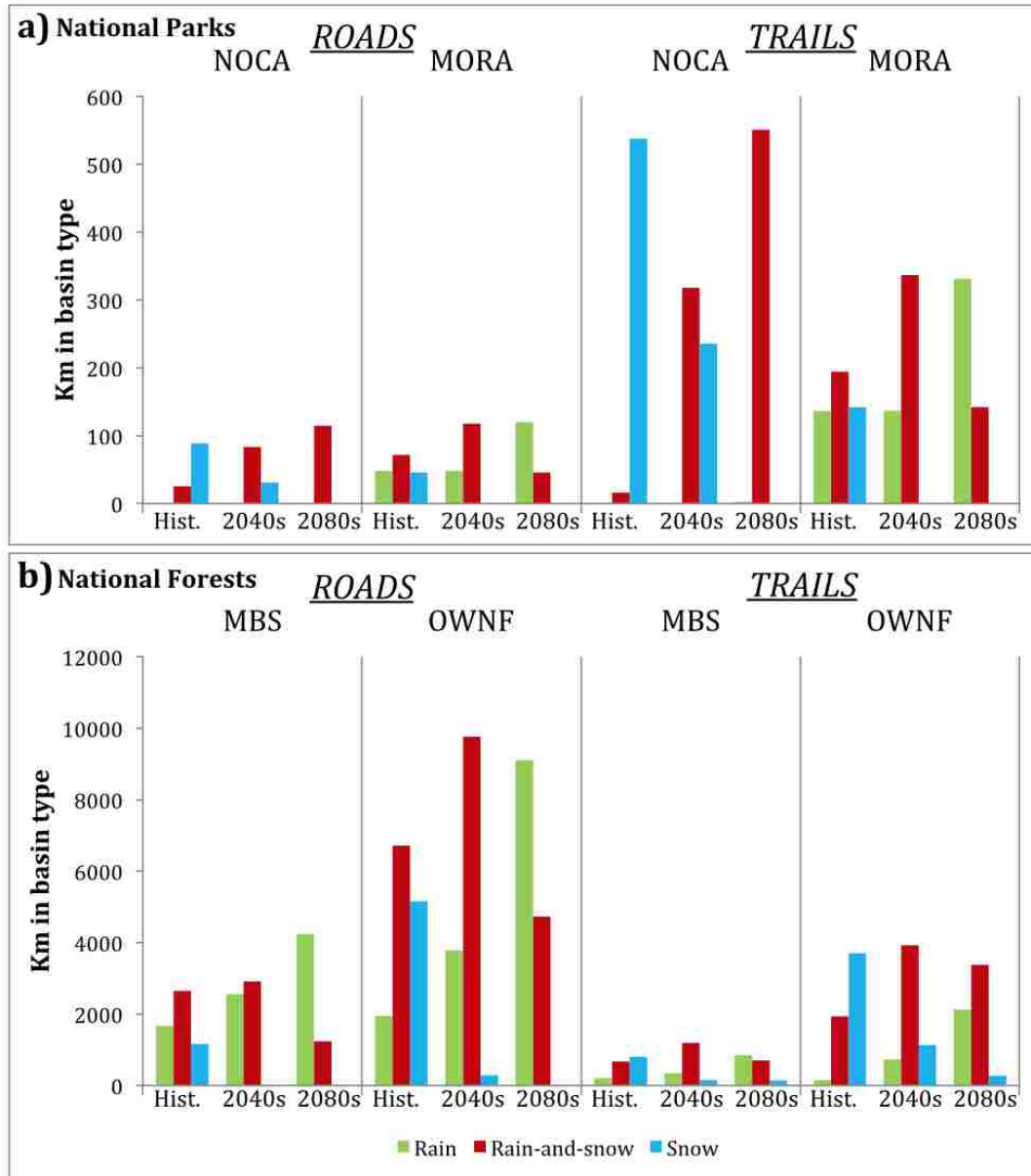


Fig. 2.4 Kilometers of roads and trails in each hydrologic basin type within the two national parks (a) and two national forests (b) across the NCAP landscape during three time periods: historic, 2040s, and 2080s

Lettenmaier 2007) may expose early-season visitors to more intense hydrologic or weather extremes than they have historically encountered (Scott et al. 2007). Higher precipitation intensity could decrease driver safety (Hambly et al. 2013) and higher flood hazard in autumn could make river recreation more perilous. Amplified fire regimes driven by climate change (Rogers et al. 2011) emphasize the value of access for fire management, but could also reduce safe operation of some roads and require additional emergency response to protect recreationists and communities. Earlier access to roads and trails may also increase the need for extended seasonal maintenance and construction activities (Mills et al. 2009).

2.3.2 Adaptation

2.3.2.1 *Adapting to changing flood hazard and extreme flows*

Workshop participants identified adjustments to operations, designs, management, and planning that may increase resistance and resilience to changing high flows and flood hazards. One “no regrets” strategy is to continue to upgrade the aging system of roads and stream crossings as required by the Northwest Forest Plan and the 2005 Travel Management Rule (36 CFR part 212). These upgrades are intended to increase the resistance of roads at stream crossings to higher peak flows and flood frequency, and can enable adaptation if climate change is considered in design (Halofsky et al. 2011; Littell et al. 2012). Currently some culverts on fish-bearing streams are being replaced with culverts designed for aquatic organism passage, following the U.S. Forest Service Stream Simulation design standards and requirements of the Endangered Species Act. This design often results in higher culvert flow and debris capacity and provides a resistance strategy for higher peak flows. Given projected changes in basin types and Q100, engineers may consider upgrades of culverts and bridges in areas with projected greater hydrologic change (e.g., in mixed-rain-and-snow basins) (Meyer 2008; Halofsky et al. 2011). They could also use projections of future Q100 as future flood hazard (Fig. 3) to design replacements or to identify areas for enhancing culvert and bridge capacity projects (Halofsky et al. 2011; Tohver et al. 2014).

Another “no regrets” tactic is to expand current efforts to inventory roads, culverts, and stream crossings as part of a sustainable roads analysis. These inventories provide critical information for identifying future repairs, replacements, and upgrades, increasing the capacity of the transportation system to adapt to changing hydrologic regimes. Areas where damage is most likely to escalate can be identified by combining information on where roads currently experience frequent flood damage with spatial data on infrastructure condition and projected changes in flood hazard.

Funding limitations were identified as a key barrier to climate adaptation because they often hinder efforts to upgrade the transportation system (Eisenack and Stecker 2012). Extreme floods that damage roads and culverts were identified as opportunities to replace existing structures with ones that are more resistant to higher peak flows. However, these replacements, called “betterments,” can be difficult to fund under eligibility requirements for the Emergency Relief for Federally Owned Roads (ERFO) program because the default policy proscribes “in-kind” replacement with the same infrastructure that was in place at the time of damaged. Sufficient justification for betterments based on climate change impacts could provide new avenues to increase resistance and resilience of repaired and replaced infrastructure (Tohver et al. 2014).

Response strategies to address projected changes in high flows include: rerouting roads and trails farther from streams and rivers, relocating transportation routes to locations that do not require culverts or bridges, and decommissioning highly vulnerable roads or trails. The USFS has a large inventory of logging roads no longer used in forest management. In some cases, the current road system may provide multiple routes to specific destinations, and climate vulnerability

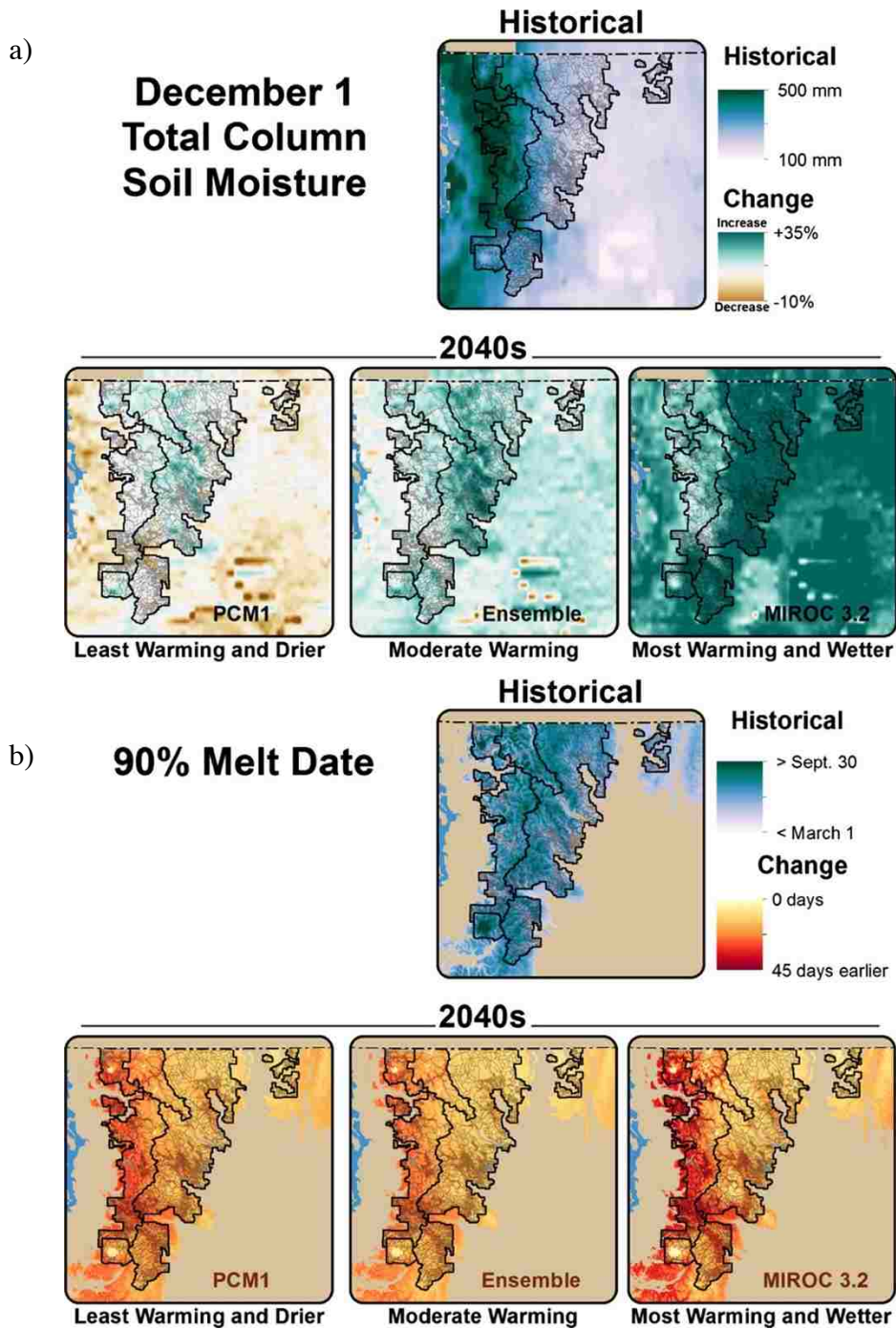


Fig. 2.5 Percentage change in total soil moisture content on December 1 within the NCAP landscape for 2040s (2030–2059), compared with historical levels (1916–2006), calculated as $[(\text{future} - \text{historical}) / \text{historical}] * 100$ (a). Average change in date at which 90 % of SWE is melted from historical date (upper panel) and the 2040s date compared to historical dates (bottom panels) (b). Future projections modeled using A1B emission scenario and three model configurations, an ensemble of 10 GCMs and two individual GCMs projecting less warming and drier conditions (PCM1) and more warming and wetter conditions (MIROC 3.2) than ensemble mean. Gray lines show roads and trails.

assessments can be used to identify which roads to maintain and which roads to close (Meyer 2008). However, the lack of redundancy in roads and trails in national parks will likely focus adaptation efforts on increasing resilience or resistance of the existing infrastructure, such as change in use or modes of transportation from car to bike or foot. Changes to the road and trail system are often opposed by a public accustomed to access for recreation. Working with local communities and recreational user groups, land managers can convert roads from vehicle to non-vehicular use, which can reduce maintenance costs and risks to aquatic habitat. Greater public involvement can generate political support and possibly funding from external sources to maintain access (Irvin and Stansbury 2004). Incorporating decision “triggers” as an adaptation measure in long-term plans (e.g., closure of a road if it is damaged by flooding) can enhance the capacity to respond to climate change impacts with well-defined actions already vetted through public review (Eisenack and Stecker 2012).

2.3.2.2 Adapting to increasing soil moisture and landslide hazard

Road and trail management may need to be modified to reduce adverse impacts and maintenance costs associated with higher soil moisture. Increased soil saturation could create more boggy areas around roads and trails and associated erosion and damage to infrastructure. Recreation managers may consider locations with projected increases in winter soil moisture in their maintenance prioritization process (Fig. 2.5a). Short-term “no regrets” adaptation tactics for trails include improving drainage, stabilizing slopes, and restoring vegetation cover. More repairs and reroutes may be necessary to avoid damage to vegetation when users stray from established trails to avoid saturated soils and inundated sections. Short-term adaptation tactics for roads include reducing weight on the road, altering road surface type, drainage improvements, and planning for higher maintenance costs. However, repeated landslides and slope failures may require that vulnerable roads and trails be closed and that new construction avoid areas with elevated hazard.

Climate change may necessitate greater emphasis on hydrologic impacts in road and trail design. Roads and trails constructed perpendicular to the slope can intercept, block, restrict, and channel water, which can exacerbate landslide hazards projected due to increasing soil moisture. Road and trail resilience can be increased by constructing improved drainage and enhanced erosion control. Monitoring erosion and saturated soils near roads and trails will be important for identify deterioration and prioritize locations for restoration and repair. Monitoring may be more effective if it focuses on infrastructure in areas with the highest projected increases in soil moisture (Fig. 2.5) and in mixed-rain-and-snow basins (Fig. 2.2), where the largest shifts in precipitation type are expected.

2.3.2.3 Adapting to changes in snowpack and visitor use patterns

Reduced snowpack and earlier snowmelt could allow earlier access for visitors to higher elevations and a longer “summer” recreation season (Michalak et al. 2013). However, an expanded visitor season would increase the cost of operating facilities (e.g., visitor centers and campgrounds) and require modifications to recreation management (Albano et al. 2013). Due to budget constraints, NPS and USFS managers are challenged to maintain visitor facilities and access. Therefore, longer snow-free seasons may not necessarily result in longer visitor access because agencies may lack capacity to open transportation routes earlier in the spring. Additionally, risks to public safety could increase with more frequent disruptions to access from

flooding and landslides. A long-term adaptation strategy would be to increase funding to allow for greater maintenance and an expanded visitor season. Public safety may be improved through regulation of seasonal use, combined with better information about current conditions and weather forecasts, especially in early spring and late autumn, before and after maintenance activities. Partnerships with recreational user groups may generate opportunities to communicate this message to the public, thus enhancing awareness of safety issues. Monitor changes in the timing, location, and number of visitors can provide data on where management policies could be modified.

2.4 Summary and Discussion

Historical development of roads and trails and regional climate exert strong controls on current patterns of access in the north-central Cascade Range of Washington, U.S.A. Climate change is expected to result in important changes in access via impacts to flooding, landslide hazard, and seasonal snowcover. The NCAP science- management collaboration evaluated the vulnerability of access to climate change and identified adaptation options applicable throughout the contiguous lands of two national forests and two national parks where altered weather patterns are already affecting the transportation network (Maurer et al. 2011; MacArthur et al. 2012). Hydrologic models project continued and escalating exposure to climate-induced changes in access due to shifting hydrologic regimes (Tohver et al. 2014; Salathé et al. 2014).

In the short term, natural climatic variability may exacerbate, compensate for, or even temporarily reverse expected trends in some hydroclimatic processes. However, in the long term (40–100 years; Meyer 2008), the cumulative impacts of climate change are expected to become the dominant factor, particularly for temperature-related effects (Mote et al. 2008). In response to these challenges, the NCAP identified adaptation strategies and tactics to enhance the resistance, resilience, and response of the transportation system. The federal lands context of this assessment provides opportunities to implement adaptation over a large geographic area, such as design standards, operations, and planning with consideration of a dynamic climate. Incorporating adaptation into long-term planning is an important element of climate change planning (NRC 2008; Whitely Binder et al. 2010; Hamlet 2010) and an adaptive management system can allow decisions regarding repairs, restoration, and closures to evolve as hydrologic regimes evolve. The vulnerability assessment and adaptation planning described here focuses on transportation systems on federal lands, providing an approach that can be applied to other resource sectors and mountainous regions. The results are particularly relevant to areas where snowpack is a key hydrologic component and infrastructure is in close proximity with streams.

Acknowledgments

We thank USFS and NPS staff for organizing and participating in the workshop and providing subsequent expertise, input, and vision, especially Dave L. Peterson. Climate and hydrologic data produced by Climate Impacts Group (CIG): Guillaume Mauger, Ingrid Tohver, Jeremy Littell, and Se-Yeun Lee. Figures (except Fig. 2.4) by Robert Norheim and transportation data provided by Christopher DeLorto, National Park Service Transportation Scholar associated with the National Park Foundation and Eno Transportation Foundation. We are also grateful for the comments from three anonymous reviewers. Funding provided by the U.S. Department of the Interior, Northwest Climate Science Center; the National Park Service, North Cascades National Park Service Complex; the U.S. Forest Service, Pacific Northwest Research Station; and National Science Foundation, CBET Environmental Sustainability Program (Grant #1336725).

References

- Albano CM, Angelo CL, Strauch RL, Thurman LL (2013) Potential effects of warming climate on visitor use in three Alaskan national parks. *Park Sci* 30(1):36–44
- Chapman L (2007) Transport and climate change: a review. *J Transp Geogr* 15:354–367
- Crozier MJ (1986) Landslides: causes, consequences, and environment. Croom Helm, Ltd. Dover, NH
- Dominguez F, Rivera E, Lettenmaier DP, Castro CL (2012) Changes in winter precipitation extremes for the western United States under a warmer climate as simulated by regional climate models. *Geophys Res Lett* 39:1–7
- Eisenack K, Stecker R (2012) A framework for analyzing climate change adaptation as actions. *Mitig Adapt Strateg Glob Chang* 17(3):243–260
- Elsner MM, Cuo L, Voisin N et al (2010) Implications of 21st century climate change for the hydrology of Washington state. *Clim Chang* 102:225–260
- Halofsky JE, Peterson DL, O'Halloran KA, Hoffman CH (2011) Adapting to climate change at Olympic National Forest and Olympic National Park. Gen Tech Rep PNW-GTR-844. Portland, OR: U.S. Department of Agriculture, Forest Service, Pacific Northwest Research Station
- Hambly D, Andrey J, Mills B, Fletcher C (2013) Projected implications of climate change for road safety in Greater Vancouver, Canada. *Clim Chang* 116:3–4
- Hamlet AF, Elsner MM, Mauger GS, Lee S, Tohver I, Norheim RA (2013) An overview of the Columbia basin climate change scenarios project: approach, methods, and summary of key results. *Atmosphere Ocean* 51(4): 392–415
- Hamlet AF (2010) Assessing water resources adaptive capacity to climate change impacts in the Pacific Northwest region of North America. *Hydrol Earth Syst Sci* 7(4):4437–4471
- Hamlet AF, Lettenmaier DP (2007) Effects of 20th century warming and climate variability on flood risk in the western US. *Water Resour Res* 43: W06427
- Hamlet AF, Mote PW, Clark MP, Lettenmaier DP (2005) Effects of temperature and precipitation variability on snowpack trends in the Western United States. *J Clim* 18:4545–4561
- Huggel C (2009) Recent extreme slope failures in glacier environments: effects of thermal perturbations. *Quat Sci Rev* 28:1119–1130
- Intergovernmental Panel on Climate Change (IPCC) (2007) Climate sensitivity and feedbacks. In: Pachauri RK, Reisinger A (eds) *Climate change 2007: synthesis report. Contribution of Working Groups I, II and III to the Fourth Assessment Report of the Intergovernmental Panel on Climate Change*. Geneva, Switzerland: Intergovernmental Panel on Climate Change
- Kloprogge P, Van der Sluijs J (2006) The inclusion of stakeholder knowledge and perspective in integrated assessment of climate change. *Clim Chang* 75:359–389
- Irvin RA, Stansbury J (2004) Citizen participation in decision making: Is it worth the effort? *Public Adm Rev* 64(1): 55–65
- Liang X, Lettenmaier DP, Wood EF, Burges SJ (1994) A simple hydrologically based model of land surface water and energy fluxes for GSMs. *J Geophys Res* 99:14415–14428
- Louter D (2006) *Windshield wilderness: cars, roads, and nature in Washington's national parks*. University of Washington Press, Seattle
- Littell JS, Peterson DL, Millar CI, O'Halloran KA (2012) U.S. national forests adapt to climate change through science-management partnerships. *Clim Chang* 110:269–296
- Littell JS, Elsner MM, Mauger GS, et al (2011) Regional climate and hydrologic change in the Northern US Rockies and Pacific Northwest: internally consistent projections of future climate for resource management. Project report available at: http://cses.washington.edu/picea/USFS/pub/Littell_etal_2010/Littell_etal_2011_Regional_Climatic_And_Hydrologic_Change_USFS_USFWS_JVA_17Apr11.pdf. Accessed 31 Jan. 2014
- MacArthur J, Mote P, Ideker J et al. (2012) Climate change impact assessment for surface transportation

- in the Pacific Northwest and Alaska. Research Report WA-RD 772. Olympia, WA: State of Washington, Department of Transportation, Office of Research and Library Services. OTREC-RR-12-01. Salem, OR: Oregon Transportation Research and Education Consortium
- Mantua N, Tohver I, Hamlet AF (2010) Climate change impacts on streamflow extremes and summertime stream temperature and their possible consequences for freshwater salmon habitat in Washington State. *Clim Chang* 201:187–223
- Martin YE (2006) Wildfire disturbance and shallow landsliding in coastal British Columbia over millennial time scales: a numerical modeling study. *Catena* 69
- Mauger G (2011) Meteorological dataset. Climate Impacts Group, University of Washington. Unpublished data. Available at: http://cses.washington.edu/picea/mauger/VIC_SNOW/pub/. Accessed 31 Jan. 2014
- Maurer M, Roalkvam, CL, and Salsbury, SL (2011) Climate Impacts Vulnerability Assessment. Washington State Department of Transportation Report, Olympia, 70 pp
- Meyer MD (2008) Design Standards for US Transportation Infrastructure: The Implications of Climate Change. Transportation Research Board, National Research Council, Washington, D.C. 30 pp
- Michalak J, Withey JC, Lawler JL (2013) Climate adaptation planning for British Columbia provincial parks: A guide to conducting a rapid assessment of climate impacts on park management objectives. Prepared for North Pacific Landscape Conservation Cooperative. University of Washington, Seattle
- Millar CI, Stephenson NL, Stephens SL (2007) Climate change and forests of the future: managing in the face of uncertainty. *Ecol Appl* 17:2145–2151
- Mills BN, Tighe SL, Andrey J, Smith JT, Huen K (2009) Climate change implications for flexible pavement design and performance in southern Canada. *J Transp Eng* 135(10):773–782
- Mote PW, Salathé EP (2010) Future climate in the Pacific Northwest. *Clim Chang* 102:29–50
- Mote P, Hamlet AF, Salathé EP (2008) Has spring snowpack declined in the Washington Cascades? *Hydrol Earth Syst Sci* 12:193–206
- Nakićenović N, Swart R (eds) (2000) Special report on emissions scenarios: a special report of working group III of the Intergovernmental Panel on Climate Change. Cambridge University Press, Cambridge, United Kingdom, and New York
- Nearly DG, Ryan KC, DeBano LF (eds) (2005) Wildland fire in ecosystems: effects of fire on soils and water. Gen. Tech. Rep. RMRS-GTR-42-vol.4., Rev. 2008, U.S. Department of Agriculture, Forest Service, Rocky Mountain Research Station, Ogden, UT
- National Research Council (NRC) (2008) Potential impacts of climate change on U.S. transportation: Special report 290. Transportation Research Board, National Research Council, The National Academies Press, 280 pp
- Pelto MS, Riedel J (2001) Spatial and temporal variations in annual balance of North Cascade glaciers, Washington 1984–2000. *Hydrol Process* 15:3461–3472
- Peterson DL, Millar CI, Joyce LA, et al (2011) Responding to climate change in national forests: a guidebook for developing adaptation options. Gen. Tech. Rep. PNW-GTR-855. Portland, OR: U.S. Department of Agriculture, Forest Service, Pacific Northwest Research Station
- Raymond CL, Peterson DL, Rochefort RM (2014) Climate Change Vulnerability and Adaptation in the North Cascades Region, Washington. Gen Tech Rep PNW-GTR-892. Portland, OR: U.S. Department of Agriculture, Forest Service, Pacific Northwest Research Station
- Raymond CL, Peterson DL, Rochefort RM (2013) The north Cascadia adaptation partnership: a science management collaboration for responding to climate change. *Sustainability* 5(1):136–159
- Rogers BM, Neilson RP, Drapek R, Lenihan JM, Wells JR, Bachelet D, Law BE (2011) Impacts of climate change on fire regimes and carbon stocks of the U.S. Pacific Northwest. *J Geophys Res* 116:G03037

- Salathé EP, Hamlet AF, Mass CF, Lee S-Y, Stumbaugh M, Steed R (2014) Estimates of 21st Century flood risks in the Pacific Northwest based on regional climate model simulations. *J Hydrometeorol*. doi:10.1175/JHM-D-13-0137.1
- Schmidt K, Roering JJ, Stock JD et al (2001) The variability of root cohesion as an influence on shallow landslide susceptibility in the Oregon Coast Range. *Can Geotech J* 38:995–1024
- Schwartz HG, Meyer M, Burbank CJ, Kuby M, Oster C, Posey J, Russo EJ, and Rypinski A (2014) Ch. 5: Transportation. In: Melillo JM, Richmond TC, and Yohe GW (eds) *Climate Change Impacts in the United States: The Third National Climate Assessment*. U.S. Global Change Research Program, 130–149
- Scott D, Jones B, Konopek J (2007) Implications of climate and environmental change for nature-based tourism in the Canadian rocky mountains: a case study of Waterton lakes national park. *Tour Manage* 28:570–570
- Snover AK, Mauger GS, Whitely Binder LC, Krosby M, Tohver I (2013) *Climate Change Impacts and Adaptation in Washington State: Technical Summaries for Decision Makers*. State of Knowledge Report prepared for the Washington State Department of Ecology. Climate Impacts Group, University of Washington, Seattle
- Snover AK, Whitely Binder L, Lopez J, Willmott E, Kay J, Howell D, and Simmonds J (2007) *Preparing for Climate Change: A Guidebook for Local, Regional, and State Governments*. In association with and published by ICLEI – Local Governments for Sustainability, Oakland, CA
- Strauch RL, Raymond CL, Hamlet AF (2014) Climate change, hydrology, and access in the North Cascade Range. In: Raymond CL, Peterson DL, and Rochefort RM (eds) *Climate change vulnerability and adaptation in the North Cascade Region, Washington*. Gen Tech Rep PNW-GTR-892. Portland, OR: U.S. Department of Agriculture, Forest Service, Pacific Northwest Research Station
- Suffling R, Scott D (2002) Assessment of climate change effects on Canada's national park system. *Environ Monit Assess* 74(2):117–139
- Tohver, I, Hamlet AF, Lee S (2014) Impacts of 21st century climate change on hydrologic extremes in the Pacific Northwest region of North America. *J Amer Water Resour Assoc* 1–16, doi:10.1111/jawr.12199
- U.S. Department of Agriculture, Forest Service (USDA FS) (2010) *National roadmap for responding to climate change*. Washington, DC, USA
- U.S. Department of the Interior, National Park Service (USDI NPS) (2010) *Climate change response strategy*. Climate Change Response Program. Washington, DC, USA, Available at: http://www.nps.gov/orgs/ccrp/upload/NPS_CCRS.pdf. Accessed 31 Oct. 2013
- Wall T, Meyer M (2013) *Risk-Based Adaptation Frameworks for Climate Change Planning in the Transportation Sector*. Transportation Research Board of the National Academies, Washington, DC
- Whitely Binder LC, Krencicki Barcelos J, Booth DB et al (2010) Preparing for climate change in Washington State. *Clim Chang* 102(1–2):351–376

Supplemental material

https://static-content.springer.com/esm/art%3A10.1007%2Fs10584-015-1357-7/MediaObjects/10584_2015_1357_MOESM1_ESM.pdf

Chapter 3. A hydro-climatological approach to predicting regional landslide probability using Landlab

Ronda Strauch¹, Erkan Istanbuluoglu¹, Sai Siddhartha Nudurupati¹, Christina Bandaragoda¹, Nicole M. Gasparini², and Gregory E. Tucker³

¹Civil and Environmental Engineering, University of Washington, Seattle, WA

²Earth and Environmental Sciences, Tulane University, New Orleans, LA, USA

³Cooperative Institute for Research in Environmental Sciences (CIRES) and Department of Geological Sciences, University of Colorado Boulder, Boulder, CO, USA

Note: This manuscript is under review as a discussion paper in Earth Surface Dynamics, which is an open access journal and permission to reproduce is included under a Creative Commons 4.0 by-nc-nd license.

Abstract

We develop a hydro-climatological approach to modeling of regional shallow landslide initiation that integrates spatial and temporal dimensions of parameter uncertainty to estimate an annual probability of landslide initiation. The physically-based model couples the infinite slope stability model with a steady-state subsurface flow representation and operates on a digital elevation model. Spatially distributed raster data for soil properties and a soil evolution model and vegetation classification from National Land Cover Data are used to derive parameters for probability distributions to represent input uncertainty. Hydrologic forcing to the model is through annual maximum recharge to subsurface flow obtained from a macroscale hydrologic model, routed on raster grid to develop subsurface flow. A Monte Carlo approach is used to generate model parameters at each grid cell and calculate probability of shallow landsliding. We demonstrate the model in a steep mountainous region in northern Washington, U.S.A., using 30-m grid resolution over 2,700 km². The influence of soil depth on the probability of landslide initiation is investigated through comparisons among model output produced using three different soil depth scenarios reflecting uncertainty of soil depth and its potential long-term variability. We found elevation dependent patterns in probability of landslide initiation that showed the stabilizing effects of forests in low elevations, an increased landslide probability with forest decline at mid elevations (1,400 to 2,400 m), and soil limitation and steep topographic controls at high alpine elevations and post-glacial landscapes. These dominant controls manifest in a bimodal distribution of spatial annual landslide probability. Model testing with limited observations revealed similar model confidence for the three hazard maps, suggesting suitable use as relative hazard products. Validation of the model with observed landslides is hindered by the completeness and accuracy of the inventory, estimation of source areas, and unmapped landslides. The model is available as a component in Landlab, an open-source, Python-based landscape earth systems modeling environment, and is designed to be easily reproduced utilizing HydroShare cyberinfrastructure.

3.1 Introduction

In steep mountainous landscapes, episodic shallow landslides (generally <2 m depth; Bordoni et al, 2015) and landslide-triggered debris flows are often the dominant form of hillside erosion and

major source of sediment into streams (Benda and Dunne, 1997a, b; Goode et al., 2012). Where landslide processes intersect with human development, they cause property damage, disruption of infrastructure, injury, and loss of life (Taylor and Brabb, 1986; Baum et al., 2008a), contribute to sedimentation in reservoirs (Bathurst et al., 2005), and may even lead to dam failures (Ghirotti, 2012). Landslides provide punctuated sediment input to streams, affecting stream geomorphology (Benda and Dunne, 1997a, 1997b) and ecosystem dynamics (Pollock, 1998; May et al., 2009). Landslide hazard maps are common tools used to characterize the relative potential for landslide occurrence in space, either qualitatively (using susceptibility levels) or quantitatively (using modeled landslide probabilities) (van Westen et al., 2006; Raia et al., 2014).

Our objective is to develop a parsimonious probabilistic model of shallow landslide initiation that can be implemented with minimal calibration for landslide hazard mapping using regionally available, spatially distributed input data for soil, vegetation type, local topography, and hydroclimatology. Based on the literature review presented below, we propose that a regional landslide hazard model should: (1) be flexible enough to incorporate changes in intrinsic and extrinsic conditions, such as vegetation and climate; (2) account for spatial variability in model parameters and forcings, and (3) integrate spatial and temporal dimensions of uncertainty to quantify landslide probability. With these principles in mind, we develop a hydro-climatological approach to modeling regional landslide hazard using the Landlab (version 1.1.0) modeling toolkit - an open-source, Python-based earth surface modeling framework that provides flexible model customization and coupling (Hobley et al., 2017). Next, we provide a short literature review that guides the design of our landslide modeling approach.

3.1.1 Geomorphology and Modeling Background

Landslides occur when destabilizing forces due to gravity and pore-water pressure exceed the resisting forces of friction and cohesion over a failure plane. These forces are controlled by intrinsic hillslope conditions, including attributes of topography, such as local slope and upslope contributing area, and properties of rock, soil, and vegetation root cohesion; and extrinsic drivers of rainfall, snowmelt, and earthquakes (Crozier, 1986; Wu and Sidle, 1995; van Beek, 2002; Naudet et al., 2008). There are three primary components of a landslide: (1) a source area or landslide scar where the initial failure begins, (2) a transmission or scour zone, such as a debris flow channel, and (3) a toe or zone of deposition (Lu and Godt, 2013).

Landslide susceptibility can be identified through numerous methods, which can be broadly grouped into empirical methods and process-based numerical models (Hammond et al., 1992; Wu and Sidle, 1995; Sidle and Ochiai, 2006). Data-driven empirical approaches relate the number and frequency of historical landslide observations in a region to triggering events (Caine, 1980; Crozier, 1999; Glade, 2001), landscape attributes (Carrara et al., 1995; Chung et al., 1995; Lee et al., 2007), or a combination of both (Kirschbaum et al., 2012) using threshold relations and various statistical models such as logistic regression, fuzzy logic, artificial neural networks, and support vector machine (Lee et al., 2007; Pardeshi et al., 2013; Chen et al., 2014). Empirical methods have been used for landslide susceptibility zonation or categorizing the landscape into relative landslide hazards (Sidle and Ochiai 2006).

Process-based models employ effective stress principles to characterize the destabilizing and resisting forces under hydrologic drivers (Iverson, 2000; Montrasio and Valentino 2016),

offering the ability to explore changes in environmental and climatic conditions. Such process-based models are especially useful in areas with limited landslide inventories (Pardeshi et al. 2013). Recent process-based numerical models have largely focused on improving the characterization of the space-time dynamics of subsurface flow as a driver of pore-water pressure (e.g., Baum et al., 2008b; Raia et al., 2014; Anagnostopoulos et al., 2015; Montrasio and Valentino, 2016). Distributed hydrology models that use steady-state or transient solutions for subsurface flow depth were coupled with an infinite-slope stability model that solves the ratio of stabilizing to destabilizing forces on a failure plane parallel to the land surface (Montgomery and Dietrich, 1994; Miller, 1995; Wu and Sidle, 1995; Pack et al., 1998; Borga et al., 1998; Casadei et al., 2003; Tarolli and Tarboton, 2006; Baum et al., 2008b).

Steady-state models assume that lateral subsurface flow, driven by the topographic gradient, at each point on the landscape is in equilibrium with a steady-state recharge rate (Montgomery and Dietrich, 1994; Pack et al., 1998). The degree of soil saturation is predicted proportional to the ratio of upslope contributing area to local slope, and a ratio of watershed recharge and local soil transmissivity, following TOPMODEL assumptions (Beven and Kirkby, 1979; O'Loughlin, 1986; Pack et al., 1998). More recent efforts have focused on the development of transient flow models in various complexities by coupling vertical infiltration and redistribution processes in the unsaturated zone, using the Richards equation for unsaturated flow (Richards, 1931) or its variants, with lateral flow parameterizations such as kinematic wave in 1- and 2-dimensions (Iverson, 2000; Casadei et al., 2003; Baum et al., 2008b; Godt and McKenna, 2008; Raia et al., 2014; Alvioli et al., 2014; Anagnostopoulos et al., 2015).

While transient flow models have contributed to improved understanding of the influence of weather forcing and temporal variability in precipitation on landslide initiation, they remain tools typically applied for relatively small-scale assessments (Iverson, 2000; Raia et al. 2014). Transient models require a large number of hydrologic soil and vegetation parameters that are highly variable, uncertain, and difficult to measure or estimate (Godt and McKenna 2008; Baum et al. 2008b). In addition, in most steep forested mountains where landslide risk is high, presence of macropores due to connected root structures, biological activity, fractures, large clasts, and lenses, leads to preferential and funneled flows that violate the assumptions of most matrix-flow models (Nimmo, 2005; Sidle et al., 2001; Gabet et al., 2003; Beven and Germann 2013). Numerical solutions to flow equations also present a major computational bottleneck in large-scale applications for probabilistic quantification of landslide hazard.

Comparison of steady-state and transient models using case studies with known extreme rainfall events that caused widespread landsliding involve statistical model performance evaluation (Zizioli et al., 2013). While using transient hydrologic models provided slight improvements in the prediction of landslide locations, overall, statistical comparisons of model outputs between steady-state and transient models revealed fairly similar degrees of success (Gorsevski et al., 2006; Zizioli et al., 2013; Anagnostopoulos et al., 2015; Boroni et al., 2015; Formetta et al., 2016). In some applications, model complexity increased the accuracy of predicted landslide locations at the expense of overestimating instability on unsaturated hillslopes (e.g., Godt et al., 2008; Bellugi 2011). In other cases, model precision increased while accuracy decreased (Gorsevski et al., 2006).

Data uncertainty due to spatial and temporal variability of parameters continues to be one of the major challenges in predicting landslides over broad regions (Crozier, 1986; Sidle and Ochiai, 2006; van Westen et al., 2006; Baum et al., 2014; Anagnostopoulos et al., 2015). These uncertainties and variabilities can develop from geological anomalies, inherent spatial heterogeneities in soil and vegetation properties and their changes over time, and sampling limitations (El-Ramly et al., 2002; Cho, 2007; Baum et al., 2014). Uncertainties in hydro-climate quantities, such as precipitation and recharge, are particularly pronounced in steep high mountain regions due to lack of observations and complex spatial and temporal atmospheric processes (Roe, 2005; Wayland et al., 2016). Designating landslide hazard as a probability, rather than an index, systematically accounts for uncertainty and variability in stability analysis (Hammond et al., 1992) and more appropriately represents complex systems (Berti et al., 2012). Currently, only limited process-based models account for data uncertainty in landslide hazard mapping (e.g., Pack et al., 1998; Raia et al., 2014).

Observations and model experiments suggest that the largest landslides are usually associated with the largest rainfall events (e.g., Page et al. 1994; Gorsevski et al., 2006). Considering that hillslope hydrology is more likely to attain equilibrium conditions during prolonged wet conditions (e.g., Barling et al., 1994; Borga et al., 2002), a steady-state representation of subsurface flow hydrology, coupled with a process-based infinite slope stability model is an efficient approach for predicting the likelihood of landslide hazard at regional scales.

Lastly, most landslide hazard methods disregard a temporal dimension over which landslide probability is defined (Wu and Sidle, 1995; van Westen et al., 2006). As a result of that, instead of using estimated probabilities directly in the form of return periods of observed landslides or expected values for risks resulting from landslides, models use probability estimates as relative indices (e.g., Pack et al., 1998) that can be used for hazard zonation (Pardeshi et al., 2013). Lack of temporal dimension limits the incorporation of model results into risks assessments and the decision-making processes in high-risk regions.

3.1.2 Approach Overview

We develop a process-based modeling approach for shallow landslide initiation that incorporates imprecisions and uncertainties in hydro-climatological forcing, soils, and land cover properties. Rather than predicting critical rainfall intensity necessary to destabilize hillslopes (Montgomery and Dietrich 1994) or a terrain stability index map (Pack et al. 2001, 2005), our approach aims to develop a spatially continuous probability of landslide *initiation* that can be updated as conditions and triggers evolve. The model evaluates the infinite slope stability equation at the scale of a grid cell from a Digital Elevation Model (DEM). Daily rate of recharge (i.e., flux of water entering saturated zone) can be provided by model users from a variety of grid resolutions from hydrologic models such as the Variable Infiltration Capacity (VIC) model (Liang et al. 1994) as used in our regional application, or assigned as parameters by the user. A “Source Tracking Algorithm” (STA) is developed to route spatially variable recharge fields, at the native resolution of a hydrology model, generically referred to as a Hydrology Source Domain (HSD), onto the grid resolution of slope stability calculations. Raster grids derived from soil texture and vegetation cover classes are used with look-up tables to estimate model parameters ranges obtained from the literature to quantify uncertainty. Through Monte Carlo simulation (Raia et al., 2014), we calculate the probability of landslide initiation at each landscape grid cell. Our

probability is further refined by a geomorphic soil evolution model that estimates soil depth with greater spatial heterogeneity than conventional soil survey map units, which is critical for slope stability analysis (Dietrich et al., 1995). This soil evolution model estimates long-term soil depth based primarily on soil mass production and slope-dependent sediment transport rules.

Landslide probability calculations are written in Python as a Landlab LandslideProbability component (landlab.github.io, including User Manual). The STA is available as a Landlab utility. The landslide model is designed as a user-written “driver” within Jupyter Notebooks, where the workflow of model application is presented. The driver and data are deployed on HydroShare (www.hydroshare.org), an online collaboration environment for sharing data, models, and code (Horsburgh et al., 2016; Idaszak et al., 2016), and made available for cloud computing via HydroShare JupyterHub infrastructure using a web browser (see Sect. 3.2.5).

In this work we explore the questions (1) How does regional hydro-climatology influence the spatial patterns of shallow landslide initiation over large geographic scales? and (2) How does distributed soil depth influence the probabilistic nature of landslide initiation compared to coarse-scale, homogenous soil depth estimates? We demonstrate our approach in a mountainous region of Washington, USA. This Pacific Northwest (PNW) region is naturally susceptible to landslides because of high and intense rainfall, steep mountains, active tectonics, and geologic and glacial history (Nadim et al., 2006; Sidle and Ochiai, 2006). The Oso landslide, which occurred in the vicinity of our study area in 2014, resulting in 43 fatalities and over \$50 million in economic losses, provides a solemn reminder of the hazard landslides present (Wartman et al., 2016). Although the Oso landslide was a deep-seated type, the greater frequency of shallow landslides affords utility and relevance to our model.

3.2 Methodology

3.2.1 Probabilistic approach to landslide initiation

Our approach is based on the infinite slope stability equation derived from the Mohr-Coulomb failure law that predicts the factor-of-safety (FS) stability index of a hillslope parcel from the ratio of stabilizing forces of soil cohesion and friction, reduced by pore-water pressure of subsurface flow, to destabilizing forces of gravity (Hammond et al., 1992; Wu and Sidle, 1995). The model as given by Pack et al. (1998) is:

$$FS = \frac{(C_r + C_s)/h_s \rho_s g}{\sin \theta} + \frac{\cos \theta \tan \phi (1 - R_w \rho_w / \rho_s)}{\sin \theta} \quad (1a)$$

$$C^* = (C_r + C_s)/h_s \rho_s g \quad (1b)$$

C^* is a dimensionless cohesion (Eq. 1b) embodying the relative contribution of cohesive forces to slope stability. When $C^* > 1$, cohesion is sufficient to hold the soil slab vertically (Pack et al., 1998). C_r and C_s are root and soil cohesion respectively [Pa], h_s is the soil depth perpendicular to slope [m], ρ_s and ρ_w are saturated soil bulk density and water density [kg/m^3], respectively, g is acceleration due to gravity [m/s^2], θ is slope angle of the ground, and ϕ is soil internal friction angle [$^\circ$]. Relative wetness, R_w , is defined as the ratio of subsurface flow depth, h_w , flowing parallel to the soil surface, to h_s . Deterministically, a hillslope element is unstable if $FS < 1$ and stable if $FS > 1$ (Sidle and Ochiai, 2006; Shelby, 1993). When $FS = 1$, the slope is “just-stable” or in a state of “limited equilibrium” (Lu and Godt, 2013).

Relative wetness is arguably the most dynamic factor at short time scales, relating to water table depth and to recharge rate. It is derived from local subsurface lateral flow, q_s [$m^2 d^{-1}$], represented by a 1-D (i.e., flow parallel to bedrock) form of the kinematic wave approximated by Darcy's law using topographic gradient of hillslope, $q_s = K_s h_w \sin \theta$ (Wu and Sidle, 1995). Under a steady-state assumption, lateral flow is in balance with the rate of water input, q_r [$m^2 d^{-1}$], through a uniform rate of recharge, R [$m d^{-1}$], across the upslope specific contributing area, a [m], $q_r = Ra$. This assumption gives: $Ra = K_s h_w \sin \theta$, where K_s is saturated hydraulic conductivity [$m d^{-1}$]. Solving this equation for h_w and dividing both sides by h_s gives R_w (Montgomery and Dietrich, 1994; Pack et al., 1998):

$$R_w = \frac{h_w}{h_s} = \min \left(\frac{R a}{T \sin \theta}, 1 \right) \quad (2)$$

Here T is soil transmissivity [$m^2 d^{-1}$], which is depth-integrated saturated hydraulic conductivity, K_s . For uniform K_s within the soil profile, $T = K_s h_s$. Ground saturates when $R_w = 1$, which represents hydrostatic conditions and the maximum value for R_w . Options for user-provided T or K_s are accepted by the component; although comparison of resulting probabilities were found to be similar given that the value of T was derived from h_s . We assume uniform conductivity within the soil profile overlying a relatively impermeable layer such as bedrock, and subsurface flow direction parallel to this drainage barrier (Montgomery and Dietrich, 1994). These assumptions are appropriate for relatively steep topography and to efficiently characterize wetness over large areas (Tarolli and Tarboton, 2006; van Westen et al., 2006).

A Monte Carlo simulation is used with equation (1) by assuming R , T , C ($C = C_r + C_s$), h_s and ϕ as random variables represented by probability distributions (Tobutt, 1982; Hammond et al., 1992). One benefit of Monte Carlo simulation is that many of the sources of inaccuracy (e.g., nonlinearity, input uncertainties) are overcome (Strenk, 2010; El-Ramly et al., 2002) by generating a distribution of samples over a plausible range for selected variables. The uncertainty in R is defined by using a time series of the maximum daily recharge in each year (e.g., Benda and Dunne, 1997a; Borga et al., 2002; Istanbuloglu et al., 2004). The model includes both spatially uniform and spatially distributed options for sampling recharge (described further in Sect. 3.2.3). Using sampled random variables in Eq. (1a), FS is calculated in each model iteration during the simulation. Annual probability of failure $P(F)$ and landslide return period (RP) at each grid cell are defined as (Hammond et al., 1992; Cullen and Frey, 1999):

$$P(F) = P(FS \leq 1) = n(FS \leq 1)/n \quad (3a)$$

$$RP = P(F)^{-1} \quad (3b)$$

Our model does not predict the size of a probable landslide at the initiation point, which can be smaller or larger than the size of a DEM grid. $P(F)$ gives a relative propensity that a landslide could initiate within the grid cell. The design of the model reflects the uncertainty of soil and vegetation within a grid cell. Therefore, if some random samples lead to a low deterministic FS, they contribute to an increase of the $P(F)$ within that cell.

3.2.2 Model Development in Landlab

The landslide modeling approach presented above is implemented in Landlab (landlab.github.io). Landlab is an open-source modeling toolkit written in Python for building and running two-dimensional numerical models of Earth-surface dynamics (Tucker et al., 2016; Hobbey et al.,

2017; Adams et al., 2017). A detailed explanation of the Landlab framework is provided in Hobley et al. (2017). Landlab provides a grid architecture, a suite of pre-built components for modeling surface or near-surface processes, and utilities that handle data creation, management, and interoperability among process components. The Landlab design allows for a “plug-and-play” style of model development, where process “components” can be coupled together in a user-customized “model driver”. Each component is a set of code functions that represent an individual process; the model driver has code used to import or generate required data, execute the component or set of components used in the model, and to visualize results. For example, once a DEM is imported as a Landlab grid instance, any Landlab component can be used with interoperable methods to attach data and perform operations. Landlab code developed for this work is explained in detail in the user manual of the Landlab LandslideProbability component available from eSurf and the Landlab github website.

The Landlab workflow developed in this regional landslide probability mapping study uses the LandslideProbability component presented in Fig. 3.1. The workflow includes preparing spatial model parameters and model forcing data completed in preprocessing steps outside of Landlab. A model driver is written to run the LandslideProbability component on RasterModelGrid (RMG) instance only. RMG is a Landlab class for creating raster grids and representing the connections among grid elements. A structured grid is generated that covers the model domain. Spatial model parameters and forcing variables supplied by the user are stored on the grid elements as Landlab data fields, which are NumPy arrays containing data associated with grid elements (in this case nodes). The driver imports Landlab and necessary Python libraries as well as loads and processes data required for the LandslideProbability component.

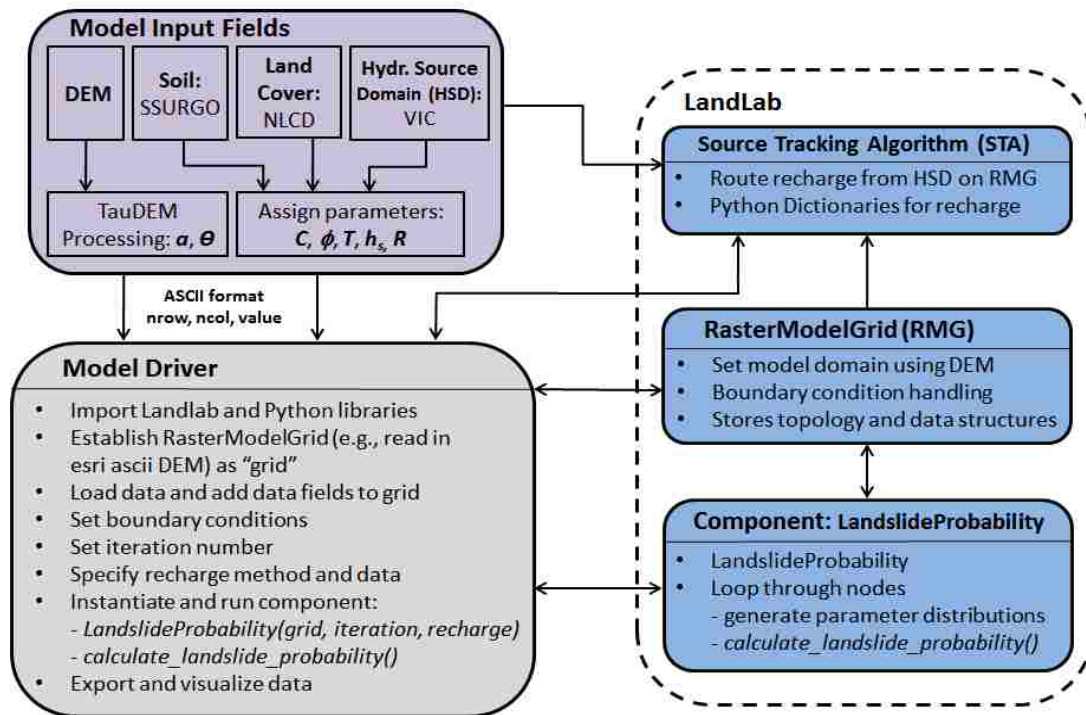


Figure 3.1. Workflow for landslide modeling using the Landlab LandslideProbability component. The user creates input parameter fields (purple box). The model driver (gray) imports Landlab, Python libraries, and model parameters fields: instantiates (e.g., create an instance) the RasterModelGrid and the component; and runs utilities and methods of Landlab (blue inside dashed box).

Slope angle and specific contributing area are static parameters derived from a DEM in pre-processing steps. Total cohesion, C (i.e., $C_r + C_s$), ϕ , h_s , and T are treated as random variables following a triangular distribution specified with three parameters (minimum, mode, and maximum) to represent spatial and temporal uncertainties in these parameters on the landscape (Cho, 2007; Dou et al., 2014). Triangular distributions give weight to the most likely value (i.e., mode) and have been proposed in other Monte Carlo simulations of slope stability (Hammond et al., 1992; El-Ramly et al., 2002; Strenk, 2010). Parameters of the triangular distribution can be assigned by relating categorical vegetation cover variables, for example from the National Land Cover Data (NLCD) (Jin, 2013; USGS, 2014b) or other map sources, with a lookup table for cohesion and using available soils data such as gridded Soil Survey Geographic Database (SSURGO) (DOA-NRCS 2016), to assign internal friction angle, soil depth, and transmissivity (see 3.3 for details). Soil density is set as a constant field, $2,000 \text{ kg m}^{-3}$ in our application.

In each Monte Carlo iteration, we characterize recharge as an annual maximum daily recharge event. Four options for sampling recharge are provided, which are identified in the model driver by selecting a probability *distribution*: *uniform*, *lognormal*, *lognormal_spatial*, and *data_driven_spatial*. The first two assign spatially uniform random variables with respective parameters of minimum and maximum, and mean and standard deviation. The latter two are designed to represent spatial variability in recharge based on historical annual maximum daily recharge routed to each node of the model domain. The *lognormal_spatial* option assigns mean and standard deviation of annual maximum recharge and uses lognormal distribution of recharge for simulation. The *data_driven_spatial* option uses a non-parametric Monte Carlo sampling approach to sample directly from historical recharge data. Upslope-averaged recharge for each grid node is calculated with the Landlab Source Tracking Algorithm (STA) utility using recharge from a HSD, which in this study is the VIC macroscale ($1/16^\circ$ or $5 \times 6 \text{ km}$ grid cell) hydrology model.

Within the model driver, the user also sets any boundary conditions, such as areas to exclude (i.e., bedrock outcrops, glaciers) and assigning the number of Monte Carlo iterations ($n \gg 1,000$, Hammond et al., 1992). The LandslideProbability component is instantiated by passing four arguments: the grid, number of iterations, recharge distribution, and recharge parameters. Multiple instances of the LandslideProbability class can be established in one driver to compare the results from different recharge specifications. Once the component has been instantiated, the component's method *calculate_landslide_probability()* is run. For each iteration, this method loops through each core node, generates unique model parameters, and calculates the relative wetness (Eq. 2) and deterministic FS index (Eq. 1a) at each iteration. At the end of the iterations, the $P(F)$ at the node is calculated as the number of iterations in which $FS \leq 1$ divided by the number of iterations. Variables output by the component at each core node include calculated probability of saturation and $P(F)$, which can be queried at each node or visualized across the entire grid within the driver or using a command line terminal to execute commands.

3.2.3 Hydrologic Data Processing

A key aspect of the regional landslide modeling approach is the linking of landslide hazard to hydro-climatological forcing at regional scales. The Landlab LandslideProbability component is

written with the capability to accept input from hydrologic model outputs. We used the VIC macroscale hydrologic model (Liang et al., 1994) to demonstrate this capability because it characterizes elevation-dependent differences in regional precipitation and temperature forcings and their influence on recharge through regulating snow accumulation and melt, rain-on-snow, evapotranspiration, and soil moisture. VIC is semi-distributed, predominantly physics-based macro-scale hydrology model, which is advantageous for representing distributed parameters of hydro-climatology that are not stationary in time over large regional areas (Hamlet et al., 2013).

The VIC model simulates the land surface as a large, flat, uniform grid with sub-grid heterogeneity (e.g., vegetation and elevation) based on statistical distributions. Daily or sub-daily meteorological drivers (e.g., temperature and precipitation) influence the fluxes of water and energy near the land surface. Each grid is simulated independently and flows between grid cells are ignored (e.g., unrouted). Precipitation enters the upper of typically three layers of soil and infiltrates to lower layers via a variable infiltration curve. Soil water can move between layers vertically and is lost through evapotranspiration and from the third layer as base/subsurface flow via non-linear recession. Water input in excess of infiltration forms surface runoff.

To characterize the annual probability when the ground is likely to be the most saturated, daily baseflow and surface runoff are summed at each VIC grid cell to represent recharge [mm d^{-1}] and the annual maximum daily value is selected for each model year, similar to others (e.g., Benda and Dunne, 1997a; Borga et al., 2002; Istanbuluoglu et al., 2004). The recharge data arrays are keyed to latitude, longitude, and grid cell ID (a user-defined ID for each VIC grid cell, in our case) packaged as Python dictionaries (*see Fig 1. of User Manual*). To help account for lateral fluxes in groundwater (van Beek, 2002), VIC recharge is routed to each node in the model grid using the STA utility, which also addresses the different spatial resolutions of VIC and the RMG. This Landlab utility was developed to derive the fraction of annual maximum recharge from each VIC grid cell within the upslope contributing area of each Landlab grid node. The fractions and VIC IDs are saved as values for two Python dictionaries keyed to the RMG node ID. At each node, these dictionaries are used to calculate the upstream proportionally-averaged maximum recharge for each year.

3.2.4 Soil Depth Evolution Model

Soil depth controls the temporal and spatial patterns of landsliding over geomorphic time scales and is considered one of the most significant parameters controlling the FS stability index, especially at depths less than 1.5 m (Benda and Dunne, 1997a; Istanbuluoglu et al., 2004; Catani et al., 2010; Sidle and Ochiai, 2006). Soil depth can vary in space and time as a function of weathering and sediment transport in relation to climate, lithology, topographic position, and vegetation cover (Dietrich et al., 1995). As an alternative to spatial soil maps such as the SSURGO database (*DOA-NRCS* 2016), which are often produced at the soil pedon-level, we developed a soil depth map using a simple soil evolution model and topographic and land cover attributes (Dietrich et al., 1995; Pelletier and Rasmussen, 2009; Tesfa et al., 2009; Bellugi et al., 2015).

Change in soil depth depends on soil production by bedrock weathering and slope-dependent sediment transport expressed as (Nicótina et al., 2011; Tucker and Slingerland, 1997; Heimsath et al., 1997):

$$\rho_s \frac{\partial h_s}{\partial t} = -\rho_r \frac{\partial z_b}{\partial t} - \rho_s \nabla q_s \quad (4)$$

where ρ_s and ρ_r are bulk densities for soil and rock, respectively, h_s is soil depth, z_b is the elevation of the soil-bedrock interface, t is time, ∇ is the topographic divergence operator for the topographic gradient, and q_s is the sediment flux. The soil production (e.g., first term in Eq. 4 on right side) is a function of the rate of change in the elevation of the soil-bedrock interface, which has been shown to decline exponentially with soil depth (Heimsath et al., 1997, Gabet et al., 2003):

$$\frac{\partial z_b}{\partial t} = -P_o e^{-\alpha h_s} \quad (5)$$

where P_o is the soil production rate from exposed bedrock (i.e., no soil cover) and α is the rate of exponential decay with depth. Diffusive sediment transport characterized in the second term on the right side of Eq. (4) can be represented by a simple soil creep function dominant in convex hillslopes as (Nicótina et al., 2011; Istanbuluoglu et al., 2004):

$$\nabla q_s = -K_d \nabla^2 z \quad (6)$$

where K_d is a linear hillslope diffusion coefficient and ∇^2 is Laplacian of elevation. Dividing Eq. (4) by ρ_r , multiplying by the ratio of ρ_r / ρ_s , and substituting Eq. (5) and Eq. (6) into Eq. (4), yields the following instantaneous soil depth equation:

$$\frac{\partial h_s}{\partial t} = \frac{\rho_r}{\rho_s} P_o e^{-\alpha h_s} + K_d \nabla^2 z \quad (7)$$

The change in soil depth with time based on Eq. (7) is added to the soil depth at $t-1$ (t in years) to evolve soil depth over time (see also: Pelletier and Rasmussen 2009).

Variable curvature profiles, steep and planar hillslopes, and abrupt knife edge drainage divides indicate nonlinear transport processes such as mass wasting (Roering et al., 2004, 1999). These landscape characteristics are common in the steep terrain; therefore, in every iteration of the model, Eq. (1a) and Eq. (2) are used to calculate FS within the soil evolution model. When $FS \leq 1$, soil is removed to bedrock by setting it to a very small value of 0.005 m to be consistent with the creep equation. In each model iteration, C and T, were randomly sampled and used deterministically in the FS Eq. (1a). Calibration of the soil evolution model is done by adjusting P_o and K_d for the location of the landslide analysis based on published long-term rates of erosion and diffusion. Creation, calibration, and application of the soil evolution model are detailed in Sect. 3.4.1.

3.2.5 Reproducibility

To publish a reproducible version of this research, we used the HydroShare (www.hydroshare.org) cyberinfrastructure platform, which is designed explicitly to encourage the reusing and sharing of models (Tarboton et al., 2014; Horsburgh et al., 2016; Morsy et al., 2017). Steps that supported reproducibility included using the HydroShare sharing settings with a workflow that started with *Private* while data and models were developed, *Discoverable* while research was being shared with colleagues for review, and *Public*, once our results were accepted

for publication. We used the *Select a license* function to add No Commercial (NC) use to our Creative Commons license. We made use of the *Groups* social collaboration, by making early versions of our research results available to invited participants of workshops and tutorial demonstrations to our Landlab group in HydroShare. The data and model are accessed by launching Jupyter Notebooks that access Landlab installed on JupyterHub servers at the National Center for Supercomputing Applications (Yin et al, 2017; Castranova, 2017). HydroShare features enable our current and future researchers to use the *Copy Resource* function to replicate our published resource (i.e., the landslide model) in their own account with *Derived from* metadata that references back to the published resource DOI, to serve as a starting point for their work.

3.3 Model application

3.3.1 Study Area

The model described above is applied within the geographical limits of the North Cascades National Park Complex (NOCA) in the state of Washington, U.S.A, managed by the U.S. National Park Service (Fig. 3.2). In recent decades, NOCA has experienced damaging and disruptive landslides that have impacted infrastructure and the public. Furthermore, the park area is covered by a recent soil survey between 2003 and 2009, including field investigation (DOA-NRCS and DOI-NPS, 2012), and has a complete map of mass wasting processes visually observed in the field (Riedel and Prohala, 2005).

NOCA is approximately 2,757 km², with 93% wilderness (in which no motorized or mechanized devices are permitted; DOI-NPS, 2012), which is ideal for studying naturally triggered landslides. The elevation ranges from about 100 m to 2,800 m (Fig. 3.2a). The terrain is composed of rock slopes at the highest elevations, short (<100 m) soil-mantled hillslopes, and landslides upslope of relatively straight debris flow channels connected to the fluvial system. Over 300 glaciers occupy mountain peaks in NOCA. The influence of the Pacific Ocean, approximately 80 km to the west, provides a humid temperate climate. However, the north-south oriented Cascade Mountains create an effective orographic climate boundary, separating a wetter west side from a drier east side. Reported mean annual precipitation ranges from about 708 mm in the low elevations of the eastern slopes to 4,575 mm at the highest mountain elevations west of the Cascade crest, with about 70% falling in November through March (Fig. 3.2b). This spatial precipitation gradient is the result of orographically-enhanced precipitation that leads to a strong rain shadow (Roe 2005). Average annual air temperatures range from -2 to 11°C, depending on elevation (DOA-NRCS and DOI-NPS, 2012).

Vegetation is mainly coniferous trees, with deciduous trees along river floodplains, and shrubs, meadows, and barren land in the subalpine and alpine environments. In this study vegetation classes were grouped into herbaceous, shrubland, and forest using the 2014 NLCD data, which is based on the land use/land cover (LULC) classification of 2011 Landsat satellite imagery (Jin, 2013; USGS, 2014b). Based on this classification, forest, shrubs, and herbaceous vegetation represent 58%, 17%, and 12% of the park, respectively. Elevation ranges for these vegetation classes are from 106 to 2363 m (forest), 110 to 2465 m (shrubs), and 121 to 2759 m (herbaceous).

The park geology is composed of a complex mosaic that includes mostly complexly faulted and folded sedimentary and volcanic rocks on the west side, unmetamorphosed sedimentary and

volcanic rock on the eastern edge, and highly squeezed and recrystallized metamorphic rock originating from great depth in middle (Haugerud and Tabor, 2009). Alpine and continental glaciation, along with rivers and mass-wasting processes, have created the landscape we observe today. The glaciers eroded U-shaped valleys with steep valley walls prone to landslides and flat valley floors with gravel-bed rivers. The lower ends of many valleys on the east side were not covered in alpine glaciers and have narrow, winding V-shaped canyons and steep, narrow rivers.

A park-wide landform mapping study identified six different types of mass wasting: rock fall/topple, debris avalanche, debris torrent, slump/creep, sackung, and snow avalanche-impacted landforms (Riedel et al., 2015). Mass wasting landforms were identified in the landform mapping using 1998 air photos at 1:12,000 scale, 7.5 minute topographic maps, bedrock geology maps, and field investigations. The minimum mapping unit was approximately 1,000 m², except for a few smaller slump units. In this study, we only used mapped debris avalanches for model confirmation as they often initiate by shallow landslide processes. Debris avalanches typically represent a mixture of failed rock and debris and the mapped polygon included head scar, transport and scour channels, and deposition zone represented in a single polygon (Fig 3.3a). We extract the highest 10% of the elevations in the mapped debris avalanche polygons as landslide source areas through comparison to aerial imagery (Tarolli and Tarboton, 2006). Landslide sources are more frequent in the intermediate elevations. In the NOCA region, 75% of landslide source areas are located in the 1,200 m to 2,000 m elevation range (Fig. 3.3b).

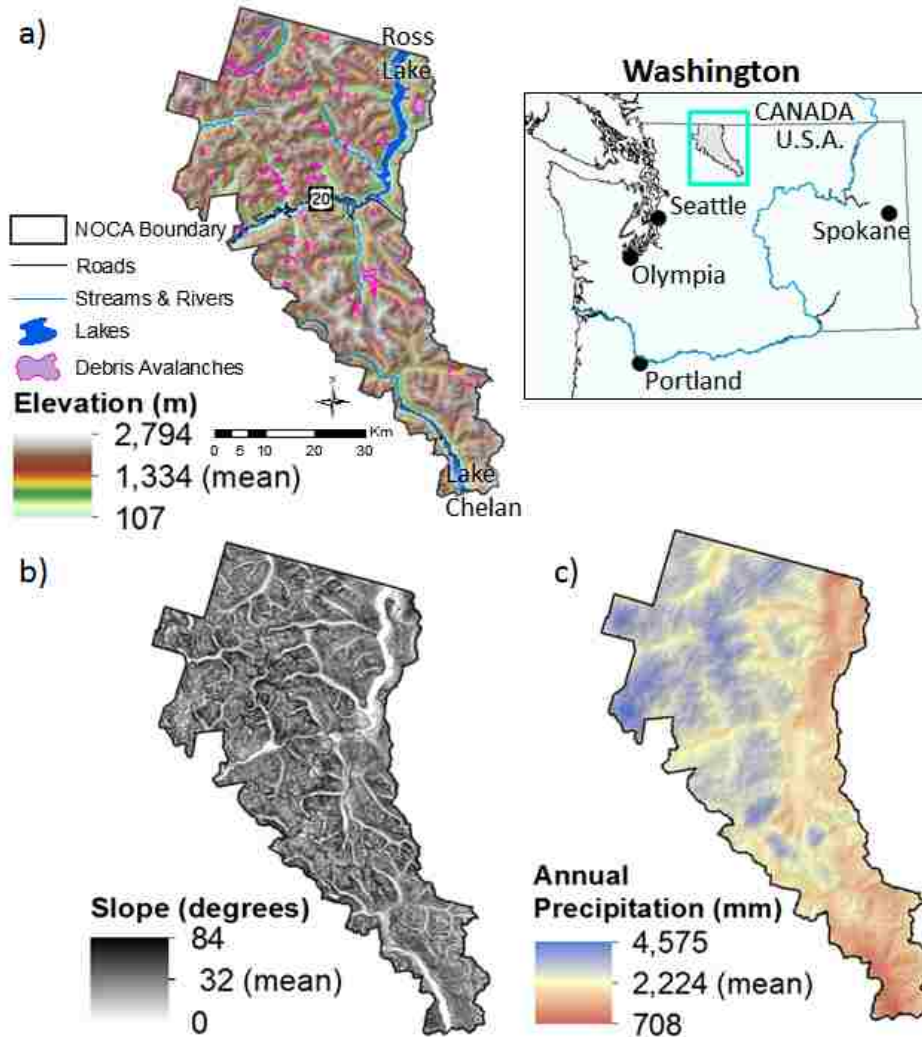


Figure 3.2. North Cascades National Park Complex (NOCA) in northern Washington state, U.S.A: (a) a 30-m DEM of the domain overlain by debris avalanches and major water bodies; (b) slope derived from DEM; and (c) mean annual precipitation (1981-2010 average) mapped at 800-m resolution from PRISM (PRISM Climate Group, 2004).

Some areas in mountainous regions are covered by glaciers, permanent snowfields, and exposed bedrock, which are unsuitable locations to model landslides on soil-mantled hillslopes using the infinite slope model (Borga et al., 2002). Furthermore, they are not expected to be destabilized by precipitation, although other forces could cause failures (e.g., earthquake, volcanic activity, and temperature). We exclude high elevation areas covered by glaciers, permanent snowfields and exposed bedrock (Fig 3.3c), as well as wetlands and other water surfaces, based on landform mapping and maps of lithology and LULC, from our modeling domain and geomorphic analysis because shallow landslides are not typically observed on these landforms. The total area excluded from the stability analysis accounts for about 21% of NOCA's land area.

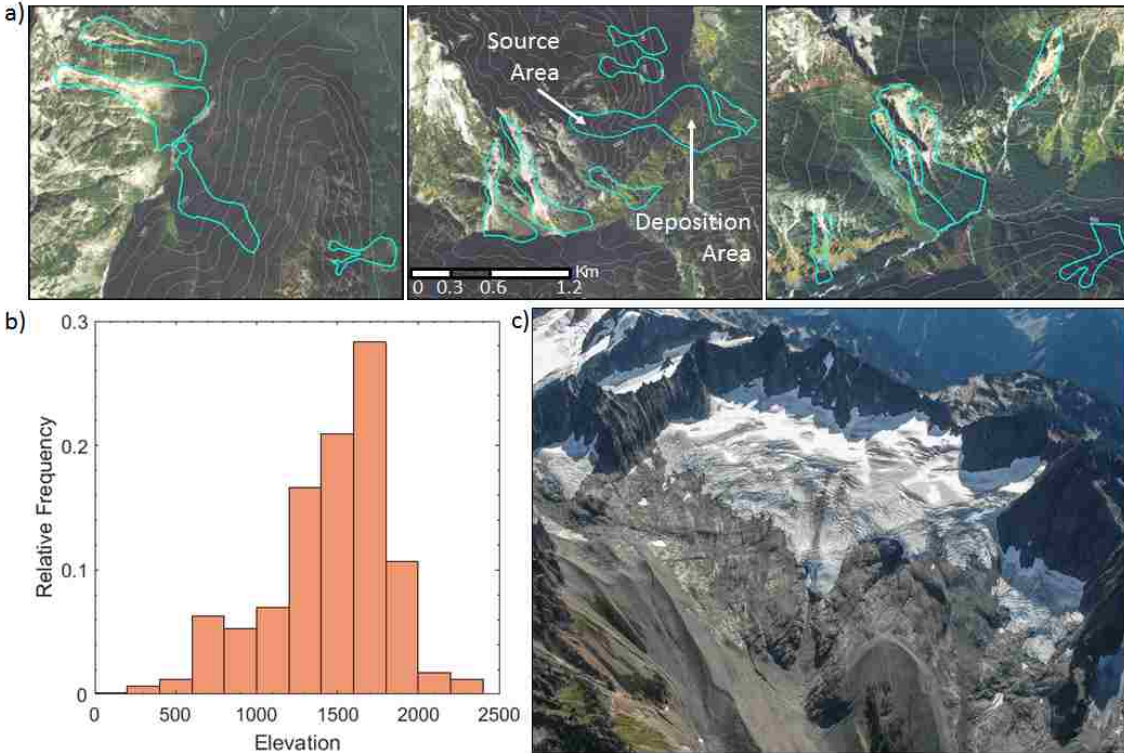


Figure 3.3. (a) Example debris avalanches (cyan) mapped in three areas within NOCA. Contours are in 100-m intervals. Aerial image source from World Imagery, Esri Inc.¹; (b) elevation distribution of the relative frequency of mapped debris avalanche source areas (upper 10%); and (c) High elevation rock and glacier mapped surrounding Spiral Glacier in North Cascades showing a bedrock glacier cirque with thin barren soils and moraine deposits (photo by John Scurlock with permission).

3.3.2 Model Input Fields

We used a grid resolution of 30 m to evaluate and compare our regional model of landslide probability to a limited set of landslide observations. A 30-m grid cell size is consistent with the minimum mapping unit used for landslides (Riedel et al., 2015; see also Regmi et al., 2014). Slope ($S = \tan \theta$), combined curvature (Curv), and contributing area (CA) attributes were derived from a 30-m DEM acquired from *National Elevation Dataset* (NED) (USGS, 2014a) (Fig. 3.2a). In addition, the NLCD data for vegetation classification and the SSURGO soils database we used in this study both have available 30-m grid resolutions. To show the model potential for regional applications, a global coverage of 30-m DEM from the NASA Shuttle Radar Topography Mission (SRTM) is available (USGS 2017). Thus, showing the model’s potential at this resolution is intended in this paper, especially for regional applications beyond the use in a single watershed across the globe.

3.3.2.1 Vegetation and Soil parameters

Parameters of a triangular distribution for C , ϕ , T , and h_s are provided in Table 1. In our case study, C represents root cohesion because we assumed soils to be primarily cohesionless, due to

¹ Images created using ArcGIS® software by Esri. ArcGIS® and ArcMap™ are the intellectual property of Esri and are used herein under license. Copyright © Esri. All rights reserved. For more information about Esri® software, please visit www.esri.com.

low clay content in this mountain substrate. We developed spatial coverages for minimum, mode, and maximum C for NOCA by relating vegetation classes with corresponding published C values in the literature (Table 1), where field observations suggest right-skewed distribution (Hammond et al., 1992; Schmidt et al., 2001; Gabet and Dunne 2002; Hales et al. 2013). Based on ranges available in the literature, we selected a mode value as a commonly reported value, minimum parameter as 30% of the mode, representing death and loss of productivity (Sidle, 1991; 1992), and a maximum near the highest reported value for C. Other LULC types include water, wetland, snow/ice, barren, and developed (e.g., roads, campground). Small C values are assigned for barren and developed land uses (~14% of the domain) having minimal vegetation. Mode values of C mapped over NOCA are given in Fig. 3.4b.

Table 3.1. Parameters defined for vegetation and soil types in the study region. For spatially continuous parameters, values represent the statistics for the model domain with (*mean*) values in parentheses.

Parameter	Minimum	Mode (<i>Mean</i>)	Maximum
Root Cohesion [kPa]			
Barren/Developed	0.03	0.10	0.15
Forest (coniferous)	3	10	20
Shrubland	1.2	4	10
Herbaceous	0.6	2	5
Internal angle of friction [°]¹			
Loamy sand	26.2	32	42.2
Sandy loam	28.7	35	46.2
Developed areas (loamy, sandy)	28.7, 31.2	35, 38	46.2, 50.2
Transmissivity [m² d⁻¹]²	0.42	(3.39)	16.4
Soil depth [m][†]	0.09	(0.62)	2.01
¹ Developed areas within the two soil types, respectively, have mode values 3° larger due to compaction.			
² Values for the continuous variables, transmissivity and soil depth, represent the minimum, mean, and maximum for the study area, not individual soil map units.			

Despite the aggregation of plant types into functional plant communities (Fig. 3.4a), considerable spatial variability in C is present within the park (Fig. 3.4b), with the greatest values in the forest communities of the valley bottom and lower valley walls. As communities transition from forest to shrublands to herbaceous species with increasing elevation, C declines. Note that herbaceous species are likely composed of considerable woody vegetation in this alpine region, but of diminutive stature.

In order to investigate the contribution of soil depth to mapping landslide probability, we developed and used two alternative soil depth products. The nationally available SSURGO database maintained by the Natural Resources Conservation Service (NRCS) is a readily available data source that includes depth-to-restrictive layer (*DOA-NRCS* 2016), which we used to specify the mode of soil depth (Fig. 3.4c). Using the *Soil Data Viewer* of Esri ArcGIS (*DOA-NRCS*, 2015a), the weighted-average aggregation option is used to extract soil depth within each soil map unit (*DOA-NRCS* and *DOI-NPS*, 2012). SSURGO soil depth (*SSURGO-SD*) is uniform for each soil map unit and thus, lacks finer scale spatial heterogeneity and create edge incongruities (Fig. 3.4c), a limitation also identified in other landslide modeling studies (Bordoni

et al., 2015). A smoother and spatially consistent soil depth map is achieved using the soil evolution model.

SSURGO-SD represents the recent conditions in soil depth. The difference between the actual soil depth in the field and the SSURGO reported soil depth will likely be associated with the limited number of soil depth measurements used to develop SSURGO maps, measurement errors, and spatial interpolation assumptions. In addition, for the locations that have already produced landslides before SSURGO mapping, we assume that the maximum value of the triangular distribution represents the soil depth prior to a landslide. To represent uncertainty, minimum h_s is assumed to be 70% of the mode and maximum h_s adds 10% to the mode value. These values give a left-skewed triangular distribution, commonly used in probabilistic landslide models (Hammond et al., 1992). Selected ranges were confirmed by the soil evolution model discussed in Sect. 3.1.2.

Transmissivity is derived as the product of weighted-average aggregated K_s of all soil layers above the restrictive layer and h_s for each soil map unit (DOA-NRCS, 2015a). Similar to h_s , this T value was considered the mode (Fig. 3.4d) and the minimum and maximum values needed for an asymmetrical triangular distribution calculated as: $T_{\min} = T_{\text{mode}} - 0.3 * T_{\text{mode}}$ and $T_{\max} = T_{\text{mode}} + 0.1 * T_{\text{mode}}$. Closely related to soil depth, transmissivity is high in valley bottoms as well on plateaus because of deeper soils, thus, more water can move through the soil when saturated (Fig. 3.4d). Transmissivity is low in the thin veneer soils below retreating glaciers as well on steeper side slopes.

Soil surface texture is a grouping used to describe the particle size distribution of granular media, and can be used as an indicator of ϕ (Nimmo, 2005). The percent sand, silt, and clay (weighted-average aggregation) for each soil map unit in NOCA were derived from SSURGO data using Soil Data Viewer (DOA-NRCS, 2015b). This revealed largely sandy loam or loamy sand soil textures, based on USDA classification, across the NOCA. These soil textures corresponded to Unified Soil Classification System (USCS) soil types silty sand and well-graded (diverse particle size) fine to coarse sand, respectively. Reported ϕ values for these USCS soil types were assigned as the ϕ_{mode} (i.e., Table 5.5 in Hammond et al., 1992 and Table 5.2 in Shelby, 1993). Developed land cover type was assigned an additional 3° to the mode to compensate for higher soil density from development activity, such as compaction (Sidle and Ochiai, 2006). The map of ϕ exhibits the least variability in NOCA due to the relatively narrow range of soil textures, with lower angles typical at higher elevation and higher angles farther downslope (figure not shown). Given the mode and ranges of ϕ for these soil types, minimum and maximum ϕ were calculated to generate right-skewed distributions for both soil types as: $\phi_{\min} = \phi_{\text{mode}} - 0.18 * \phi_{\text{mode}}$ and $\phi_{\max} = \phi_{\text{mode}} + 0.32 * \phi_{\text{mode}}$. The soil and water density terms in Eq. (1a), were assigned a constant value of $2,000 \text{ kg m}^{-3}$ and $1,000 \text{ kg m}^{-3}$, respectively (Pack et al., 2005).

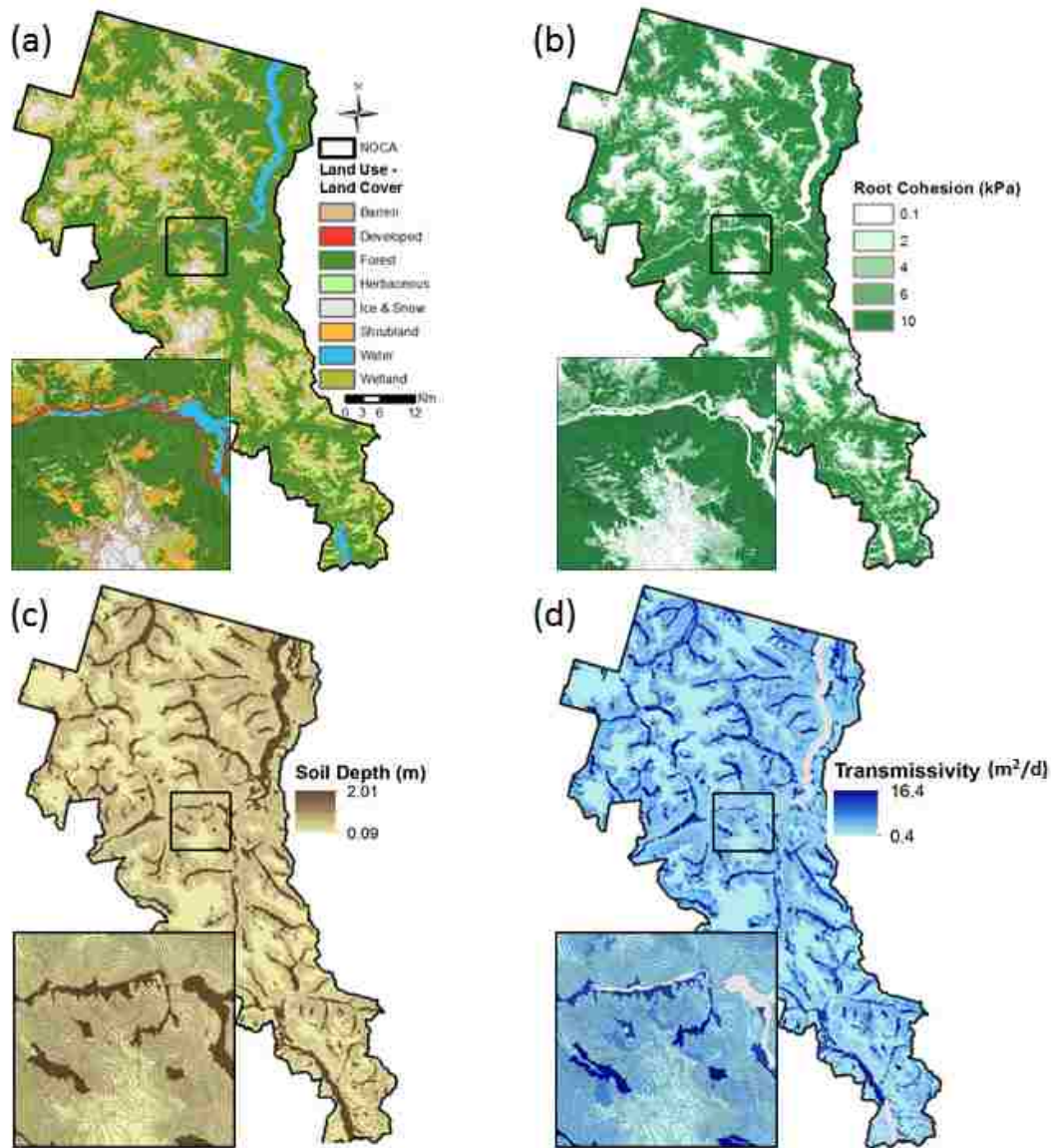


Figure 3.4. Distributed parameters used in the landslide model over NOCA, including: **(a)** LULC classified from NLCD (USGS, 2014); **(b)** root cohesion based on LULC; **(c)** soil depth from SSURGO; and **(d)** transmissivity based on SSURGO soil depth. Mapped values in (b) through (d) represent the mode values used in the parameter distributions. Insert shows zoomed-in area with 100 m contours.

3.3.2.2 Model Recharge

The model is designed with a flexible approach to parameterizing recharge. Available probability distributions include uniform, lognormal, lognormal spatial, and data driven spatial.

Supplemental materials include a Jupyter Notebook that reproduces these four recharge options on a synthetic grid. To provide the hydro-climatology forcing to drive our landslide model, our model application leverages the existing detailed simulations of VIC in the PNW region developed through the *Columbia Basin Climate Change Scenarios Project* (Elsner et al., 2010; Hamlet et al., 2013). The project developed a calibrated implementation of VIC (1/16° or 5x7 km grid resolution) covering the Columbia River basin in Washington to produce validated

historical hydrologic simulations (water years 1916-2006) driven by spatially interpolated daily station observations of temperature and precipitation (Hamlet et al., 2013). Archived model output at a daily-time-step includes gridded baseflow and runoff. Hydrologic simulations using VIC have also been run for all of the contiguous United States (CONUS; Livneh et al., 2013, 2015). Thus, acquisition of hydrologic model output is readily available to apply the landslide model anywhere throughout the CONUS. We determined the maximum daily recharge for each year to generate a 91-year long time series to calculate the annual highest pore-water pressure at each VIC grid cell. Modeling with maximum recharge provides an indicator of individual storm events that typically trigger shallow landslides (Lu and Godt, 2013), although lesser amounts of recharge may also be sufficient to trigger landslides in some locations.

3.4 Results and Discussion

3.4.1 Geomorphic Analysis and Soil Evolution

Understanding the spatial distribution of dominant geomorphic processes can aid the development of landslide hazard maps consistent with geomorphic theory. In this section, we discuss the mapping of dominant processes on the landscape on the slope and area domain, and explore the proposed soil evolution model to develop modeled soil depth maps.

3.4.1.1 Investigation of Process Domains

Hillslope diffusion, landslide, debris flow, and fluvial transport processes leave unique imprints on landforms, manifested in the slope-contributing area (S-CA) domain as different scaling relationships (Montgomery and Dietrich, 1992; Tucker and Bras, 1998; Montgomery, 2001; Stock and Dietrich, 2003; Tarolli and Fontana, 2009). The infinite-slope factor-of-safety model is only applicable to the initiation of landslides. Therefore, hazards associated with debris flow scour and deposition cannot be predicted by this model. We used a S-CA plot and the infinite slope stability theory to: (1) identify process domains and limit the analysis of the landscape to slopes where there is shallow landslide potential, (2) evaluate observations of debris avalanches to identify landslide source areas, and (3) infer plausible ranges of the infinite slope stability model parameters to corroborate those we compiled from the literature for NOCA (Table 1).

Our geomorphic analysis was based on plotting, in log-log scale, S, (as $\tan(\theta)$), and CA pairs of each DEM grid cell in NOCA, cells within mapped debris avalanches (including depositional areas), and most likely source areas of landslides identified as the single highest elevation grid cell within each mapped debris avalanche (Fig. 3.5). The general trend in the S-CA relationship is acquired for all grid cells of NOCA as well as debris avalanche (DA) cells by binning the data with respect to CA and calculating the mean S for each CA bin. The negative linear relation in the log-log plot suggest a power-law scaling in the form of $S \sim CA^{-B}$ where B is the slope of the S-CA relation on the log-log domain, which reflects channel longitudinal profile concavity.

Concavity is generally associated with the role of discharge (CA is used as a surrogate in this plot) in enhancing sediment transport, while the degree of concavity is tightly related to how nonlinear the dominant transport is with respect to S and CA (Roering et al, 1999; Montgomery 2001; Istanbuluoglu 2009). Geomorphic process domains interpreted from the binned S-CA plot portrayed in Fig. 3.5 include: (1) a hillslope zone where slope-dependent processes such as dry ravel and soil creep dominate, leading to convex slopes, (2) a landsliding zone where pore-pressure driven slope failures introduce concavity as landslides arise with shallower slopes as recharge CA grows, (3) a debris flow or saturated landslide zone in headwater channels where

mass wasting processes are supplemented with higher fluidity and ground saturation leading to S and CA driven high-concentration transport (Iverson et al., 1997), and (4) a fluvial region where stream-dominated erosion and transport processes ensue (Montgomery and Foufoula-Georgiou, 1993; Tucker and Bras, 1998). Dominant process domains in the S-CA plot are identified by visual inspection of the scaling transitions that mark changes in concavity. It is well documented that debris flows show reduced concavity relative to both channels and pore-pressure driven landslide zones in the S-CA domain (Montgomery and Foufoula-Georgiou, 1993; Tucker and Bras, 1998; Stock and Dietrich, 2003). The highest profile concavity results from fluvial transport (Fig. 3.5).

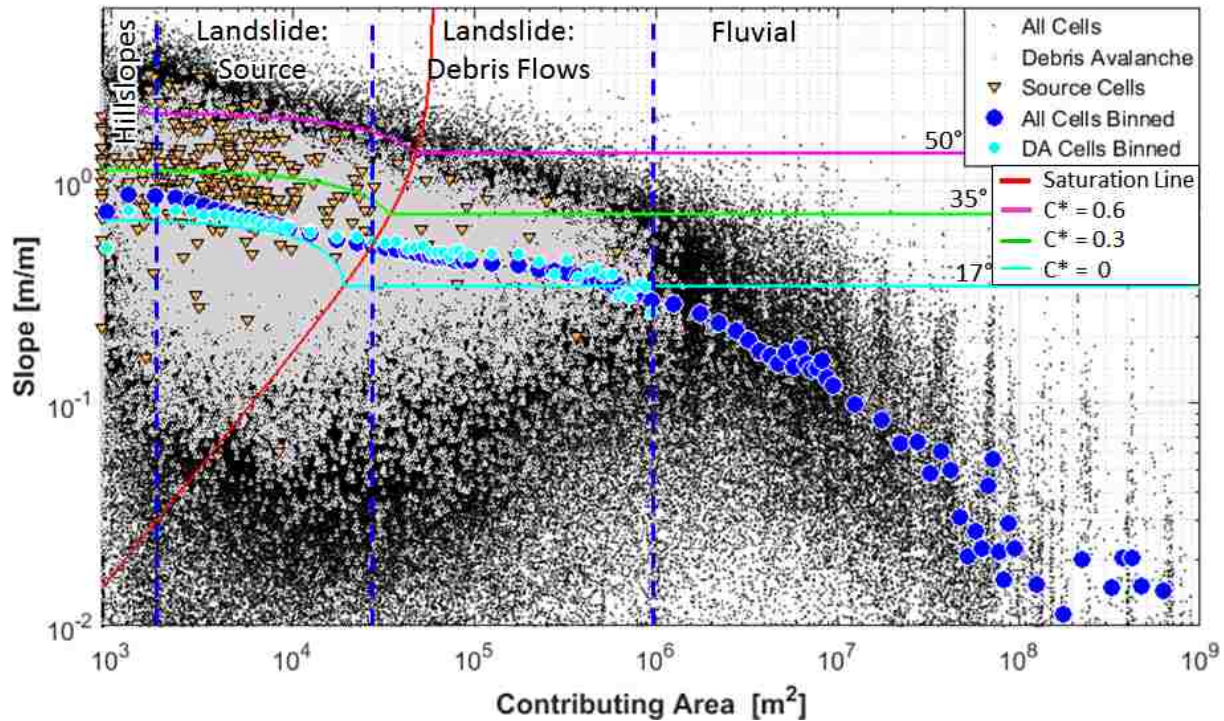


Figure 3.5. Slope-contributing area (S-CA) plot for North Cascades National Park Complex. Mean S for bins of CA are indicated by blue dots and cyan dots for all cells and debris avalanche (DA) cells, respectively. DA source cells (orange triangles) are the single highest elevation grid cell within mapped debris avalanches (gray). Slope stability curves plot the solution of Eq. (1a) for FS=1, given C^* and $\theta=34^\circ$. Above each curve landscape is unstable for a given C^* . Saturation line (red curve) separates partially saturated areas (left) from saturated areas (right). Vertical lines divide the plot into geomorphic process domains in relation to CA of the landscape (e.g., Montgomery 2001). Cyan horizontal line at 17° generally separates potential landslide dominated areas from fluvial dominated areas.

A threshold CA of approximately 1 km^2 and a slope threshold of $\theta=17^\circ$ generally separates colluvial mass wasting and debris transport processes from fluvial processes (Fig. 3.5; see also Legg et al., 2014). Nearly all grid cells within mapped debris avalanches plot to the left of the 1 km^2 dashed line. An average θ value of 17° may also correspond to a low-end of a slope threshold for landsliding. Fully saturated cohesionless soils are unconditionally stable at $\tan(\theta) \leq \frac{1}{2} \tan(\theta)$ (i.e. half of θ), assuming a ratio of water to saturated soil density of 0.5 (e.g., Montgomery and Dietrich, 1994). Solving for θ when $\theta = 17^\circ$ gives 34° , generally consistent

with selected ϕ values from soil texture (Table 1) (Hammond et al., 1992). Approximately 85% of NOCA landscape lies above $\theta > 17^\circ$, suggesting a dominant role of mass wasting processes in this landscape. We included areas above this slope threshold in our landslide model domain.

The red saturation curve is calculated as aR/T , where R/T is calibrated to 0.0005 m^{-1} (e.g., $a/\sin\theta = 2000 \text{ m}$) to capture most of landslide source cells (left of curve) and a scaling break in the binned S-CA plot (Fig. 3.5). The saturation curve partitions the landscape into partially saturated (left) and saturated (right) areas, which generally delineates the S-CA pairs separating landsliding from debris flow tracks that form under full soil saturation. For a $T = 10 \text{ m}^2 \text{ d}^{-1}$, R is 5 mm d^{-1} , which is within the range of the lowest maximum annual modeled recharge values in most of the study area, indicating that the plotted saturation line could reasonably map regions that experience saturation annually.

The three lines stacked vertically plot the solution of S in the infinite slope stability equation (Eq. 1a and 2) as a function of CA, and given $FS=1$, $R/T=0.0005 \text{ m}^{-1}$, $\phi=34^\circ$ and select values of dimensionless cohesion, C^* . Conditioned on the C^* value, slopes that plot above the S-CA solution are unstable. Consistent with the binned S-CA data, the solution of the infinite slope stability equation curves down as a function of CA, and following soil saturation, a constant instability S threshold is reached. Root cohesion is approximately 6 kPa for $C^*=0.3$ (middle green line) and 12 kPa for $C^*=0.6$ (upper pink line), assuming a soil depth of 1 m. These root cohesion values are reasonable for shrub and mature forest vegetation found in the literature (Table 1) and they facilitate stability with steeper slopes. When $C^*=0$ (bottom cyan line), landslides initiate at lower slopes than when cohesion is greater. This solution also envelops the low slope-end of nearly all landslide source S-CA pairs identified from debris avalanche data. Only a small portion of the unstable areas plot above the $C^*=0.6$ solution of Eq. (1a), which implies areas with higher root cohesion.

3.4.1.2 Evolved Soil Depth

We ran the soil evolution model described in Sect. 3.2.4 at representative topographic conditions and used the results in a nonlinear regression analysis to estimate soil depth from slope and total curvature. As the study domain is large, we used a representative population of θ [$^\circ$], CA, and Curv values to run the soil evolution model for different vegetation types. The resulting nonlinear equations were used to estimate the mode of modeled soil depth (M-SD) of each vegetated grid cell of the study domain. Capitalizing on the S-CA analysis (see Sect. 3.1.1), θ , CA, and Curv triplets in each of the CA bins are used from the landscape dominated by colluvial transport processes ($\theta > 17^\circ$ and $CA \leq 1 \text{ km}^2$). In order to further classify landscapes within each CA bin, θ and Curv pairs are grouped into shallow ($\theta \leq$ the 10th percentile θ), moderately steep (between 10th and 90th percentiles of θ), and steep ($\theta \geq$ the 90th percentile θ) slope classes. Within each class, θ and Curv are averaged.

We ran the soil evolution model for 10,000 years to represent the postglacial landscape (i.e., roughly the current interglacial period or Holocene) using the calibrated parameters listed in Table 2, allowing soil sediments to develop from bedrock and to be removed through diffusive and mass wasting processes. We ran the soil model for the three slope classes and for mature

forest, shrubs, and herbaceous root cohesion (Table 1). Mean and mode soil depth were calculated for a given θ , CA, and Curv for each vegetation type.

Table 3.2. Model parameters used in the soil evolution model

Parameter	Value	Units
h(initial) – initial soil depth	0.01	m
α – rate of exponential decay with depth	3	m ⁻¹
Po – soil production rate from exposed bedrock	0.0005	m yr ⁻¹
Kd – linear hillslope diffusion coefficient	0.01	m ² yr ⁻¹
ρ_r / ρ_s – Rock to soil density density	2.65/2	[-]
Ks – saturated hydraulic conductivity	7	m d ⁻¹
ϕ – internal angle of friction	35	Degrees
Root cohesion ¹	Varies	kPa
Recharge (mean) ² and Coefficient of variation	32, 0.35	mm d ⁻¹
¹ Root cohesion varied by vegetation type based on Table 1 and soil cohesion was assumed to be zero.		
² Recharge extracted from average values found at four representative VIC grid cells within NOCA.		

Both θ and Curv have been found to be correlated with soil depth (Heimsath et al., 1997; Braun et al., 2001; Mitchell and Montgomery, 2006; Hren et al., 2007). A multivariate nonlinear regression in the form of $y = \beta_1 \cdot x_1^m + \beta_2 \cdot x_2 + C$ was fit to mean and mode of soil depth (predictand, y) given θ and Curv (predictors, x_1 and x_2) for each vegetation type with $R^2 > 0.9$ for all slope classes (not reported). Maps for mode of the modeled soil depth (M-SD) were developed over the portion of the NOCA domain by applying the regression equations using the distributed θ and Curv appropriate for vegetation type at each grid cell. Minimum and maximum depth were set at 0.005 and 2 m, respectively. Outside the colluvial transport process domain are conditions outside the regression analysis; therefore, vegetated areas were assigned a depth of 0.5, 1, and 2 m for herbaceous, shrubland, and forest, respectively, to generate a contiguous soil depth map for NOCA consistent with SSURGO. Areas with barren land cover were assigned a soil depth of 0.05 m, representing the minimum range of modeled herbaceous areas. Developed areas were assigned a value of 0.5 m. Areas assigned fixed values are about 2% of the model domain.

As an alternative to the SSURGO-SD, the map of the mode values of M-SD was used to represent the most likely soil depth at each grid cell in the landslide probability model. The evolved soil depth was also used to revise T , using the K_s provided by SSURGO, which provides a more-distributed continuous field of T . The revised T map is used when Landlab is run based on mode from M-SD.

Local erosion is calculated within the soil evolution model. Calibration of the soil evolution model was performed by adjusting model parameters from the literature (e.g., Tucker and Slingerland, 1997; Nicótina et al., 2011) and comparing the mean annual rock erosion rate estimated by the model to long-term average rock erosion rates published for the Cascade Mountains, which range from 0.02 to 0.5 mm y⁻¹ over roughly the last several Ma (Reiners et al., 2002, 2003) and slightly higher rates over the last millennia of 0.08 to 0.57 mm y⁻¹ (Moon et al., 2011). In addition to published erosion rates, the resulting soil depths were compared to the SSURGO-SD, which ranged from 0.09 to 2.01 m across NOCA.

Modeled erosion rates ranged from 0.037 to 0.49 mm y⁻¹, consistent with published rates as determined by mineral cooling ages (Reiners et al., 2002, 2003; Moon et al., 2011). In Fig. 3.6 we show modeled mean annual erosion rates in relation to modeled mode soil depth for a steep and moderate slope class, and illustrate the local variability of M-SD under forest and shrub conditions. The relative frequency histogram of soil depth resembles a triangular distribution, with mode values generally higher than mean values, indicating a negatively (left) skewed distribution for soil depth (Fig. 3.6a, c). Therefore, there is a higher frequency of deeper soil relative to shallower soils for a given soil distribution. Soil creep fills hollows, thickening soils, as FS gradually drops, leading to episodic landslides that evacuate sediment (Fig. 3.6b, d).

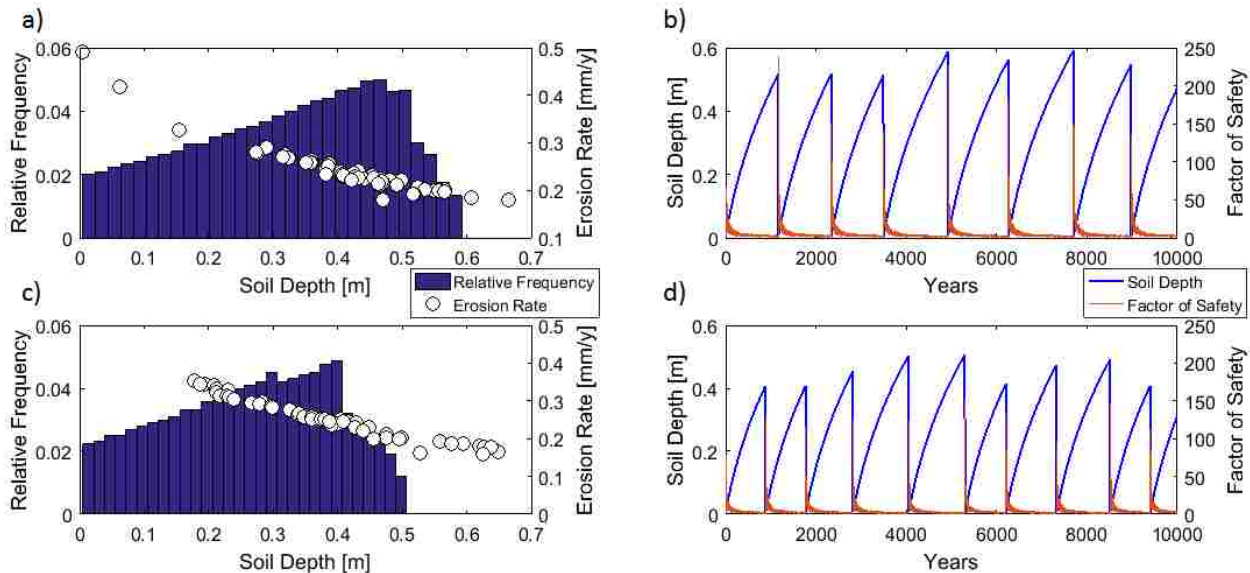


Figure 3.6. Illustration of the soil evolution model run using (a, b) steep slope class and forest vegetation and (c, d) moderately steep slope class and shrub vegetation. (a, c) Modeled mean annual erosion rates plotted with respect to soil depth, along with soil depth histogram for a representative convergent location. (b, d) Temporal evolution of soil depth and FS for a representative convergent location with: (a) S=40° and Curv=-0.01; and (b) S=29° and Curv=-0.01.

Comparison of the SSURGO-SD with the M-SD indicates that there is value in a long-term geomorphic perspective in supplying a spatio-temporal soil depth. M-SD exhibits substantially more spatial variability than the SSURGO-SD (Fig. 3.7). While both soil depth distributions have similar median values, M-SD has a wider distribution with a higher proportion of shallower and deeper soils than SSURGO-SD. In general, the M-SD is shallower than SSURGO-SD on steeper, convex hillslopes with herbaceous or shrub vegetation and deeper on gentler, concave hillslope with forest vegetation. For both models, soil depth is greater in the valleys and shallower near the ridge tops (Fig. 3.7c, d), consistent with other reporting (Anagnostopoulos et al., 2015; Montgomery and Dietrich, 1994).

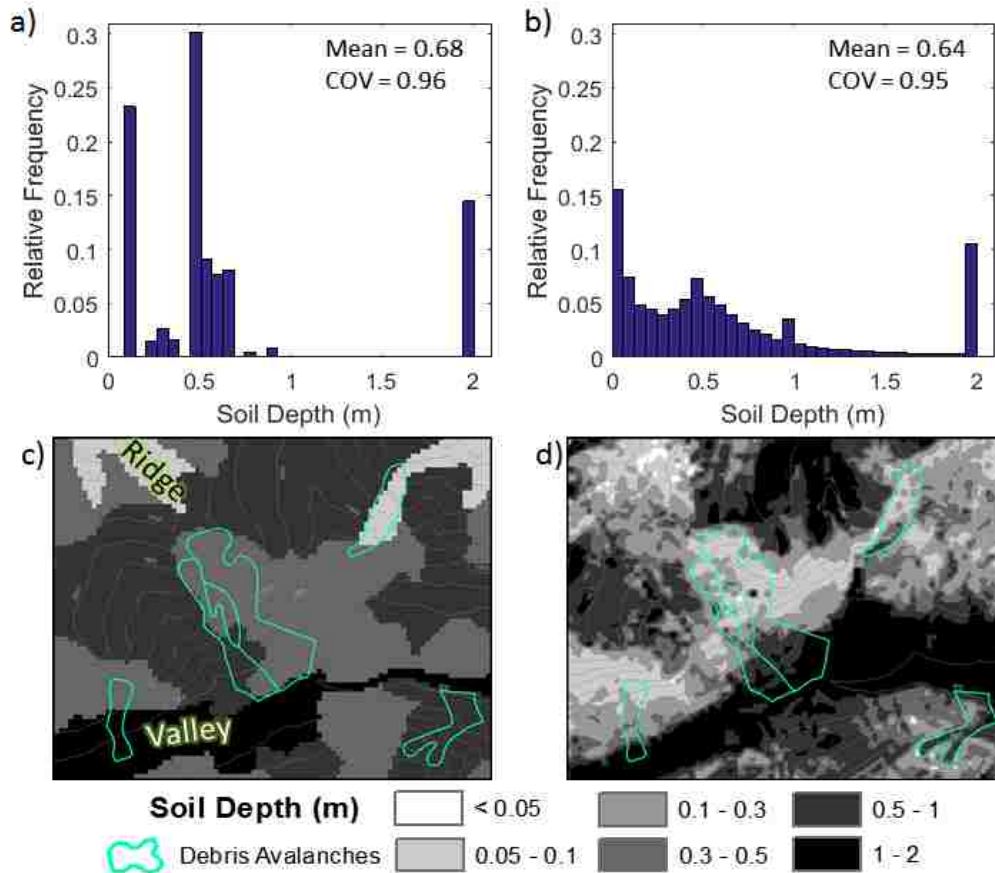


Figure 3.7. Relative histograms of soil depths within NOCA: **(a)** SSURGO-SD and **(b)** mode of M-SD, with respective spatial mean and coefficient of variation (COV). Example location ($\sim 6 \text{ km}^2$) within NOCA: **(c)** SSURGO-SD and **(d)** M-SD. Mapped debris avalanches are outlined in cyan and contours are at 100-m.

The maximum and minimum soil depth parameters of the triangular distribution to characterize soil depth variability were obtained by analyzing soil evolution model results. At most θ , CA, and Curv triplets using in the soil evolution model, a landslide occurred at least once. Given the negatively-skewed nature of the temporally evolved soil depth, maximum evolved soil depth was set equal to 10% of the mode in all model simulations. Two M-SD scenarios were developed to compare with SSURGO-SD reflecting existing contemporary and long-term soil depths. In SSURGO-SD and M-SD simulations we set the minimum parameter as 70% of the mode. However, for a long-term evolved soil depth (M-SD LT), if the minimum was greater than 0.005 m, the minimum soil depth was set to 0.005 m, reflecting the effect of landslides over a long term. This introduces a temporal uncertainty component to modeling landslide probability, which can be used to more accurately estimate landslide return period.

3.4.2 Probability of Failure

Modeled annual probability of failure of shallow landslides, $P(F)$, for NOCA simulated by the Landlab LandslideProbability component using SSURGO-SD and two M-SD scenarios are shown in Fig. 3.8. In each run 3,000 values were sampled for model parameters at each grid cell in the Monte Carlo simulations.

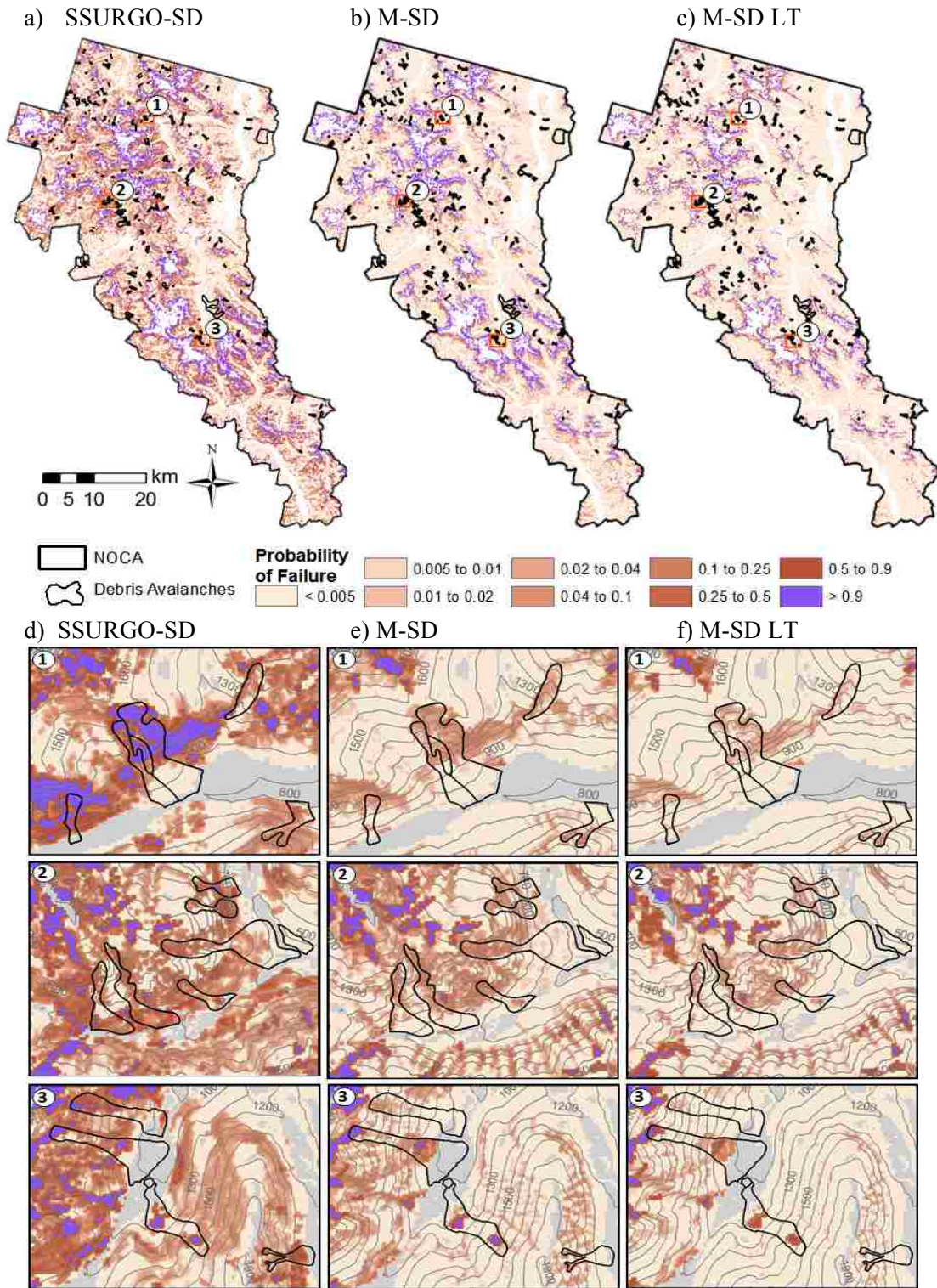


Figure 3.8. Landslide annual $P(F)$ map for NOCA overlain with mapped debris avalanches for simulations with: (a) SSURGO-SD; (b) M-SD; (c) M-SD LT. Zoomed-in areas are shown for greater detail in the lower panel in the same order and according to number designated. Purple areas are considered chronically unstable and areas excluded from analysis are shown as gray. Contours are at 100 m. Aerial images of zoomed-in areas are provided in Fig. 3.3.

P(F) derived from simulations exhibit low probabilities where slopes are moderate and cohesion is high (e.g., forest). Highly unstable areas largely correspond to steep barren landscape mostly located below retreating alpine glaciers, with steep glacial landforms, transitioning from glacier to colluvial processes (similar to Guthrie and Brown 2008; Tarolli et al., 2008; Legg et al., 2014) (Fig. 3.9). Barren areas cover ~13% of the modeled domain. These areas with a thin veneer colluvium, except for moraines, appear to be “continuously sliding” (Borga et al., 2002) or “chronically unstable” (Montgomery, 2001), which also impedes the colonization of vegetation (Dietrich et al., 1995; Istanbuluoglu and Bras, 2005). Shallow soils can enhance the probability of saturation, leading to high pore-water pressure and saturated overland flows with moderate storms (Pelletier and Rasmussen 2009). Mass wasting activity in barren areas were not completely included in our landslide inventory as they exhibit chronic small-scale slides that do not pose major risks or substantial deposition zones.

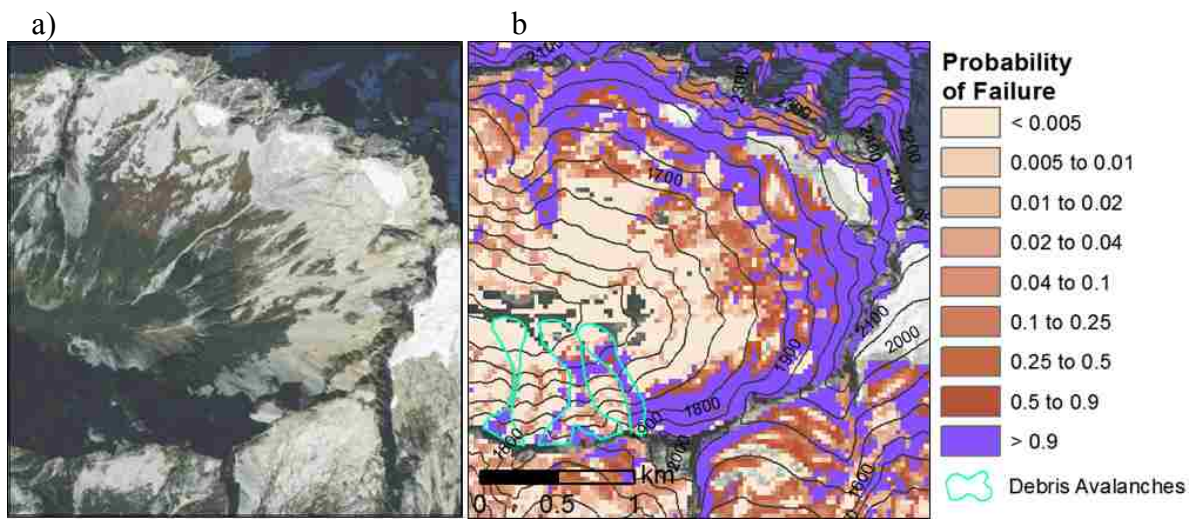


Figure 3.9. Illustration of highly unstable steep areas: (a) High resolution (0.3 m) imagery of a NOCA mountain (World Imagery, Esri Inc.)¹ compared to (b) P(F) simulated by M-SD with mapped debris avalanches. Contours at 100 m. Notice the barren areas below retreating glaciers with high P(F).

Other locations of higher P(F) are located in topographic hollows (Fig. 3.8, 3.9). These converging areas accumulate deeper soils, which decreases the effectiveness of root cohesion, and attract subsurface flow, leading to enhanced pore-pressure (Dietrich et al., 1995). Converging areas often correspond to the upper portions of mapped debris avalanches, which display higher landslide probabilities than the runout portions in simulations. Thus, the landslide probability visually appears to capture the source area of debris avalanches.

Substantial differences between P(F) derived with different soil depth maps are evident (Fig. 3.8 and Fig. 3.10) and corroborate previous studies showing the influence of various soil depth estimates on landslide susceptibility (Dietrich et al., 1995; Okimura, 1998). In general, probabilities are higher and more spatially extensive when the model is parameterized using SSURGO-SD compared to both M-SD scenarios. Given that other parameters are kept consistent, these differences are attributed to spatial variability of soil depth and related adjustments to transmissivity.

To investigate the spatial distribution of $P(F)$ in relation to soil depth, we plot the cumulative distribution of $P(F)$, referred to as the fraction of modeled area where $P(F)$ is less than or equal to a given value, for each simulation (Fig 3.10a). We present our general observations of the spatial distribution of $P(F)$ in the order of SSURGO-SD, M-SD, and M-SD LT as depicted in Fig 3.8. Simulations show approximately 26%, 38%, and 49% of the modeled domain (79% of NOCA, where $\theta > 17^\circ$) as stable (i.e., $P(F)=0$) under the current vegetation cover and climate. We refer to these sites as unconditionally stable (i.e., stable even when saturated, and with minimum C and ϕ sampled) (Pack et al., 1998; Montgomery 2001). A bimodal spatial distribution for $P(F)$ is evident (Fig. 3.10a, b). Areas with low probabilities, around $P(F) \leq 0.1$, dominate the spatial distribution of $P(F)$, manifested with a steep rise in the fraction of area from $P(F)=0$ to $P(F)=0.1$ (Fig 3.10a). For $P(F) \leq 0.1$ ($RP \geq 10$ years), the order of aerial cover for the model domain, including the stable regions, is 72%, 85%, and 87%. When the unconditionally stable areas are excluded, the percentages become 46%, 47% and 38%, respectively, for the three soil depth products used. This region approximately marks the first peak of the relative histogram of $P(F)$ (Fig. 3.10b). In the broad $0.9 > P(F) \geq 0.1$ range, the increase in fraction of area with $P(F)$ is gradual especially for the two M-SD simulations (Fig. 3.10a). In the highly unstable regions, with $P(F) \geq 0.9$ ($RP \leq 1.1$ years) as mapped in Fig. 3.8 and Fig. 3.9, the fractional area begins to rise again in all simulations (Fig 3.10a). $P(F)=1$ occupies 11% and 7% of the modeled area in the SSURGO-SD and M-SD simulations, which can be conceptually named as unconditionally unstable (i.e., unstable even when dry and with the highest combinations of C and ϕ sampled) (Pack et al., 1998; Montgomery 2001). The model run using M-SD LT soil scenario shows a smaller area percentage, ~6%, with $P(F) \geq 0.9$, while SSURGO-SD and M-SD had 16% and 10%. M-SD LT soil scenario provides a more realistic estimate as some locations are not likely to produce slope failures annually due to limited soil development. The second peak of the relative frequency histogram of $P(F)$ appears when $P(F) > 0.9$, largely associated with postglacial barren lands with steep mountain slopes, and converging topography, especially in the case of SSURGO-SD (Fig. 3.10b). Dominant factors that control the relative frequency of $P(F)$ are labeled in Fig 3.10b, and further discussed in subsequent sections.

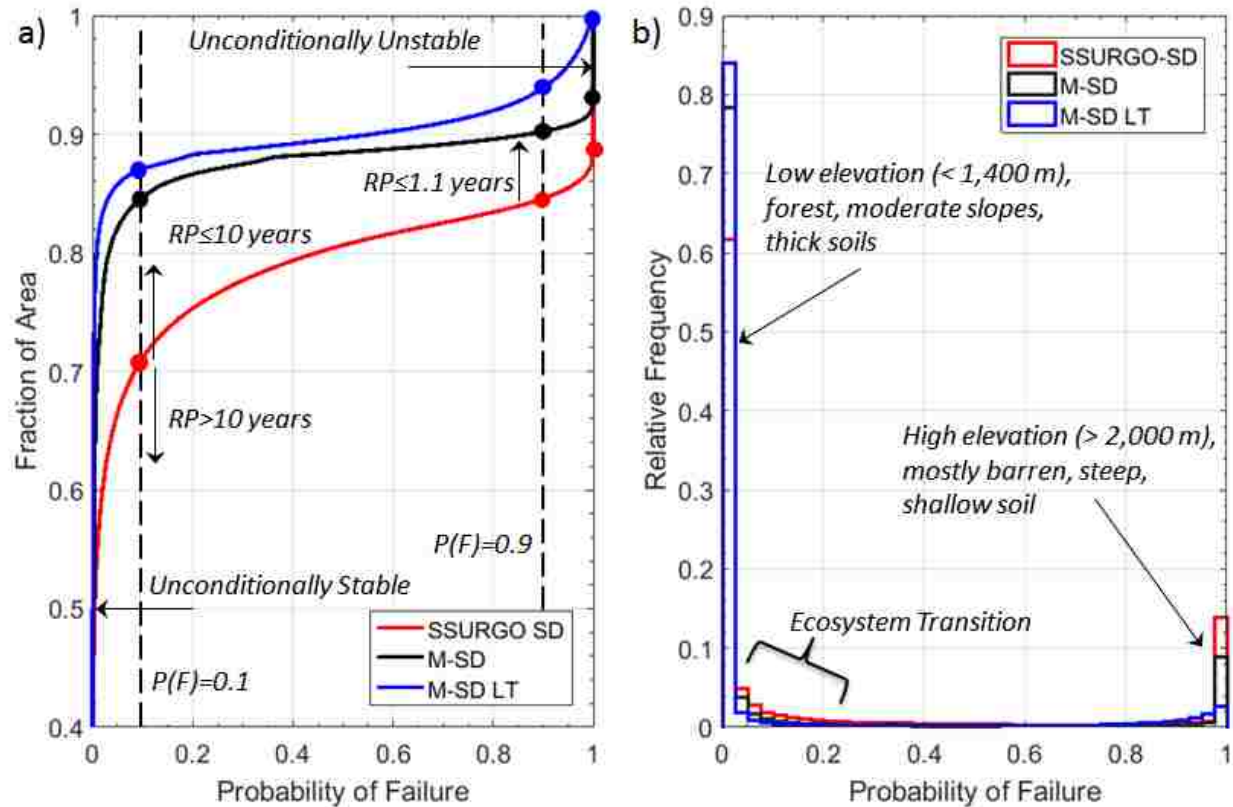


Figure 3.10. (a) Cumulative distribution and (b) relative frequency of $P(F)$ (bin size $\Delta P(F)=0.025$) mapped over NOCA from Landlab simulations using SSURGO-SD and two M-SD scenarios. Labels indicate dominant controls on the distribution of $P(F)$ in (b). Fraction of area is used for cumulative spatial probability, plotted using the Weibull plotting position. Return Period for landslides are illustrated only for SSURGO-SD.

We expressed the annual probability of landsliding in the form of a RP, plotted with respect to fraction of area for all three simulations, and mapped RPs for the M-SD LT scenario in Fig. 3.11. The M-SD LT reduces the probability and increases the return period estimates of landslide initiation, revealing the influence of long-term memory of landsliding on the probability distribution of soil thickness obtained from the soil evolution model. Therefore, the M-SD LT scenario would better suit the definition of RP, while the other two simulations provide reference for relative comparisons. In general and in concert with the $P(F)$, landslides at nearly all RPs affect a greater proportion of the domain when SSURGO-SD is used. Approximately 28% of the model domain is simulated to have a landslide return period of less than or equal to 10 years (i.e., $P(F) \geq 0.1$ or frequent slides) based on SSURGO-SD, compared to half as much area, 15%, for simulations using M-SD; M-SD LT had slightly less at 13%. Low return periods (i.e., < 10 years) coincide with steep slopes in barren areas that show chronic landsliding, low-cohesion vegetation type, such as herbaceous, as well as some steep hollows.

At the high end of the return period, 46% of the model domain was simulated to have landslides with a return period of ≥ 500 years for SSURGO-SD scenario, including stable areas, compared to 52% and 70% for model runs that used M-SD and M-SD LT scenario, respectively (Fig. 3.11). High return periods (i.e., $RP > 500$ years, $P(F) < 0.002$) are found where slopes are gentler, on divergent topography, and in forest areas. The fraction of the model domain with a landslide

return period between 100 and 500 years is 10%, 18%, and 21% for SSURGO-SD, M-SD, and M-SD LT, respectively, showing a larger fraction in the M-SD products. These landslide frequency rates relate to long-term averages and the actual failures are likely to be clustered in space and time depending on triggering event and the time since the last landslide at the same location (Guthrie and Evans, 2004).

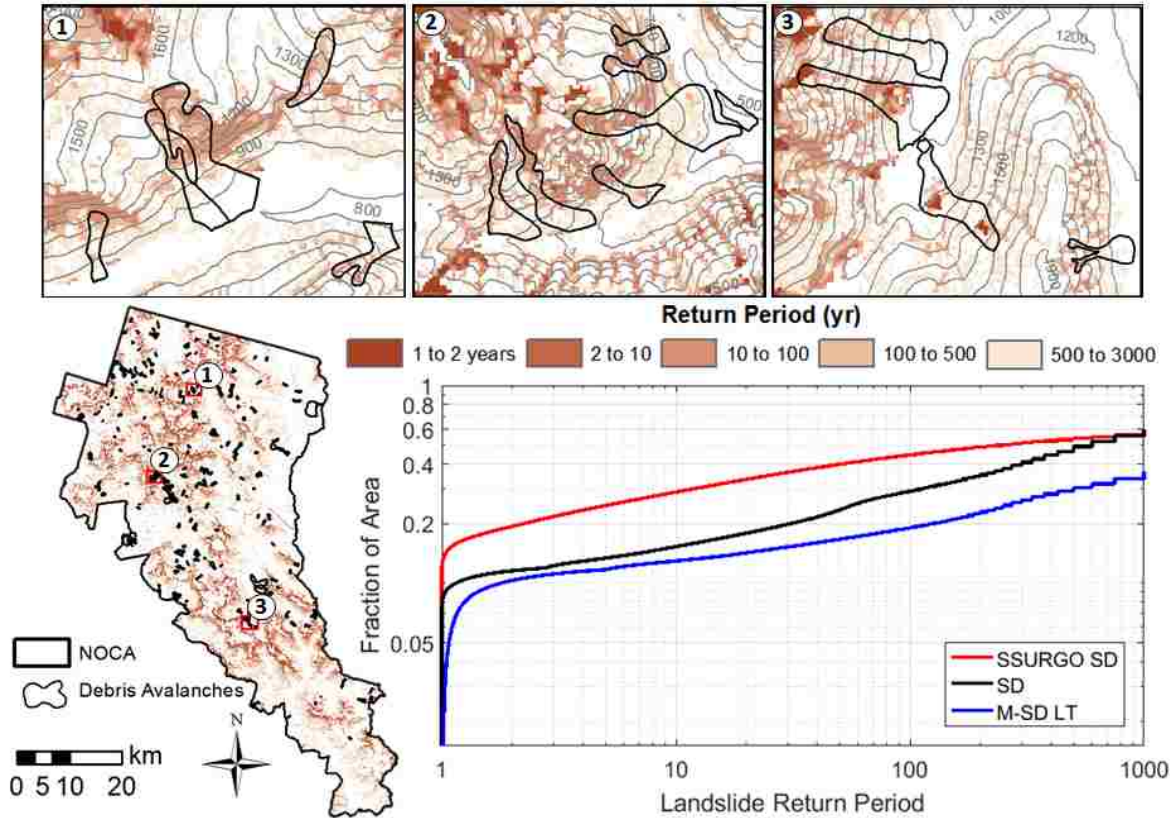


Figure 3.11. Modeled landslide return period simulations with M-SD LT for NOCA overlain with mapped debris avalanches, including zoomed in areas at top for greater detail. Cumulative distribution of return periods for SSURGO-SD, M-SD, and M-SD LT scenarios, plotted on a log-log scale using the Weibull plotting position.

As soils in landslide locations are formed by sediment accumulation from surrounding hillsides and weathering of the local bedrock, landslides can be the main source of denudation across landslide-prone regions. The expected values of mean annual denudation rate is approximated by: $\text{mean}(P(F) \cdot h_s) / (\rho_r / \rho_s)$ for each simulation. This gives spatial average of the long-term denudation rates due to landslides as 51.9 mm y^{-1} , 7.06 mm y^{-1} , and 5.04 mm y^{-1} for SSURGO-SD, M-SD, and M-SD-LT scenarios, respectively. While these rates are higher than the reported mean annual denudation rates in this region over the last millennia of 0.08 to 0.57 mm y^{-1} (Moon et al., 2011), M-SD-LT clearly gives the closest estimates to observations among the three soil depth scenarios. Over an order of magnitude variation in denudation rates is also common as part of long-term records of erosion rates (e.g., Molnar, 2004).

A critical question that remains is: what are the dominant controls that lead to the bimodal distribution of landslide probability in the modeled domain? First, we examined if topography

alone, represented by S and CA pairs, can explain this behavior. The S-CA data pairs from each model grid cell are colored by the value of P(F) in the order from low to high value using output from the M-SD LT scenario (Fig. 3.12). As slopes get steeper ($S > 0.45$ or 24.2°), a relatively rapid increase in P(F) in relation to slope from 0.4 to 1.0 can be seen, surrounded with lower probabilities. CA does not seem to impose a visually detectable increase in P(F), which is likely largely due to the wet climate in region. The landslide source cells identified from the highest elevation of debris avalanche shapefiles fall in the “eye” of this high-P(F) region in the S-CA domain. Interestingly, P(F) diminishes in the steepest slopes of most CAs. While the trend of increasing P(F) as slope gets steeper generally shows the influence of slope in Eq. (1a), landscape with $P(F) \geq 0.4$ only constitute about 11% of the model domain (Fig. 3.10a). For comparison $P(F) \geq 0.1$ was 13%. On the other hand, about 57% of the domain has steeper slopes than 24.2° ($S = 0.45\text{m/m}$). Locations with slopes less than this are rarely found with $P(F) > 0.4$. This suggest that the majority of the domain with similar pairs of S and CA exhibit lower landslide probability, which can be largely attributed to the spatial distribution and influence of vegetation type and soil depth (e.g., Roering et al., 2003).

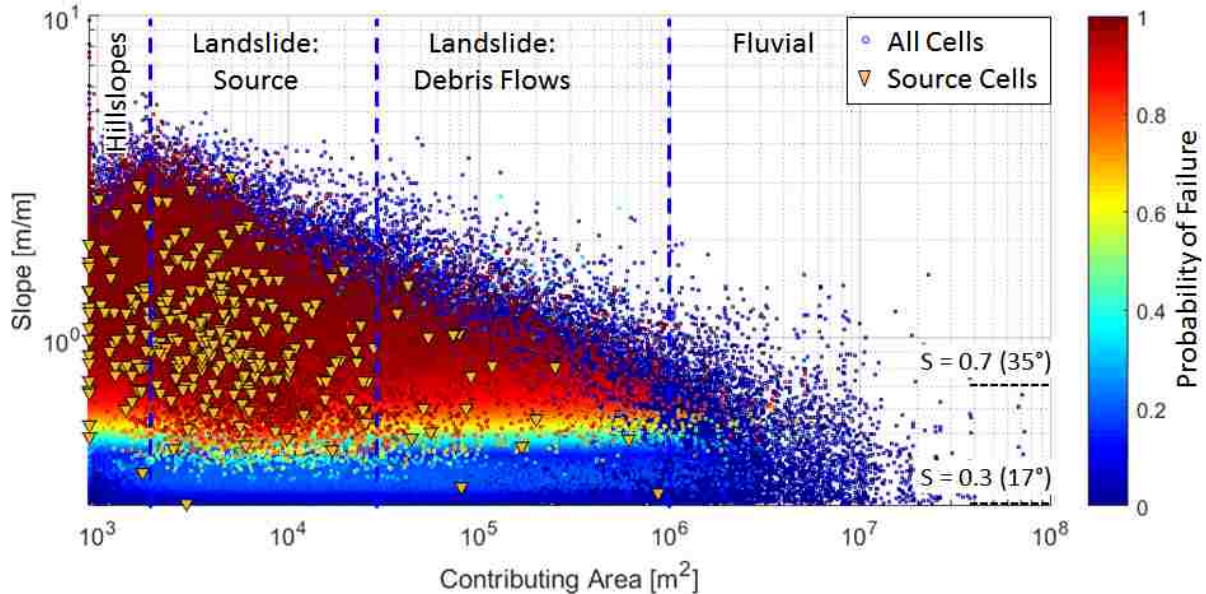


Figure 3.12. S-CA plot colored by the P(F) simulated with from the M-SD LT. Source cells (orange triangles) are the single highest-elevation grid cell within mapped debris avalanches. Comparable to Fig. 3.5. High probabilities plot over low probabilities.

We investigated the roles of vegetation, slope steepness, and soil depth on P(F) in relation to elevation (Fig 3.13). From low to high elevations, vegetation changes from predominantly forest (elevation $< 1,400$ m) to coexisting shrub, herbaceous plants, and barren land (1,400 m to 2,200 m) as a result of elevation-dependent ecoclimatic controls (e.g., temperature) on vegetation survival and growth (Fig. 3.13a). In this region of ecosystem transition, the mean P(F) shows a persistent increase from 1,400 m until a maximum is reached between 2,200 and 2,400 m, depending on simulation (Fig. 3.13b, c). Observations of debris avalanche by elevation confirm the pattern of P(F) dependence on elevation in relation to ecosystem change; 75% of the extracted landslide initiation zones from mapped debris avalanches are located between 1,200 m to 2,000 m (Fig. 3.3b). In the 1,400 to 1,900 m elevation range of the ecosystem transition zone,

mean slope is relatively constant ~ 0.75 m/m ($\sim 37^\circ$), and rises up to 0.9 m/m (42°) between 1,900 and 2,200 m (Fig 3.13c), consistent with the binned-averaged slopes of the landslide source area in the S-CA plot in Fig 3.5. Mean soil depth begins to drop in both SSURGO and modeled soil depth products above 2,200 m.

These observations confirm the strong control of ecosystem transition on landslide activity in the region. Below about 1,400 m ($\sim 40\%$ of NOCA), forested vegetation combined with deeper soils and moderate slopes keep $P(F)$ low. In the 1,400 to 2,200 m range, loss of root cohesion with ecosystem transition combined with gradual increase in landscape slopes contribute to increased $P(F)$. Above 2,200 m elevation, soils become very shallow and slopes exhibit the steepest angles in the modeled domain. This combination leads to the largest variability in $P(F)$, combining the highest $P(F)$ values, $P(F) \geq 0.9$ mostly attributed to barren areas ($\sim 6\%$ of the model domain in the M-SD LT scenario), with lower $P(F)$ values where thinner soils reduce the driving force within Eq. (1a). In aggregate, thinner soils at higher elevations lead to lower mean $P(F)$, which we referred to as soil depth control. The general contribution of elevation on the spatial organization of $P(F)$ is labeled in Fig 3.10b.

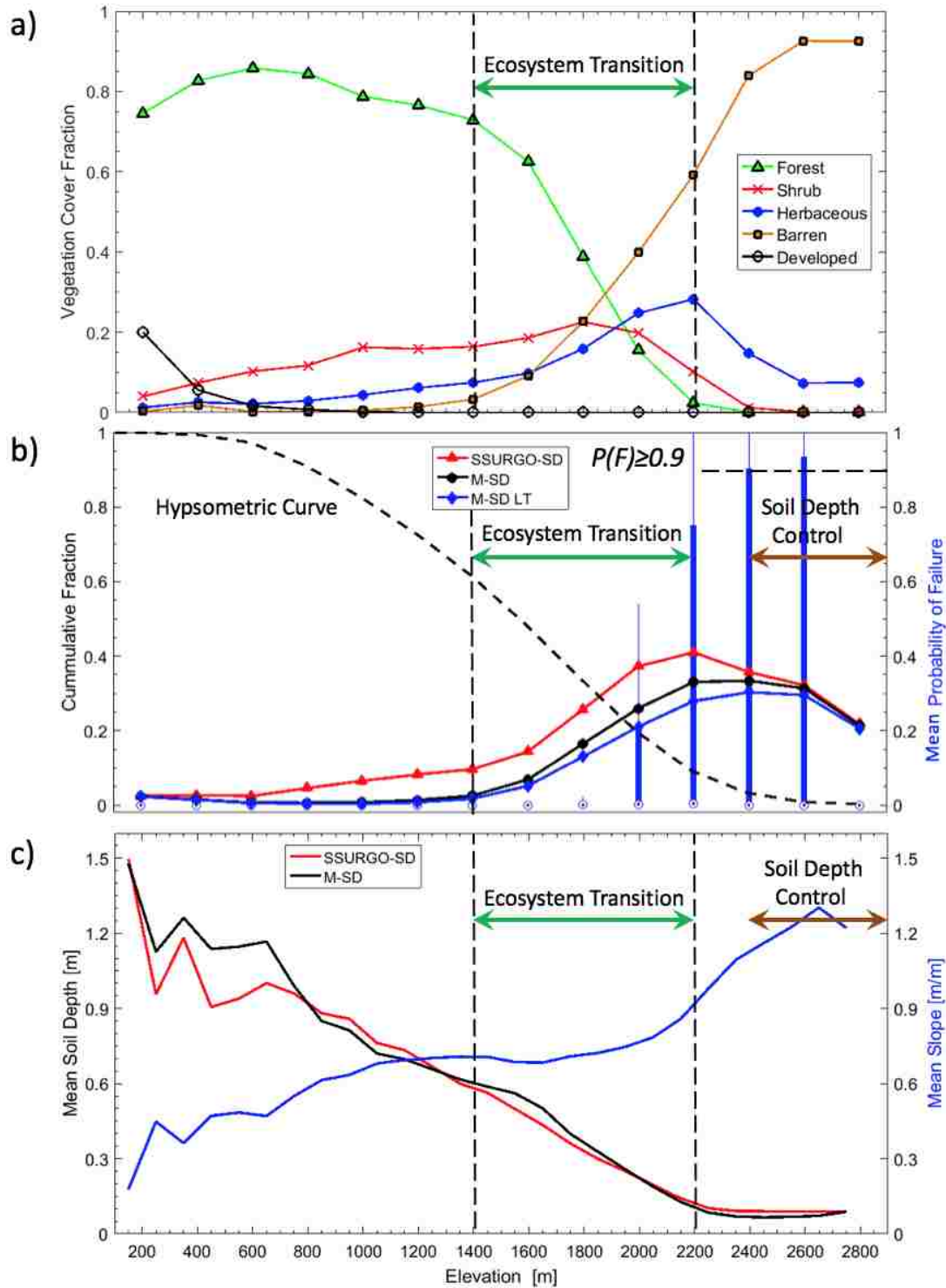


Figure 3.13. Elevation (200 m bands or bin) influence on: **(a)** vegetation cover fraction for NOCA, taken as fraction of vegetation type within each elevation band, **(b)** mean $P(F)$ using SSURGO-SD and two M-SD scenarios, along with compact box-whisker plots for $P(F)$ of M-SD LT scenario where circles-dot symbol represents median (outliers not shown, greater than 1.5 interquartile distance) overlaid with hypsometric curve for NOCA, and **(c)** mean soil depth for SSURGO-SD and M-SD products with mean slope. Mean values calculated within each 200-m elevation band.

3.4.3 Model Evaluation

The performance of a landslide model is often based on its ability to capture existing mapped landslides. In Sect. 3.4.2 we evaluated our model through visual comparison of modeled $P(F)$ to observed landslide locations (e.g., Fig. 3.8, 3.9). In this section, a more quantitative approach is presented for model evaluation. We statistically evaluated our model using multiple approaches, including cumulative distribution (CD) of $P(F)$ comparisons as well as Receiver Operating Characteristics (ROC) (Fawcett, 2006) and Success Rate (SR) curves (Bellugi et al., 2015).

For the statistical analysis, we limited our performance assessment to the source areas of the mapped debris avalanches. Source areas of debris avalanches were not mapped separately from the remaining debris avalanche features (i.e., transition and deposition zones) hindering the evaluation of model predictions (Tarolli and Tarboton, 2006). Because we anticipate that the source areas could originate from a neighboring grid cell, we considered source cells as a collection of grid cells in the upper 10, 20, and 30% highest elevation cells within each mapped debris avalanche shapefile. These populations of source cells were treated as ‘observed’ landslide source cells during validation of the landslide probability using CD, SR and ROC performance metrics. In this validation, we excluded barren areas with slopes $\geq 37^\circ$ (~5% of the model domain), which characterizes slopes of active small-scale dry landslides (failure depth \leq soil depth) more appropriately represented by nonlinear hillslope diffusion models (see Roering et al., 1999; DiBiase et al., 2010; Pelletier et al., 2013).

For comparison of $P(F)$ with source area cells, we randomly sampled 50,000 grid cells outside mapped debris avalanches (~2% of the modeled domain), similar to the number of grid cells within entire mapped debris avalanche areas. The majority of the source grid cells and outside debris avalanches cells are located at elevations between 1200 and 1800 m (Fig. 3.14a). Grid cells in the random sample outside debris avalanches were constrained to the elevation range of the source cells to allow unbiased comparison. We recognize that the areas outside mapped debris avalanches have the potential to be unmapped landslides, other landslide types, or unstable areas deficient a triggering event; therefore, we interpret the test results conservatively. We expect the simulated $P(F)$ should estimate lower probability outside debris avalanches compared to source areas of mapped debris avalanches.

At low and mid elevations, simulations generally showed a greater fraction of high probabilities in source areas compared to outside of debris avalanches (Fig. 3.14b, c). However, when only high elevation (>1,800 m) data were considered, the pattern was reversed with a larger fraction of high probabilities found outside debris avalanches than source areas (Fig. 3.14d). At this higher elevation, much of the land cover is barren or herbaceous (i.e., low root cohesion), resulting in high probabilities of failure throughout the model domain (Fig. 3.12a). While there are extensive shallow failures in these regions only limited amount of those that turned into debris avalanches were mapped. This reverse pattern is also present at mid-elevations (~1,200 to 1,800) for both M-SD scenarios, only for 10% of the sample data, when $P(F)>0.03$ and $P(F)>0.1$ for M-SD and M-SD LT, respectively (note the crossing curves in Fig. 3.14b). At low elevation (~125 to 1,200 m), there were no source areas with $P(F)>0.4$ in M-SD and M-SD LT scenarios.

The performance of the model results we are presenting in this paper are specific to a sample comparison of 10% source area of mapped debris avalanches and random sampling outside

debris avalanches. When examining the validation datasets in their entirety (i.e., regardless of elevation), the median $P(F)$ of the 10% source DA cells is 13 times the median $P(F)$ of outside DA for SSURGO-SD and four times the median $P(F)$ for M-SD; median is zero for outside DA cells in the M-SD LT. The Kolmogorov-Smirnov test (Chakravart et al., 1967) test show paired comparison between DA source area cells and cells outside DA for all three scenarios are statistically different ($p \ll 0.01$).

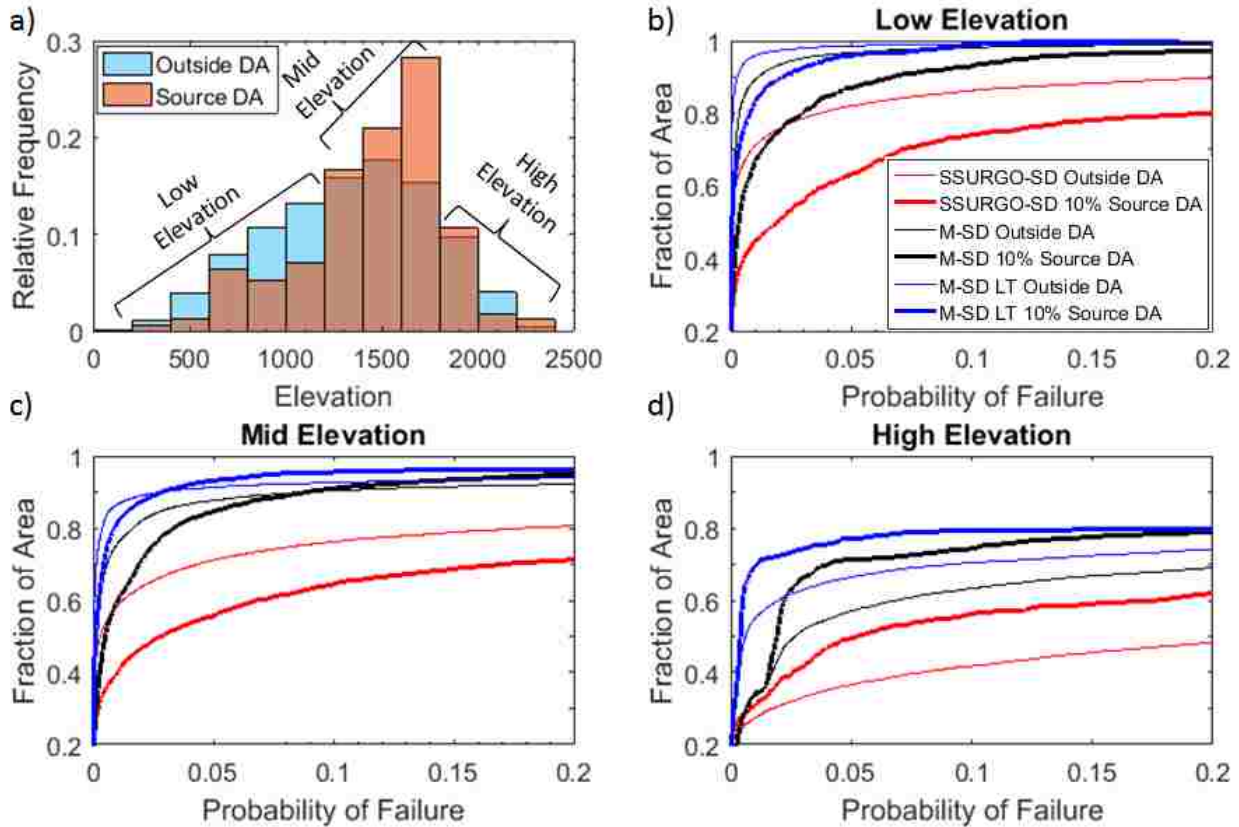


Figure 3.14. a) Relative histogram of source areas in upper 10% elevation of debris avalanches (DAs) and for 50,000 grid cells outside DAs. Cumulative distributions of $P(F)$ plots limited to $P(F) \leq 0.2$, or return period ≥ 5 years, to highlight detail in simulation using SSURGO-SD, M-SD, and M-SD LT at: b) low (<1,200 m), c) mid (1,200 to 1,800 m), and d) high (>1,800 m) elevations as depicted in a). Thicker lines represent probabilities for source areas of (DAs) and thin lines represent probabilities for cells outside DAs.

Another statistical analysis uses ROC curves to examine how our model compares with randomly distributed landslides over the landscape. These curves are constructed from confusion matrices generated from comparisons between observed and modeled landslides, based on varying $P(F)$ threshold (e.g., 0.1, 0.2, 0.3, etc.). True positives (TP) are those cases within observed landslides where probabilities are equal to or greater than threshold. False negatives (FN) are probabilities within landslides that fall below the threshold. False positives (FP) occur outside observed landslides with simulated probabilities equal to or above the threshold. True negatives (TN) are also outside observed landslides, but with probabilities below the threshold. From these metrics, true positive rate (TPR) or fraction of landslides captured and false positive rate (FPR) or fraction of false alarms can be calculated as follows:

$$TRP = \frac{TP}{(TP+FN)} \quad (8)$$

$$FRP = \frac{FP}{(FP+TN)} \quad (9)$$

The advantage of the ROC curve over a standard confusion matrix is the ability to vary the probability threshold for assigning model simulations to a modeled landslide (positive) or no landslide (negative) classification, generating different positive and negative comparisons (Mancini et al., 2010; El-Ramly et al., 2002; Anagnostopoulos et al., 2015). A better performing model will exhibit a curve toward the upper left of a FPR (x-axis) and TPR (y-axis) plot. A 1:1 line in the plot represents a trivial model that randomly assigns stable and unstable cells. The area under the curve (AUC) generated by ROC curve quantifies the performance of a model for identifying landslide and non-landslide locations. The AUC statistic represents the probability of correctly ranking a landslide and non-landslide pair randomly selected from those two datasets (Hanley and McNeil, 1982). SR curves are similar to ROC curves, with TPR as the y-axis, but compares this to the fraction of landscape predicted as unstable (x-axis), calculated as $(TP+FP)/(TP+FP+TN+FN)$. Again, a relatively well performing model would plots farther away from the 1:1 line representing a trivial model.

For this comparison, we used the same datasets used in the cumulative probability analysis discussed Sect. 3.4.2. Both simulations using SSURGO and M-SD modeled 10% source areas and non-landslide areas better than random selection as demonstrated by the curves plotted above the 1:1 line (Fig. 3.15). The classification is stronger as the source area fraction is reduced. However, the model's strength in the classification is modest as indicated by the AUC values of between 0.60 and 0.61, compared to an AUC of 1 representing a perfect classification. The TRIGRS-P probabilistic landslide model tested by Raia et al. (2014) found higher AUC results (i.e., 0.65 to 0.73). However, their study tested small areas (3 to 6 km²) that were well studied locations with detailed inventories of landslides resulting from one or two winter rainfall seasons and the entire landslide was tested rather than source areas only.

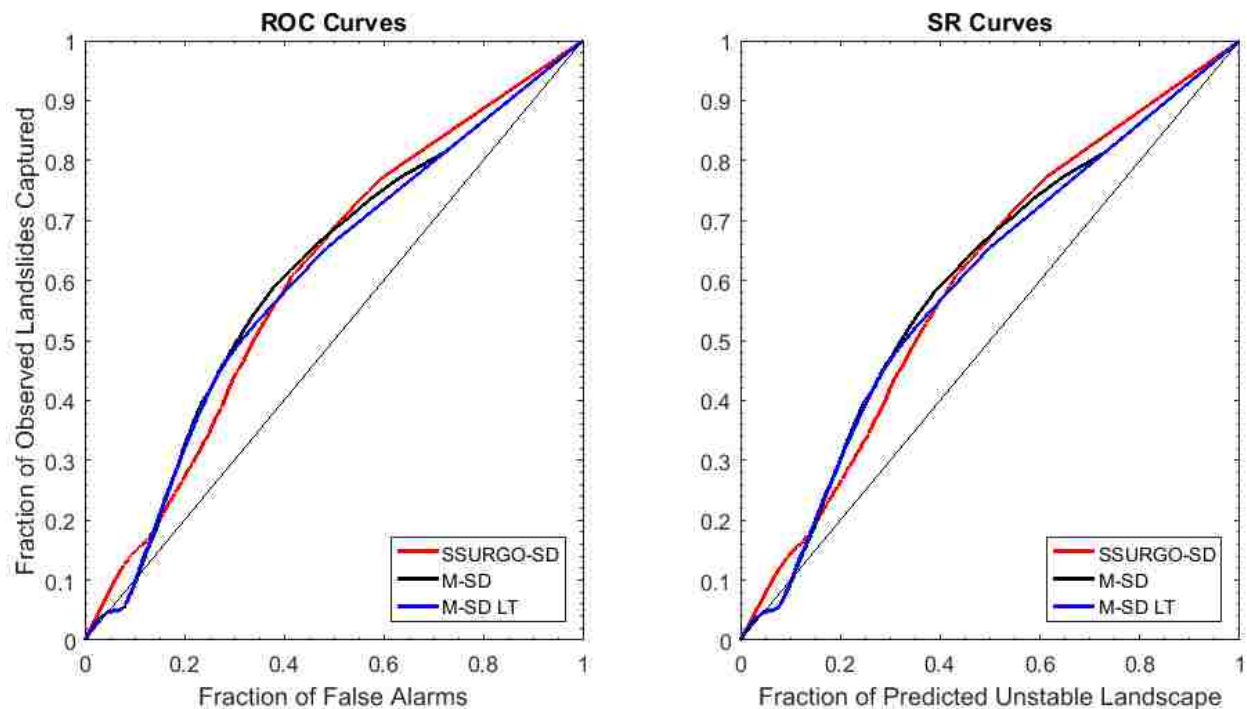


Figure 3.15. a) ROC curves and b) SR curves for simulations using SSURGO-SD, M-SD, and M-SD long-term (LT). Comparison represent $P(F)$ for the upper 10% of DA as observed landslides to a random sample of 5,000 cells outside DAs. Thresholds for simulated probabilities associated with positive classification of a source areas declines along the curves from lower left to upper right. Black diagonal line on a 1:1 line represents the case of a trivial or random classification model.

ROC and SR curves provide an indication of how well the modeled simulations of $P(F)$ classify both observed landslide source cells and non-landslide grid cells compared to random classification. The crossing of ROC and SR curves in the simulations with M-SD (Fig. 3.15) implies that at higher probability thresholds, simulated probabilities delineate more false alarms (e.g., areas outside DAs as unstable) than capturing source areas. This may be indicative of the high probability values at high elevations even outside the debris avalanches where vegetation is sparse, as was indicated above in the analysis of cumulative distribution plots. We found for our case study that the optimal probability threshold to maximizing landslides captured and minimizing false alarms (i.e., point around the apex of the ROC curves) declines by half depending on the simulation: $P(F) \geq 0.008$ (i.e., $RP \leq 125$ years) for SSURGO-SD, $P(F) \geq 0.004$ (i.e., $RP \leq 250$ years) for M-SD, and $P(F) \geq 0.002$ (i.e., $RP \leq 500$ years) for M-SD LT.

The modeled potentially unstable landscape has generally been greater than observed landslides when infinite slope stability models are calibrated with limited observations (Sidle and Ochiai, 2006; Baum et al., 2010). As pointed out by Borga et al. (2002), concluding “overrepresentation” of areas potentially subject to shallow landsliding can be misleading because the absence of mapped landslides does not necessarily indicate an absence of landslide hazard over time across the landscape. Locations with high landslide probability outside mapped landslides in both simulations could be indicators of where to conduct additional investigations for missed landslides or areas on the verge of failing.

Validating hazard maps is challenging, especially in large areas of remote mountainous regions, because inventories are typically incomplete, lack the date of landslide occurrence, different landslide types likely have different meteorological triggers, environmental conditions change after a landslide event, and unidentified high probability areas may fail in the near future even though they appear to be stable during an inventory (van Westen et al., 2006; Tarolli and Tarboton, 2006). Additional evaluation of model performance would benefit from field investigation in areas of high and low modeled P(F) to identify any landslides or instability that may have been missed during the original inventory. Future work that couples the volume of sediment available for landsliding will lead to further improvements in estimating hazards and potential impacts from landslides.

4.4.4 Model Limitations

For model design and computation efficiency, we made several simplifying assumptions. We neglect groundwater leakage to the bedrock in recharge estimation and apparent soil cohesion through the effect of surface tension in unsaturated zones, both of which could be added to future updates to the component. Tree and snow surcharge is also disregarded, although it may have some stabilizing effect where soils are shallower than 1 m (Hammond et al. 1992). Our approach does not simulate the actual number of landslides, landslide type, nor the size of the landslide because the discretized nature of the failure field precludes specific knowledge of which and how many grid units may be involved in a failure at a particular time. These model omissions present opportunities for future customization of the component or coupling with other models.

Modeled probability does not capture the runout of debris avalanches, which can travel considerable distances in steep mountainous environments. Some unexpected results depicted higher probability in runout portions of some debris avalanches when using SSURGO-SD, but these probabilities were lower when M-SD scenarios were used (e.g., Fig. 3.8, middle zoomed-in panels). Mis-mapping of probabilities of failure and observed landslide are likely attributed to variations in soil depth, material properties, and hydrologic routing (Schmidt et al., 2001). Model parameters such as slope derived from DEMs developed with post-landslide mapping can also contribute to reduced probabilities in observed landslides where slope and soil depth were reduced. Furthermore, inventories over broad areas are challenging as landslides are isolated processes that may occur with regularity, but may not be large in size (Van Westen et al., 2006). Finally, steady-state flow that we used for subsurface flow neglects transient processes and roles of macro-pores. Macropores from decayed roots or animal activity can be important in transporting water relatively quickly from the surface to deeper soil layers and groundwater (Sidle et al., 2001; Gabet et al., 2003; Beven and Germann 2013).

3.5 Conclusion

We develop a regional model of probabilistic shallow landslide initiation based on the infinite slope stability equation coupled by steady-state subsurface hydrology driven by groundwater recharge. Uncertainty in model parameters is explicitly accounted for through Monte Carlo simulation. A geomorphic soil evolution model provides a spatially-distributed soil depth alternative to homogeneous patches of soil depths provided by SSURGO. This feature allows the landslide model to be used where soil depth information is uncertain, sparse, or absent. Our model developed in Landlab (Hobley et al., 2017) is made up of a landsliding component, a Landlab utility for hydrologic data processing, and a model driver that runs the component. The

model driver can be run on personal computers or online via Hydroshare through cloud computing creating reproducible results. Our approach demonstrates:

- Regional maps of landslide hazard produced with three different soil depth scenarios reveal alternative simulations of probability of landslide initiation, reflecting the importance in soil depth in landslide hazard prediction.
- Simulations using SSURGO-SD returned higher probability of failures and shorter return periods than simulations using modeled soil depth products (M-SD and M-SD LT). The M-SD LT simulation further reduces the probability of failure and increases the return period. Mean annual denudation estimates from the M-SD LT scenario show closer estimates to published rates of denudation over the last millennia than the other simulations.
- SSURGO-SD scenario provide a short-term tool for high risk planning using conservative estimates of probability of failure, while M-SD LT provides long-term estimates more consistent with landslide frequency in the region and useful for management of ecosystems and aquatic habitats, and estimation of sediment budgets for watershed planning.
- Elevation dependent patterns in probability of landslide initiation show the stabilizing effects of forests in low elevations, an increased landslide probability with forest decline at mid elevations (1,400 to 2,400 m), and soil limitation and steep topographic controls at high alpine elevations and post-glacial landscapes. These dominant controls manifest in a bimodal distribution of spatial annual landslide probability, modes controlled by highly stable forested and chronically unstable post-glacial domains and other barren areas.
- Model testing with limited observations revealed similar model confidence for the three hazard maps, suggesting suitable use as relative hazard products. Validation of the model with observed landslides is hindered by the completeness and accuracy of the inventory, estimation of source areas, and unmapped landslides.
- Our shallow landslide hazard model provides regional scale estimates of the relative annual probability of shallow landslide initiation as well as landslide return period, which is useful for civil protection through land use planning to minimize geohazard consequences from precipitation triggers.

3.6 Data and Model Availability

To facilitate ease of use of the landslide hazard model, we developed the landslide model as a component of Landlab, an open-source Python toolkit for two-dimensional numerical modeling of Earth-surface dynamics available at GitHub: <http://github.com/landlab/landlab> (Hobley et al., 2017). Documentation, installation instructions, and software dependencies for the entire Landlab project can be found at: <http://landlab.github.io/>. The Landlab project is tested on recent-generation Mac, Linux and Windows platforms using Python versions 2.7, 3.4, and 3.5. The Landlab modeling framework is distributed under a MIT open-source license. A user manual and driver scripts for the application of the Landlab LandslideProbability can be found at: https://github.com/RondaStrauch/pub_strauch_etal_esurf (Strauch, GitHub Repository)

Online access to the Landlab LandslideProbability model is freely provided through <https://www.hydroshare.org>, where data and code drivers are available to demonstrate and

explore the model using interactive IPython notebooks in a JupyterHub. Thus, users can access, test, adapt, and apply the landslide model for their area of interest without downloading Landlab or the components. Data and driver code used in this analysis are available at hydroshare (Strauch et al., 2017). Existing demonstration driver codes can be adapted to fit data provided in raster format by the user to create distributed data fields used as parameters in the component. Instructions for accessing HydroShare and the online demonstrations, codes, and data used in this paper are provided in supplemental material.

Acknowledgements

This research was supported by the US National Science Foundation (CBET-1336725, OAC-1450412) and USGS Northwest Climate Science Center. We thank Dan Miller for helpful review of an earlier version of the manuscript. Technical editing on portions of the manuscript was provided by Brad Strauch and Diann Strom. We also appreciate the developers of Landlab, including open-source contributors to the earth surface processes modeling community. Data repository (Strauch et al., 2017), testing, and online reproducibility was facilitated by the cyber infrastructure of HydroShare services provided by researchers associated with the Consortium of Universities for the Advancement of Hydrologic Science, Inc. (CUAHSI), particularly the support of Tony Castronova, and the team at CyberGIS Center for Advanced Digital and Spatial Studies for their maintenance and support for our use of the ROGER Supercomputer at the National Center for Supercomputing Applications (NCSA) at University of Illinois at Urbana-Champaign.

References

- Adams, J.M., Gasparini, N.M., Hobbey, D.E.J. Tucker, G.E., Hutton, E.W.H., Nudurupati, S.S., and Istanbuluoglu, E.: The Landlab v1.0 OverlandFlow component: a Python tool for computing shallow-water flow across watersheds, *Geoscientific Model Development*, 10.4, 2017.
- Alvioli, M., Guzzetti, F., and Rossi, M.: Scaling properties of rainfall induced landslides predicted by a physically based model, *Geomorphology*, 213, 38-47, 2014.
- Anagnostopoulos, G.G., Fatichi, S., and Burlando, P.: An advanced process-based distributed model for the investigation of rainfall-induced landslides: The effect of process representation and boundary conditions, *Water Resources Research*, 51(9): 7501-7523, 2015.
- Barling, R.D., Moore, I.D., and Grayson, R.B.: A quasi-dynamic wetness index for characterizing the spatial distribution of zones of surface saturation and soil water content, *Water Resources Research*, 30.4: 1029-1044, 1994.
- Bathurst, J. C., Moretti, G., El-Hames, A., Moaven-Hashemi, A. and Burton, A.: Scenario modelling of basin-scale, shallow landslide sediment yield, Valsassina, Italian Southern Alps, *Natural Hazards and Earth System Science*, 5.2: 189-202, 2005.
- Baum, R.L., Galloway, D.L., and Harp, E.L.: Landslide and land subsidence hazards to pipelines, U.S. Geological Survey Open-File Report 2008-1164, 192 pp., 2008a.
- Baum, R., Savage, W., Godt, J.W.: TRIGRS — a fortran program for transient rainfall infiltration and grid-based regional slope-stability analysis, version 2.0, U.S. Geological Survey Open-File Report 2008-1159, 75 pp., 2008b.
- Baum, R.L, Godt J.W., and Savage, W.Z.: Estimating the timing and location of shallow rainfall-induced landslides using a model for transient, unsaturated infiltration. *Journal of Geophysical Research: Earth Surface*, 115(F3), 2010.
- Baum, R.L., Schulz, W.H., Brien, D.L., Burns, W.J., Reid, M.E., and Godt, J.W.: Plenary: Progress in

- Regional Landslide Hazard Assessment—Examples from the USA, In: *Landslide Science for a Safer Geoenvironment*, Springer International Publishing, 21-36, 2014.
- Bellugi, D., Milledge, D.G., Dietrich, W.E., Perron, J.T., and McKean, J.: Predicting shallow landslide size and location across a natural landscape: Application of a spectral clustering search algorithm. *Journal of Geophysical Research: Earth Surface*, 120(12), 2552-2585, 2015.
- Bellugi D., W.E. Dietrich, J. Stock, J. McKean, B. Kazian, and Hargrove, P.: Spatially explicit shallow landslide susceptibility mapping over large areas, *Italian Journal of Engineering Geology and Environment*, doi: 10.4408/IJEGE.2011-03.B-045, 2011.
- Benda, L. and Dunne, T.: Stochastic forcing of sediment supply to channel networks from landsliding and debris flow, *Water Resour. Res.* 33(12): 2849-2863, 1997a.
- Benda, L. and Dunne, T.: Stochastic forcing of sediment routing and storage in channel networks. *Water Resour. Res.* 33(12): 2865-2880, 1997b.
- Berti, M., Martina, M.L.V., Franceschini, S., Pignone, S., Simoni, A., and Pizziolo, M.: Probabilistic rainfall thresholds for landslide occurrence using Bayesian approach, *Journal of Geophysical Research* 117:F04006, 2012.
- Beven K.J. and Kirkby, N.J.: A physically based variable contributing area model of basin hydrology, *Hydrological Sciences Bulletin* 24: 43-69, 1979.
- Beven, K., and Germann, P.: Macropores and water flow in soils revisited. *Water Resour. Res.*, 49(6), 3071-3092, 2013.
- Bordoni, M., Meisina, C., Valentino, R., Bittelli, M., and Chersich, S.: Site-specific to local-scale shallow landslides triggering zones assessment using TRIGRS, *Natural Hazards & Earth System Sciences*, 15(5): 1025-1050, 2015.
- Borga, M., Fontana, G.D., and Cazorzi, F.: Analysis of topographic and climatic control on rainfall-triggered shallow landsliding using a quasi-dynamic wetness index. *Journal of Hydrology*, 268(1): 56-71, 2002.
- Borga M., Fontana, G.D., Ros, D.D., Marchi, L.: Shallow landslide hazard assessment using a physically based model and digital elevation data, *Environ Geol* 35(2-3):81-88, 1998.
- Braun, J., Heimsath, A.M., and Chappell, J.: Sediment transport mechanisms on soil-mantled hillslopes, *Geology*, 29(8): 683-686, 2001.
- Caine, N. The rainfall intensity: duration control of shallow landslides and debris flows. *Geografiska Annaler. Series A. Physical Geography*, 23-27, 1980.
- Carrara, A., M. Cardinali, F. Guzzetti, and Reichenback, P.: GIS technology in mapping landslide hazards. In: Carrara, A. and F. Guzzetti (eds.) *Geographical Information System in Assessing Natural Hazard*. Kluwer, New York, 107-134 pp., 1995.
- Casadei, M., Dietrich, W.E. and Miller, N.L.: Testing a model for predicting the timing and location of shallow landslide initiation in soil-mantled landscapes, *Earth Surf. Process. Landforms*, 28: 925-950, 2003.
- Castranova, T., Dockerfile for the HydroShare-JupyterHub base image, <https://hub.docker.com/r/castrona/hydroshare-jupyterhub/> (Accessed April 4, 2017), 2017.
- Catani F., Segoni, S., Falorni, G.: An empirical geomorphology-based approach to the spatial prediction of soil thickness at catchment scale, *Water Resour Res* 46, W05508, 2010.
- Chakravarti, I. M., Roy, J.D., and Laha, R.G.: *Handbook of Methods of Applied Statistics, Volume I*, John Wiley and Sons, pp. 392-394, 1967.
- Chen, W., Li, W., Hou, E., Zhao, Z., Deng, N., Bai, H., and Wang, D.: Landslide susceptibility mapping based on GIS and information value model for the Chencang District of Baoji, China, *Arabian Journal of Geosciences* 7(11): 4499-4511, 2014.
- Cho, S.E.: Effects of spatial variability of soil properties on slope stability, *Engineering Geology*, 92(3): 97-109, 2007.
- Chung, C.F., A.G. Fabbri, and Van Western. C.J.: Multivariate regression analysis for landslide hazard zonation. In: Carrara, A. and F. Guzzetti (eds.) *Geographical Information System in Assessing Natural Hazard*. Kluwer, New York: pp. 107-134, 1995.

- Crozier, M.J. Prediction of a rainfall-triggered landslide: A test of the antecedent water status model. *Earth Surf. Process. Landforms*, 24: 825-83, 1999.
- Crozier, M. J. *Landslides Causes, Consequences, and Environment*, Croom Helm, London, 252, pp.,1986.
- Cullen, A.C. and Frey, H.C. *Probabilistic techniques in exposure assessment: a handbook for dealing with variability and uncertainty in models and inputs*, Springer Science & Business Media, 1999.
- DiBiase, R.A., Whipple, K.X., Heimsath, A.M. and Ouimet, W.B.: Landscape form and millennial erosion rates in the San Gabriel Mountains, CA, *Earth and Planetary Science Letters*, 289, 134–44, 2010.
- Dietrich, W.E., R. Reiss, J. Hsu, and Montgomery, D.R.: A process-based model for colluvial soil depth and shallow landsliding using digital elevation data, *Hydrological Processes* 9: 383-400, 1995.
- Dou, H.Q., Han T.C., Gong, X.N., and Zhang, J.: Probabilistic slope stability analysis considering the variability of hydraulic conductivity under rainfall infiltration–redistribution conditions, *Engineering Geology*, 183:1-13, 2014.
- El-Ramly, H., Morgenstern, N.R., and Cruden, D.M.: Probabilistic slope stability analysis for practice, *Canadian Geotechnical Journal*, 39(3):665-683, 2002.
- Elsner, M.M., Cuo, L., Voisin, N., Deems, J.S., Hamlet, A.F., Vano, J.A., Mickelson, K.E.B., Lee S., and Lettenmaier, D.P.: Implications of 21st century climate change for the hydrology of Washington State, *Climatic Change*, 102 (1-2): 225-260, doi: 10.1007/s10584-010-9855-0, 2010.
- Fawcett, T.: An introduction to ROC analysis, *Pattern recognition letters*, 27(8):861-874, 2006.
- Formetta, G., Capparelli, G., and Versace, P.: Evaluating performance of simplified physically based models for shallow landslide susceptibility, *Hydrology and Earth System Sciences*, 20(11): 4585, 2016.
- Gabet, E.J., Reichman, O.J., and Seabloom, E.W.: The effects of bioturbation on soil processes and sediment transport, *Annual Review of Earth and Planetary Sciences*, 31(1):249-273, 2003.
- Gabet, E.J., and Dunne, T.: Landslides on coastal sage-scrub and grassland hillslopes in a severe El Nino winter: The effects of vegetation conversion on sediment delivery, *Geol. Soc. Am. Bull.*, 114(8):983–990, 2002.
- Glade, T.: Landslide hazard assessment and historical landslide data—an inseparable couple? In *The use of historical data in natural hazard assessments*, Springer Netherlands, 153-168 pp., 2001.
- Ghirotti, M.: The 1963 Vaiont landslide, Italy. In: J.J. Clague and D. Stead (eds.) *Landslides: Types, mechanisms and modeling*. Cambridge University Press, NY, 359 PP., 2012.
- Godt, J.W., Schulz, W.H., Baum, R.L., and Savage, W.Z.: Modeling rainfall conditions for shallow landsliding in Seattle, Washington, *Reviews in Engineering Geology*, 20: 137-152, 2008.
- Godt, J.W., and McKenna, J.P.: Numerical modeling of rainfall thresholds for shallow landsliding in the Seattle, Washington, area, *Reviews in Engineering Geology*, 20: 121-136, 2008.
- Goode, J.R., Luce, C.H., and Buffington, J.M.: Enhanced sediment delivery in a changing climate in semi-arid mountain basins: Implications for water resource management and aquatic habitat in the northern Rocky Mountains, *Geomorphology*, 139: 1-15, 2012.
- Gorsevski, P.V., Gessler, P.E., Boll, J., Elliot, W.J., and Foltz, R.B.: Spatially and temporally distributed modeling of landslide susceptibility, *Geomorphology*, 80.3: 178-198, 2006.
- Guthrie, R.H., and Brown, J.K.: Denudation and landslides in coastal mountain watersheds: 10,000 years of erosion, *Geographica Helvetica*, 63(1): 26-35, 2008.
- Guthrie, R.H., and Evans, S.G.: Analysis of landslide frequencies and characteristics in a natural system, coastal British Columbia, *Earth Surface Processes and Landforms*, 29(11): 1321-1339, 2004.
- Hales, T.C., Cole-Hawthorne, C., Lovell, L., and Evans, S.L.: Assessing the accuracy of simple field based root strength measurements, *Plant and soil*, 372(1-2): 553-565, 2013.
- Hamlet, A.F., M.M. Elsner, G. Mauger, S. Lee, and Tohver, I.: An Overview of the Columbia Basin Climate Change Scenarios Project: Approach, Methods, and Summary of Key Results, *Atmosphere-Oceans*, 51(4): 392-415, 2013.
- Hammond, C., Hall, D., Miller, S., and Swetik, P.: Level 1 stability analysis (LISA), documentation for Version 2.0. USDA, For. Serv., Moscow, ID, Intermountain Res. Sta. Gen. Tech. Rep. INT-285,

- 1992.
- Hanley, J.A., and McNeil, B.J.: The meaning and use of the area under a receiver operating characteristic (ROC) curve, *Radiology*, 143(1): 29-36, 1982.
- Haugerud, R.A., and Tabor, R.W.: Geologic map of the North Cascade Range, Washington, US Department of the Interior, US Geological Survey, 29 pp., 2009.
- Heimsath, A.M., Dietrich, W.E., Nishiizumi, K., and Finkel, R.C.: The soil production function and landscape equilibrium, *Nature*, 388(6640): 358-361, 1997.
- Hobley, D.E.J., Adams, J.M., Nudurupati, S.S., Hutton, E.W.H., Gasparini, N.M., Istanbuluoglu, E., and Tucker, G. E.: Creative computing with Landlab: an open-source toolkit for building, coupling, and exploring two-dimensional numerical models of Earth-surface dynamics, *Earth Surf. Dynam.*, 5(1): 21-46, doi:10.5194/esurf-5-21-2017, 2017.
- Horsburgh, J.S., Morsy, M.M., Castronova, A.M., Goodall, J.L., Gan, T., Yi, H., Stealey, M.J., and Tarboton, D. G.: HydroShare: Sharing Diverse Environmental Data Types and Models as Social Objects with Application to the Hydrology Domain, *JAWRA Journal of the American Water Resources Association*, 52(4): 873-889, <http://dx.doi.org/10.1111/1752-1688.12363>, 2016.
- Hren, M.T., Hilley, G.E., and Chamberlain, C.P.: The relationship between tectonic uplift and chemical weathering rates in the Washington Cascades: field measurements and model predictions, *American Journal of Science*, 307(9): 1041-1063, 2007.
- Idaszak, R., Tarboton, D.G., Yi, H., Christopherson, L., Stealey, M.J., Miles, B., Dash, P., Couch, A., Spealman, C., Ames, D.P., and Horsburgh, J.S.: HydroShare - A case study of the application of modern software engineering to a large distributed federally-funded scientific software development project, Chapter 10 in *Software Engineering for Science*, Edited by J. Carver, N. P. Chue Hong and G. K. Thiruvathukal, Taylor and Francis CRC Press, 219-236 pp., 2016.
- Islam, S.U., Déry, S.J., and Werner, A.T.: Future climate change impacts on snow and water resources of the Fraser River Basin, British Columbia. *Journal of Hydrometeorology*, 18: 473-496, doi: <http://dx.doi.org/10.1175/JHM-D-16-0012.1>, 2017.
- Istanbuluoglu, E.: Modeling catchment evolution: from decoding geomorphic processes signatures toward predicting impacts of climate change. *Geography Compass*, 3(3): 1125-1150, 2009.
- Istanbuluoglu, E., Tarboton, D.G., Pack R.T., and Luce, C.H.: Modeling of the interactions between forest vegetation, disturbances, and sediment yields. *Journal of Geophysical Research: Earth Surface*, 109(F1), 2004.
- Istanbuluoglu, E., and Bras, R.L.: Vegetation-modulated landscape evolution: Effects of vegetation on landscape processes, drainage density, and topography, *J. Geophys. Res.*, 110: F02012, doi:10.1029/2004JF000249, 2005.
- Iverson, R.M., Reid, M.E., and LaHusen, R.G.: Debris-flow mobilization from landslides, *Annual Review of Earth and Planetary Sciences*, 25(1): 85-1, 1997.
- Iverson, R. M.: Landslide triggering by rain infiltration, *Water resources research*, 36(7): 1897-1910, 2000.
- Jin, S, Yang L, Danielson P, Homer C, Fry J, and Xian, G.: A comprehensive change detection method for updating the National Land Cover Database to circa 2011, *Remote Sensing of Environment*, 132: 159-175, 2013.
- Kirschbaum, D.B., R. Adler, Y. Hong, S. Kumar, C. Peters-Lidard, and Lerner-Lam, A.: Advances in landslide nowcasting: evaluation of global and regional modeling approach. *Environ. Earth. Sci.* 66: 1683-1696, 2012.
- Liang X., Lettenmaier D.P., Wood, E.F., and Burges, S.J.: A simple hydrologically based model of land surface water and energy fluxes for GSMs, *J Geophys Res* 99(D7): 14,415–14,428, 1994.
- Livneh B., Rosenberg, E.A., Lin, C., Nijssen, B., Mishra, V., Andreadis, K.M., Maurer, E.P., and Lettenmaier, D.P.: A Long-Term Hydrologically Based Dataset of Land Surface Fluxes and States for the Conterminous United States: Update and Extensions, *Journal of Climate*, 26: 9384–9392, 2013.
- Livneh B., Bohn, T.J., Pierce, D.S., Munoz-Ariola, F., Nijssen, B., Vose, R., Cayan, D., and Brekke, L.D.: A spatially comprehensive, hydrometeorological data set for Mexico, the U.S., and southern

- Canada 1950-2013, *Nature Scientific Data*, 5:150042, doi:10.1038/sdata.2015.42, 2015.
- Lee S., Ryu, J-H., and Kim, I-S.: Landslide susceptibility analysis and its verification using likelihood ratio, logistic regression, and artificial neural network models: Case study of Youngin, Korea. *Landslides*, 4:327-338, 2007.
- Legg, N.T., Meigs, A.J., Grant, G.E., and Kennard, P.: Debris flow initiation in proglacial gullies on Mount Rainier, Washington, *Geomorphology*, 226, 249-260, 2014.
- Löffler, J.: The influence of micro-climate, snow cover, and soil moisture on ecosystem functioning in high mountains, *Journal of Geographical Sciences*, 17(1), 3-19, 2007.
- Lu, N., and Godt, J.W.: *Hillslope hydrology and stability*, Cambridge University Press, 2013.
- May, C.L., Pryor, B., Lisle, T.E., and Lang, M.: Coupling hydrodynamic modeling and empirical measures of bed mobility to predict the risk of scour and fill of salmon redds in a large regulated river, *Water Resources Research* 45, W05402, 2009.
- Miller D.J.: Coupling GIS with physical models to assess deep-seated landslide hazards, *Environ. Eng. Geosci.*, 1(3): 263-276, 1995.
- Mancini, F., Ceppi, C., and Ritrovato, G.: GIS and statistical analysis for landslide susceptibility mapping in the Daunia area, Italy, *Natural Hazards and Earth System Sciences*, 10(9): 1851, 2010.
- Mitchell, S.G., and Montgomery, D.R.: Influence of a glacial buzzsaw on the height and morphology of the Cascade Range in central Washington State, USA. *Quaternary Research*, 65(1): 96-107, 2006.
- Molnar, P.: Late Cenozoic increase in accumulation rates of terrestrial sediment: How might climate change have affected erosion rates?, *Annu. Rev. Earth Planet. Sci.*, 32, 67-89, 2004.
- Montgomery, D.R.: Slope distributions, threshold hillslopes, and steady-state topography. *American Journal of science*, 301(4-5), 432-454, 2001.
- Montgomery, D.R. and Dietrich, W.E.: A Physically Based Model for the Topographic Control on Shallow Landsliding, *Water Resources Research*, 30(4): 1153-1171, 1994.
- Montgomery, D.R., and Foufoula-Georgiou, E.: Channel network source representation using digital elevation models. *Water Resources Research*, 29(12): 3925-3934, 1993.
- Montrasio, L., and Valentino, R.: Modelling Rainfall-induced Shallow Landslides at Different Scales Using SLIP-Part I. *Procedia Engineering*, 158: 476-481, 2016.
- Moon, S., Chamberlain, C.P., Blisniuk, K., Levine, N., Rood, D.H., and Hilley, G.E.: Climatic control of denudation in the deglaciated landscape of the Washington Cascades, *Nature Geoscience*, 4(7): 469-473, 2011.
- Morsy, M.M., Goodall, J.L., Castronova, A.M., Dash, P., Merwade, V., Sadler, J.M., Rajib, M.A., Horsburgh, J.S., and Tarboton, D.G.: Design of a metadata framework for environmental models with an example hydrologic application in HydroShare, *Environmental Modelling & Software*, 93: 13-28, <http://dx.doi.org/10.1016/j.envsoft.2017.02.028>, 2017.
- Naudet, V., Lazzari, M., Perrone, A., Loperte, A., Piscitelli, S., and Lapenna, V.: Integrated geophysical and geomorphological approach to investigate the snowmelt-triggered landslide of Bosco Piccolo village (Basilicata, southern Italy), *Engineering Geology*, 98(3): 156-167, 2008.
- Nadim, F., Kjekstad, O., Peduzzi, P., Herold, C., and Jaedicke, C.: Global landslide and avalanche hotspots, *Landslides*, 3(2): 159-173, 2006.
- Nicótina, L., Tarboton, D. G., Tesfa, T. K., and Rinaldo, A.: Hydrologic controls on equilibrium soil depths, *Water Resources Research*, 47(4), 2011.
- Nimmo, J.R.: Unsaturated Zone Flow Processes, in Anderson, M.G., and Bear, J., eds., *Encyclopedia of Hydrological Sciences: Part 13--Groundwater*: Chichester, UK, Wiley, v. 4, p. 2299-2322, doi:10.1002/0470848944.hsa161, 2005.
- Okimura, T.: Prediction of slope failure using the estimated depth of the potential failure layer, *J. Natural Disaster Sci.*, 11(1):67-89, 1989.
- O'loughlin, E. M.: Prediction of surface saturation zones in natural catchments by topographic analysis. *Water Resources Research*, 22(5): 794-804, 1986.
- Pack, R.T., Tarboton, D.G., and Goodwin, C.: SINMAP 2.0-A Stability Index Approach to Terrain Stability Hazard Mapping, User's Manual. Available online:

- <http://www.engineering.usu.edu/dtarb/sinmap.html> [Accessed 30 Jan. 1916], 2005.
- Pack, R.T., D.G. Tarboton, and Goodwin, C.N.: Assessing Terrain Stability in a GIS using SINMAP, 15th Annual GIS Conference, Vancouver: <http://hydrology.usu.edu/sinmap/gis2001.pdf>, 2001.
- Pack R.T., Tarboton, D.G., and Goodwin, C.N.: The SINMAP approach to terrain stability mapping. In: Proceedings of the 8th international congress of the international association of engineering geology and the environment, Vancouver, British Columbia, Canada, September 21–25, vol 2. AA Balkema, Rotterdam, pp 1157–1165, 1998.
- Page, M.J., Trustrum, N.A., and DeRose, R.C.: A high-resolution record of storm-induced erosion from lake sediments, New Zealand, *Journal of Paleolimnology*, 11: 333-348, 1994.
- Pardeshi, S.D., Autade, S.E., and Pardeshi, S.S.: Landslide hazard assessment: recent trends and techniques, *SpringerPlus*, 2(1): 523, 2013.
- Pelletier, J.D., Barron-Gafford, G.A., Breshears, D.D., Brooks, P.D., Chorover, J., Durcik, M., Harman, C.J., Huxman, T.E., Lohse, K.A., Lybrand, R. and Meixner, T.: Coevolution of nonlinear trends in vegetation, soils, and topography with elevation and slope aspect: a case study in the sky islands of southern Arizona, *Journal of Geophysical Research-Earth Surface*, 118: 741–58, 2013.
- Pelletier, J.D., and Rasmussen, C.: Geomorphically based predictive mapping of soil thickness in upland watersheds, *Water Resources Research*, 45(9): W09417, doi:10.1029/2008WR007319, 2009.
- Pollok, M.M.: Biodiversity, In: R. J. Naiman and R. E. Bilby (eds.) *River Ecology and Management: Lessons from the Pacific Coastal Ecoregion*, Springer-Verlag, New York, 430–452 pp., 1998.
- PRISM Climate Group: Oregon State University, <http://prism.oregonstate.edu>, created 4 Feb 2004.
- Raia S, Alvioli M, Rossi M, Baum RL, Godt JW, and Guzzetti, F.: Improving predictive power of physically based rainfall-induced shallow landslide models: A probabilistic approach, *Geosci Model Dev Discuss*, 6:1367–1426, 2014.
- Regmi, N.R., Giardino, J.R., McDonald, E.V., and Vitek, J.D.: A comparison of logistic regression-based models of susceptibility to landslides in western Colorado, USA. *Landslides*, 11(2): 247-262, 2014.
- Reiners, P.W., Ehlers, T.A., Mitchell, S.G., and Montgomery, D.R.: Coupled spatial variations in precipitation and long-term erosion rates across the Washington Cascades, *Nature*, 426(6967), 645-647, 2003.
- Reiners, P.W., Ehlers, T.A., Garver, J.I., Mitchell, S.G., Montgomery, D.R., Vance, J.A., and Nicolescu, S.: Late Miocene exhumation and uplift of the Washington Cascade Range, *Geology*, 30(9): 767-770, 2002.
- Richards, L.A.: Capillary conduction of liquids in porous mediums, *Physics*, 1, 318–333, 1931.
- Riedel, J, Brady S, Dorsch S, and Wegner, J.: *Geomorphology of the Thunder Creek Watershed: Landform Mapping at North Cascades National Park Service Complex*, Washington. Natural Resource Technical Report NPS/NCCN/NRTR—2012/567. National Park Service, Fort Collins, Colorado, 2015.
- Riedel, J, and Prohala, J.: Mapping ecosystems at the landform scale in Washington state, *Park Science* 23-2: 37-42, 2005.
- Roe, G.H.: Orographic Precipitation. *Annu. Rev. Earth Planet. Sci.*, 33:645–71, 2005.
- Roering, J.J.: Soil creep and convex-upward velocity profiles: Theoretical and experimental investigation of disturbance-driven sediment transport on hillslopes, *Earth Surface Processes and Landforms*, 29(13): 1597-1612, 2004.
- Roering, J.J., Schmidt, K.M., Stock, J.D., Dietrich, W.E., and Montgomery, D.R.: Shallow landsliding, root reinforcement, and the spatial distribution of trees in the Oregon Coast Range, *Canadian Geotechnical Journal*, 40(2): 237-253, 2003.
- Roering, J.J., Kirchner, J.W., and Dietrich, W.E.: Evidence for nonlinear, diffusive sediment transport on hillslopes and implications for landscape morphology, *Water Resources Research*, 35(3): 853-870, 1999.
- Schmidt, K.M., Roering, J.J., Stock, J.D., Dietrich, W.E., Montgomery, D.R., and Schaub, T.: The variability of root cohesion as an influence on shallow landslide susceptibility in the Oregon Coast Range, *Canadian Geotechnical Journal*, 38(5), 995-1024, 2001.

- Selby, M.J.: Hillslope Materials and Processes. 2nd edit., Oxford University Press, 1993.
- Sidle, R.C.: A conceptual model of changes in root cohesion in response to vegetation management, *Journal of Environmental Quality*, 20(1): 43-52, 1991.
- Sidle, R.C.: A theoretical model of the effects of timber harvesting on slope stability, *Water Resources Research*, 28(7): 1897-1910, 1992.
- Sidle, R.C., Noguchi, S., Tsuboyama, Y., and Laursen, K.: A conceptual model of preferential flow systems in forested hillslopes: Evidence of self-organization, *Hydrological Processes*, 15(10): 1675-1692, 2001.
- Sidle, R.C., and Ochiai, H.: Landslides: processes, prediction, and land use, *Water Resources Monogram* 18, American Geophysical Union, Washington DC, 2006.
- Smith, K.: Mass movement hazards (Ch. 8), In: *Environmental hazards: Assessing risk and reducing disasters* (6th edition). Routledge, New York, NY., 205-234 pp., 2013.
- Strenk, P.M.: Evaluation of analytical procedures for estimating seismically induced permanent deformations in slopes, *Doctoral Thesis*, Drexel University, 2010.
- Stock, J., and Dietrich, W.E.: Valley incision by debris flows: Evidence of a topographic signature, *Water Resources Research* 39.4, 2003.
- Strauch, R., E. Istanbuluoglu, S. S. Nudurupati, C. Bandaragoda (2017). Regional landslide hazard using Landlab - NOCA Data, HydroShare, <http://www.hydroshare.org/resource/a5b52c0e1493401a815f4e77b09d352b>
- Sweeney, K.E., Roering, J.J., and Ellis, C.: Experimental evidence for hillslope control of landscape scale. *Science*, 349(6243), 51-53, 2015.
- Tarboton, D.G., Idaszak, R., Horsburgh, J.S., Heard, J., Ames, D., Goodall, J.L., Band, L., Merwade, V., Couch, A., Arrigo, J., Hooper, R., Valentine, D., and Maidment, D.: HydroShare: Advancing Collaboration through Hydrologic Data and Model Sharing, in D. P. Ames, N. W. T. Quinn and A. E. Rizzoli (eds), *Proceedings of the 7th International Congress on Environmental Modelling and Software*, San Diego, California, USA, International Environmental Modelling and Software Society (iEMSS), ISBN: 978-88-9035-744-2, 2014. http://www.iemss.org/sites/iemss2014/papers/iemss2014_submission_243.pdf, 2014.
- Tarolli, P., Borga, M., and Dalla Fontana, G.: Analysing the influence of upslope bedrock outcrops on shallow landsliding, *Geomorphology*, 93(3): 186-200, 2008.
- Tarolli, P., and Dalla Fontana, G.: Hillslope-to-valley transition morphology: new opportunities from high resolution DTMs, *Geomorphology*, 113(1), 47-56, 2009.
- Tarolli, P. and Tarboton, D.G.: A new method for determination of most likely landslide initiation points and the evaluation of digital terrain model scale in terrain stability mapping, *Hydrol. Earth Syst. Sci.* 10: 663-677, 2006.
- Taylor, F., and Brabb, E.E.: Map showing the status of landslide inventory and susceptibility mapping in California (No. 86-100). US Geological Survey, 1986.
- Tesfa, T.K., Tarboton, D.G., Chandler, D.G., and McNamara, J.P.: Modeling soil depth from topographic and land cover attributes. *Water Resources Research*, 45(10), 2009.
- Tobutt D.C.: Monte Carlo simulation methods for slope stability. *Comput. Geosci.*, 8(2): 199-208, 1982.
- Tucker, G.E., Hobbey, D.E., Hutton, E.W.H., Gasparini, N.M., Istanbuluoglu, E., Adams, J.M., and Nudurupati, S.S.: CellLab-CTS 2015: a Python library for continuous-time stochastic cellular automaton modeling using Landlab., *Geoscientific Model Development*, 8: 9507-9552, doi:10.5194/gmd-9-823-2016, 2016.
- Tucker, G.E., and Bras, R.L.: Hillslope processes, drainage density, and landscape morphology. *Water Resources Research*, 34(10), 2751-2764, 1998.
- Tucker, G.E., and Slingerland, R.: Drainage basin responses to climate change. *Water Resources Research*, 33(8), 2031-2047, 1997.
- United States Department of the Interior, National Park Service (DOI-NPS): Foundation Document, North Cascades National Park Complex, Washington. Available from: <https://www.nps.gov/noca/learn/management/upload/North-Cascades-NP-Complex-Foundation->

- Document_small.pdf (Accessed 23 January 2017), 2012.
- U.S. Department of Agriculture, Natural Resources Conservation Service (DOA-NRCS), and United States Department of the Interior, National Park Service (DOI-NPS).: Soil survey of North Cascades National Park Complex, Washington, 2012.
- United States Department of Agriculture, Natural Resources Conservation Service (DOA-NRCS).: United States Department of Agriculture. Web Soil Survey. Available from: <http://websoilsurvey.nrcs.usda.gov/>. (Accessed 23 January 2017), 2016.
- DOA-NRCS.: Soil Data Viewer software. Available from: www.nrcs.usda.gov/wps/portal/nrcs/detailfull/soils/home/?cid=nrcs142p2_053620 [Accessed 23 June 2015], 2015a.
- DOA-NRCS.: Soil Texture Calculator software. Available from: www.nrcs.usda.gov/wps/portal/nrcs/detail/soils/survey/?cid=nrcs142p2_054167 [Accessed 24 June 2015], 2015b.
- United States Geological Survey (USGS).: Shuttle Radar Topography Mission (STRM) 1 arc-second global, Joint NASA-NGA partnership, data distributed and archived by USGS EROS Data Center, Available online at <https://lta.cr.usgs.gov/SRTM1Arc>. (Accessed 26 April 2017), 2017.
- USGS.: National Elevation Data last modified March 6, 2014, National Map Viewer (Accessed 24 November 2014), 2014a.
- USGS.: National Land Cover Data (NLCD) version Marched 31, 2014, National Map Viewer (Accessed 25 November 2014), 2014b.
- Van Westen, C.J., Van Asch, T.W., and Soeters, R.: Landslide hazard and risk zonation—why is it still so difficult? *Bulletin of Engineering geology and the Environment*, 65(2), 167-184, 2006.
- Van Beek, L.P.H.: Assessment of the influence of changes in land use and climate on landslide activity in a Mediterranean environment (Doctoral dissertation), Nederlandse Geografische Studies, Universiteit Utrecht. pp 294, 2002.
- Yin, D., Liu, Y.Y., Padmanabhan, A., Terstriep, J., Rush, J., and Wang, S.: A CyberGIS-Jupyter Framework for Geospatial Analytics at Scale. The First Practice & Experience in Advanced Research Computing (PEARC) Conference, Under review, 2017.
- Wayand, N., Stimberis, J., Zagrodnik, J., Mass, C.F. and Lundquist, J.D.: Improving Simulations of Precipitation Phase and Snowpack at a Site Subject to Cold Air Intrusions: Snoqualmie Pass, WA, *J. of Geophysical Research, Atmospheres*, 121, doi: 10.1002/2016JD025387, 2016.
- Wartman, J., Montgomery, D.R., Anderson, S.A., Keaton, J.R., Benoît, J., dela Chapelle, J., and Gilbert, R.: The 22 March 2014 Oso landslide, Washington, USA. *Geomorphology*, 253: 275-288, 2016.
- Wu, W. and Sidle, R.C.: A Distributed Slope Stability Model for Steep Forested Watersheds, *Water Resour. Res.*, 31(8): 2097– 2110, 1995.
- Zizioli, D., Meisina, C., Valentino, R., and Montrasio, L.: Comparison between different approaches to modeling shallow landslide susceptibility: a case history in Oltrepo Pavese, Northern Italy, *Natural Hazards and Earth System Sciences* 13(3): 559, 2013.

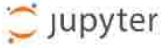
Supplemental Material

Accessing Landlab landslide component through HydroShare

Access to a reproducible application of the Landlab LandslideProbability component for the North Cascades National Park Complex (NOCA) using a Jupyter Notebook via Hydroshare is provided through the following steps. The HydroShare resource contains or accesses the data, application driver code, and Landlab LandslideProbability component, all that is needed to reproduce the probability of failure discussed in this paper.

1. Go to <https://www.hydroshare.org> and click on 'Sign up now' blue Button

2. Create an account if you don't have one. After filling out "Sign Up" profile information (can edit at a later date), verify and activate account from your email (sent by HydroShare).
3. At <https://www.hydroshare.org>, sign In with you user name (email) and password.
4. Click on 'Discover' tab in the menu at top.
5. In Search window, type: "Regional landslide hazard using Landlab - NOCA Observatory". Select this resource. Read the *Abstract* about this resource and scan sections below.
6. Scroll down to see the 'Content' and the data used in the landslide component and the Jupyter Notebook that accesses the notebook "NOCA_runPaper_LandlabLandslide.ipynb" that will 'drive' the landslide model.
7. To run this reproducible application within HydroShare, once you've navigated to the "Regional landslide hazard using Landlab - NOCA Observatory", click on the 'Open with...' blue button and select "JupyterHub NCSA".
8. A "Welcome to the HydroShare Python Notebook Server" will open in a new window. This notebook steps through the model preparation, allowing you to execute the Landlab LandslideProbability component. Review the descriptions for this welcome notebook and scroll down to the first code box. To access HydroShare resources, execute the first shaded code box with **In []**: in front and then typing "shift-enter" (both keys at the same time). A * will appear in the [] when this code box is running and a number will appear in the [1] when it is finished.
9. You will likely need to enter your HydroShare Password again in the box provided. This should end with a green text saying "Successfully established a connection with HydroShare".
10. Also execute the next code box to see where the data to run the reproducible application is located, given by a long resource id.
11. "Get Resource Content" is the next code box. This accesses the "landslide_driver.ipynb" NOCA application. If you've run this application before, it will ask if you want to overwrite your previous work, type 'y' ('n') for yes (no). this will end with the statement:

```
'Successfully downloaded resource 07a4ed3b9a984a2fa98901dcb6751954'
```
12. A list of the content of this Observatory is provided as well as the notebook we need. Click on the "NOCA_runPaper_LandlabLandslid.ipynb" notebook in blue text.
13. Now you are inside the landslide application. Read the introduction and begin executing the code boxes one-by-one using "shift-enter". Also read the before and after text boxes to understand what you're executing. Some might take a few seconds or even minutes to run given the size of the datasets. If an error occurs, try restarting the kernel by clicking "Kernel" on the menu above and select "Restart".
14. You can also try some of you own code by selecting the + in the menu bar at top, which adds a new code cell where you can execute python code.
15. You can save the execution of this notebook back to HydroShare as your own resource at the end of the notebook. View and download these files by clicking on the  jupyter icon in the upper left corner. View the notebooks folder and explore the subfolders, including the data folder.
16. To end your Jupyter server session, either select 'File', 'close and halt' within the notebook, or select the 'Running' tab, 'Shutdown' button within the Jupyter server.

The Landlab LandslideProbability Component

User Manual

Ronda Strauch, Erkan Istanbuluoglu, Sai Siddhartha Nudurupati
June 2017

1. Background on LandslideProbability Component

The Landlab LandslideProbability component implements the infinite slope stability model using a Monte Carlo simulation to predict the probability of shallow landslide initiation based on local slope, specific catchment area, climatological triggers, and soil and vegetation parameters on Landlab's RasterModelGrid. A for loop inside the component executes the Monte Carlo simulation at each node of the RasterModelGrid. The LandslideProbability component is executed by a user-written driver script that parametrizes, instantiates, runs, and plots data and results. This User Manual describes the LandslideProbability component and how to parameterize, instantiate, run, and plot data and results described in Strauch et. al., (*in review*) and using "Regional landslide hazard using Landlab - NOCA Observatory" containing two example model drivers available on <https://www.hydroshare.org/>. This document is a supplement to the manuscript in *Earth Surface Dynamics*.

The component is based on Mohr-Coulomb failure law using the infinite slope stability model that predicts the ratio of stabilizing forces due to friction and cohesion, mediated by pore-water pressure to destabilizing forces due to gravity, implemented on a failure plane parallel to the land surface, coupled with a topography-driven steady-state subsurface flow model (Montgomery and Dietrich 1994; Pack et al. 1998). The component executes a Monte Carlo solution of the coupled model by generating model forcing and parameters: daily recharge to subsurface flow that reflects local pore-water pressure through regulating the water table, soil internal friction angle, combined root and soil cohesion, soil transmissivity, and soil depth from assumed probability density functions. Local slope and specific catchment area are generated from a digital elevation model (DEM). Several options are offered for recharge. This component expands the capabilities of Landlab by providing a probabilistic shallow landsliding model that can also be used to develop watershed sediment yield models.

Note: Currently, the LandslideProbability component can only operate on a structured grid; therefore, all the references to the grid below are referring to the Landlab RasterModelGrid object.

Prerequisites: A working knowledge of the Python programming language (any version) and familiarity with the Python libraries NumPy and Matplotlib are beneficial. Also, a basic understanding of the Landlab modeling framework (Hobley et al., 2017) and the RasterModelGrid module is recommended.

2. Model Description

2.1. Model Parameters (inputs)

Spatial model parameters listed here are primarily pre-processed by the model user in a geographic information system, such as Esri's ArcGIS rasters converted to ASCII format. Users may acquire and generate these parameters from a variety of sources. Details on where to find readily available data and how to process these data into parameter rasters are provided in Strauch et al., (*in review*). For example, root cohesion can be generated from reclassifying land use/land cover (LULC) rasters from USGS National Land Cover Data (USGS 2014; Jin 2013) based on reference to a lookup table that specifies the root cohesion for different LULC types, Table 1 in Strauch et al., (*in review*). The reclassified raster can then be converted to an ASCII file for import into Landlab, defined with number of rows and columns and cell size.

Parameters are assigned as *fields* to nodes in the RasterModelGrid. Most Landlab names follow the naming conventions of Community of Surface Dynamics Modeling System (CSDMS) (Peckham, 2014). Fields are accessed using Python's dictionary data structure where the field name, such as '*topographic__slope*' is a string keyword assigned and used to access the values array. Methods to import these parameters into Landlab are detailed below in section 3.3 Step 3.

- **topographic__slope:** [-] – local elevation gradient slope of surfaces as represented by the tangent of hillslope slope angle.
- **topographic__specific_contributing_area:** [m] – specific contributing area calculated as upslope drainage area/unit contour length (e.g., grid cell width) using the multiple flow direction D-infinity approach of TauDEM.
(<http://hydrology.usu.edu/taudem/taudem5/index.html>)
- **soil__internal_friction_angle:** [deg] Critical angle just before failure due to friction between particles.
- **soil__maximum_total_cohesion:** [Pa] Maximum of combined root and soil cohesion.
- **soil__minimum_total_cohesion:** [Pa] Minimum of combined root and soil cohesion.
- **soil__mode_total_cohesion:** [Pa] Mode of combined root and soil cohesion.
- **soil__thickness:** [m] Depth to restrictive layer (e.g., bedrock, low permeable layer).
- **soil__transmissivity:** [m²/day] depth integrated saturated hydraulic conductivity; required input if conductivity is NOT provided.
- **soil__hydraulic_conductivity:** [m/day] rate of water transmitted through soil; required input if transmissivity is NOT provided to calculate transmissivity with soil depth
- **soil__density:** [kg/m³] Wet bulk density of soil, which is set uniformly across model domain at 2000 kg/m³ in the current application, but can be spatially distributed by user as a field on the RasterModelGrid.

The hydrologic driver of shallow landslide initiation in this model is a daily annual maximum rate of recharge [mm/d]. Given that users may acquire or identify recharge from various resources or approaches, the LandslideProbability component provides four options to parameterize recharge. These options control the amount of data used within the model and the distribution of the data, which is designed to represent uncertainty in recharge rate. The options are identified through a 'distribution' specified by the user as listed below. The distribution and parameters are passed from the drive to the component. Additional details on setting up the recharge are provided in Determine groundwater recharge inputs in section 3.5.

- **groundwater__recharge_distribution**: [mm/d] distribution to use for representing recharge specified as one of four options:
 - **'uniform'** – user specifies parameters **groundwater__recharge_min_value** and **groundwater__recharge_max_value** used to generate uniformly distributed recharge applied uniformly over the RasterModelGrid.
 - **'lognormal'** – user specifies parameters **groundwater__recharge_mean** and **groundwater__recharge_standard_deviation** used to generate lognormally distributed recharge applied uniformly over the RasterModelGrid.
 - **'lognormal_spatial'** – user specifies parameter arrays for **groundwater__recharge_mean** and **groundwater__recharge_standard_deviation** for each node of the RasterModelGrid used to generate spatially variable lognormally distributed recharge. We recommend providing parameters from routed recharge to better represent the spatial hydrology as arrays of: **groundwater__recharge_mean** and **groundwater__recharge_standard_deviation**.
 - **'data_driven_spatial'** – user specifies three dictionaries for **groundwater__recharge_HSD_inputs** in a list using the format of [HSD_dict, HSD_id_dict, fract_dict] (*in that order*). HSD is the *'Hydrology Source Domain'* that provides the recharge from a hydrologic model, which is processed to generate routed recharge at each RasterModelGrid node using a nonparametric method.

2.2. Model Variables (outputs)

Variables listed below are calculated by the component at RasterModelGrid locations in the model domain.

- **soil__mean_relative_wetness**: [-] mean of the ratio of depth of subsurface flow over a restrictive layer to the depth of soil layer over the restrictive layer. The value has a range from 0 (dry soil) to 1 (saturated soil).
- **soil__probability_of_saturation**: [-] ratio number of times relative wetness is ≥ 1 out of number of iterations user selected
- **landslide__probability_of_failure**: [-] ratio of the number of failures simulated (i.e., $FS \leq 1$) divided by the number of iterations in the Monte Carlo simulation, which calculates deterministic FS values.

3. Basic Steps of a Landslide Model

Here we first list the basic steps to develop a Landlab Landslide hazard model, followed by their detailed explanations.

1. **Import necessary libraries**: Only LandslideProbability from landlab.io is required. However, optional libraries that may be useful include: numpy, read_esri_ascii, write_esri_ascii, matplotlib, cPickle, os, collections, and pandas, depending on the data processing and outputs desired by the user. The SourceTracking_UTILITY is also helpful for routing.
2. **Define model domain**: The model computational domain of the LandslideProbability component can only work on a RasterModelGrid instances as of Landlab version 1.0.0.
3. **Load model input data and parameters**: Several data and parameter fields are required to run the LandslideProbability component. These input parameters, described above, can be typically read in using `read_esri_ascii()` if they are prepared in ESRI's ArcGIS software, or can consist of arrays of the same length of the number of nodes, and assigned to the RasterModelGrid.

4. **Set boundary conditions:** Often only a portion of the model domain is desired for analysis, such as watershed boundaries, jurisdictional boundaries, or areas above a certain topographic criterion such as elevation. Additionally, input parameters often have missing data that are excluded from analysis. These regions can be defined by setting `set_nodata_nodes_to_closed()` (Hobley et al. 2017). <http://landlab.readthedocs.io/en/latest/landlab.grid.base.html#boundary-condition-control> .

5. **Set Monte Carlo iterations value:** The user set the number of iterations they wish for the Monte Carlo simulation.

6. **Determine groundwater recharge inputs:** Flexibility is provided for the user to define the groundwater recharge used to calculate relative soil wetness. The user must determine the recharge values and or parameters as well as the desired parametric probability distributions they wish to use for data generation.

7. **Initialize LandslideProbability component:** The instance of the LandslideProbability class is declared and parameters are set by the user.

3.1. Step 1. Import necessary libraries

To build a landslide model using the Landlab LandslideProbability component, first the necessary Landlab components and utilities, as well as any necessary Python packages and customized utilities must be imported. Standard Python style dictates all import statements belong in the top of the driver file or script, after the module docstrings. An example of a landslide model driver begins as follows:

```

#####
'''
Landslide_driver.py

Purpose: To model shallow landslide initiation probability by gathering
input data, running LandslideProbability component, and visualizing/storing
data and outputs.

Inputs: Data is provided by the user and consists of elevation
from a DEM and derived topographic traits such as slope and contributing area.
User also supplies soil characteristics derived from a soil survey,
land cover, or other sources, including transmissivity, cohesion,
internal angle of friction, soil density, and soil thickness.
Groundwater recharge is derived from post-processed hydrological data
provided from the VIC hydrological model at 1/16 degree resolution.

Outputs: mean relative wetness, probability of saturation, and
probability of failure based on Monte Carlo simulation.

Authors: R.Strauch, E.Istanbulluoglu, and S.Nudurupati
University of Washington
Created on Thu Aug 20, 2015
Last edit June 9, 2017
'''
#####
# %% Import libraries and utilities
## Landlab components
from landlab.components.landslides import LandslideProbability

## Landlab utilities
from landlab.io import read_esri_ascii # OR from landlab import RasterModelGrid
from landlab.io import write_esri_ascii
from landlab.plot.imshow import imshow_node_grid #plotter function optional

## Additional Python packages or customized utilities
import numpy as np
import os
import matplotlib.pyplot as plt
import matplotlib as mpl
import cPickle as pickle
import pandas as pd
#####

```

To run the model for the application here, only the `LandslideProbability` component is needed. This will calculate relative wetness and probability of failure across the model domain, which is at a 30-m resolution in this application. The domain will be defined by the DEM (see Step 2). Other Landlab utilities used in this example are the plotting library `imshow_node_grid`, which is a utility that can plot a Landlab grid instance and data field in map view (see Section 4). Finally, additional Python packages and user defined utilities are imported. In this application, the `numpy` and `matplotlib` are dependencies of Landlab, meaning they are installed as part of the Landlab installation and thus, are likely already available with the user's Python distribution. The scientific computing library `numpy` is used for mathematical operations, and the `matplotlib` library is for plotting model output. The `os` library is useful for handling files and folders when processing data, such as hydrologic flux files in the HSD. The `cPickle` library helps handle dictionaries that provide lookup tables of identifiers and data used in the `SourceTracking_Utility` and `data_driven_spatial` recharge option. `Pandas` Python package provides fast, flexible, and expansive data structures particularly useful for process data associated with dates such as flux files.

3.2. Step 2. Define the model domain

As mentioned above, the `LandslideProbability` component was designed to work on a gridded landscape by using the `RasterModelGrid` instance in Landlab. The `RasterModelGrid` is square

and composed of nodes, which are points in (x,y) space in the implementation of the LandslideProbability component. The grid nodes consist of rows and columns numbered from 0 at the lower left corner of the grid and ending at the upper right corner of the grid, looping left to right in number as one moves up the rows from the bottom. Calculations in the LandslideProbability component are made at each grid cell as represented by the central node. There are two methods to implement a RasterModelGrid in Landlab. A grid can be created by reading in data from an ASCII file created in Esri ArcGIS or using the RasterModelGrid class directly. An example using a DEM to establish a grid instance follows the syntax:

```
(grid, z) = read_esri_ascii('elevation.txt', name='topographic_elevation')
```

The second approach can be accomplished with the following code:

```
grid = RasterModelGrid((number_of_node_rows, number_of_node_columns),  $\Delta x$ )
```

The first method demonstrated below is reading a DEM with *read_esri_ascii()*.

```
# Load in DEM from ArcGIS
(grid, z) = read_esri_ascii(data_folder+'/elevation.txt',
                           name='topographic_elevation')
grid.at_node.keys()      # loads DEM grid with elevation
```

In this application, the 'elevation.txt' represents a square domain of 3217 rows and 2185 columns that includes the North Cascades National Park Complex in Washington, U.S.A. The path to the file was previously defined in 'data_folder' variable and is dependent on the user's file system. The second command assigns the elevation data to nodes. This particular DEM was pit-filled using TauDEM. The component does not use elevation in the calculations; however, loading it established the full model domain and can be helpful in visualizations.

The second method to establish an elevation grid sets the RasterModelGrid instance manually:

```
grid = RasterModelGrid((number_of_node_rows, number_of_node_columns), dx)
z = user_defined_elevation_data # array length of rows*columns
grid.at_nodes['topographic_elevation'] = z
```

This application assumes that model user knows and defines the number of grid rows, number of grid columns, the grid resolution (dx) and elevation data at each node. The *user_defined_elevation_data* must be the same length as the number of nodes in the RasterModelGrid, which can be found by using the command: *grid.number_of_nodes()* after the first line. The first row must match the lower left position and end with the upper right position of the RasterModelGrid.

3.3. Step 3. Load model input data and parameters

Ten model inputs, including topographic attributes and hydrologic forcing variables as well as soils and vegetation related parameters, are required by the LandslideProbability component. Nine of these are assigned to the RasterModelGrid and thus, provide the ability to spatially vary the parameters across the model domain. These are typically pre-processed in ArcGIS and read in similar to the DEM using *read_esri_ascii('parameter')* using the example code block below for slope. Note that in the development of specific catchment area, a larger domain is used to capture the regional boundary of the watersheds that contribute flows into the boundaries of the study area if it does not follow watershed boundaries.

```
# load slope from esri ascii file
(grid1, slope) = read_esri_ascii(data_folder+'/slope_tan.txt')
grid.add_field('node', 'topographic__slope', slope)
```

If the user has an array of values, they can assign the values to the RasterModelGrid similar to the alternative method described above for establishing an elevation field. The user may also want to set a parameter uniformly across the model domain, such as soil density using the syntax below.

```
# set soil density value and assign to all nodes
grid['node']['soil__density'] = 2000*np.ones(grid.number_of_nodes)
```

This approach can also be used to set **soil__minimum_total_cohesion** and **soil__maximum_total_cohesion** if only a **soil__mode_total_cohesion** is provided and the users wished to set the minimum and maximum as a fraction of the mode.

3.4. Step 4. Set boundary conditions

Often there are gaps in data or areas of a model domain that a user wished to exclude from analysis. These areas are handled through the establishment of boundary conditions on the grid nodes. Node boundary status can be set to *boundary* or *core*; boundary nodes can be further defined as *open* or *closed*. Grid perimeter nodes are open and interior nodes are core nodes by default. Interior nodes can be set to closed boundary conditions by the user for nodes that have no data, commonly represented by value -9999. The core nodes are the nodes where the component operates and calculates probability of failure. Landlab has several methods to set and update boundary conditions at *node* elements. Data imported for model parameters in Step 3 often have missing values usually defined as -9999. These can be set to closed nodes using the following command:

```
# set boundary conditions closed where no data
grid.set_nodata_nodes_to_closed(grid.at_node['soil__transmissivity'], -9999)
```

This is also an approach for using a *mask* set up in ArcGIS where locations to include in the analysis have node values set to 1 and areas to exclude set to -9999. To test a subarea before analyzing an entire modeling domain, the mask can be set up for a subarea and then commented out to run the model for the entire domain. Another way to test an area is to establish a subset of *core_nodes* and run the component only for this subset.

3.5. Step 5. Set Monte Carlo iterations value

The number of Monte Carlo iterations, n , is a parameter defined by the user. The simulated failure probability becomes more stable (i.e., consistent) with increasing n at the expense of computer time (Cho 2007; El-Ramly et al. 2002). Hammond et al. (1992) recommends at least 1,000 iterations for the Monte Carlo simulation. This is set by the user using the following syntax:

```
# number_of_iterations for Monte Carlo simulation
number_of_iterations = 3000
```

3.6. Step 6. Determine groundwater recharge inputs

Groundwater recharge is the hydrologic driving force that increases pore-water pressure within the soil layer, reducing the effective normal stress. The LandslideProbability component

provides several options for the user to provide recharge input. Within the driver, the user provides information on recharge, which is used to instantiate the component. This information includes a *distribution* and the *parameters* (Table 1). The distribution can be: ‘uniform’, ‘lognormal’, ‘lognormal_spatial’, or ‘data_driven_spatial’. The parameters represent scalars, arrays, or lists, depending on the distribution specified. Options are shown in Table 1 and detailed descriptions with code snippets for each distribution type follow the table.

Table 1 – Recharge inputs accepted by LandslideProbability component

Distribution	Parameters	Input / Comments
‘uniform’	<ul style="list-style-type: none"> ● minimum ● maximum 	Minimum and maximum recharge is provided to generate a uniform sampling distribution over the model domain
‘lognormal’	<ul style="list-style-type: none"> ● mean ● standard deviation 	Mean and standard deviation of recharge is provided to calculate mu and sigma for generating a lognormal sampling distribution applied uniformly over the model domain.
‘lognormal_spatial’	<ul style="list-style-type: none"> ● [mean] ● [standard deviation] 	Mean and standard deviation arrays are provided for each node and used to calculate mu and sigma for a lognormal sampling distribution for each node such that recharge is spatially distributed. Each of these arrays needs to be the same length as RasterModelGrid nodes. Only core node values will be used in calculations.
‘data_driven_spatial’	<ul style="list-style-type: none"> ● {HSD_Re} ● {HSD_ID} ● {fractions} 	HSD_Re dictionary is a unique array of recharge provided as arrays (‘values’) for each of the Hydrologic Source Domain (HSD) (‘keys’). HSD_ID dictionary has the model domain node ID as ‘keys’ and HSD IDs in a list as ‘values’. The fractions dictionary assigns to each node ID as ‘key’ a lists the fractions of each HSD draining to the node as ‘values’.

● **Recharge: ‘uniform’**

In this option, the user specifies distribution as ‘uniform’ and defines the minimum and maximum recharge [mm/d] parameters to be used in the component to generate a uniform distribution that is applied uniformly over the model domain. This is the default option used in the component. A code snippet below demonstrates how to provide this information in the driver.

```
#Option - uniform distribution
distribution = 'uniform'
Remin_value = 20.
Remax_value = 120.
```

● **Recharge: ‘lognormal’**

Instead of providing minimum and maximum recharge values, in this option, the user specifies the distribution as ‘lognormal’ and provides the mean and standard deviation parameters of the recharge to be used to calculate mu and sigma for generating a lognormal distribution. This distribution is then applied uniformly over the model domain. A code snippet below demonstrates how to provide this information to the driver.

```
#Option 2 - Lognormal
distribution2 = 'lognormal_uniform'
Remean = 30.
Restandard_deviation = 0.25
```

- **Recharge: 'lognormal_spatial'**

This option allows for spatial representation of recharge. Similar to previous option, this option applies a lognormal distribution to represent recharge from arrays of mean and standard deviation representing recharge at each node. Note that the mean and standard deviation is from the native form of recharge acquired by the user and not a log transformation of the recharge. Additionally, this array must be as long as the *length of all nodes* in the model domain, such that the first mean is for node ID 0. A code snippet below demonstrates how to provide this information to the driver using a random generation of integers for mean recharge from NumPy.

```
#Option - Lognormal-Spatial
distribution = 'lognormal_spatial'
Remean = np.random.randint(20,120,grid_size)
Restandard_deviation = np.random.rand(grid_size)
```

- **Recharge: 'data_driven_spatial'**

This recharge option provides an even more elaborate handling of recharge data. In this option, the user specifies the distribution as 'data_driven_spatial' and three *Python dictionaries* are provided or generated in the driver using the STA utility to make spatially-distributed arrays of recharge at each node while looping through nodes in the component. An example of the driver description using recharge from a HSD that is spatially variable is provided below:

```
#Option - Fully distributed
distribution = 'data_driven_spatial'
HSD_inputs = [HSD_dict,HSD_id_dict, fract_dict]
```

In the application of the model in Strauch et al. (*in review*), we used spatial recharge rates from the Variable Infiltration Capacity (VIC) macroscale hydrologic model (Liang et al., 1994) simulation run at a daily time step for a historical period (water years 1916 to 2006) on a 1/16th° grid resolution (Hamlet et al., 2013). In our application of the model, we focus on landslide risk over the contemporary climate. Assuming landslides would most likely initiate during high water-input (rain and snowmelt) events, we use only the maximum modeled recharge rate in each water year at each VIC grid cell. Using a single recharge value for a year in a Monte Carlo simulation gives an annual probability of shallow landsliding. The native resolution of the VIC hydrology, generically named as '*Hydrology Source Domain*' (HSD) is coarser than the resolution of the landslide model. A separate 'source tracking' algorithm (STA) written as Landlab utility (SourceTracking_UTILITY) is run in the model driver, or in a separate Python script, to map the HSD data to the finer model domain resolution. This algorithm tracks the HSD grid IDs draining to each node of the RasterModelGrid and calculates the fraction of the upstream drainage area contribution from each HSD. This tracking is packaged into two Python dictionaries with both '*keys*' as the RasterModelGrid node ID, and the '*values*' as lists of the HSD grid IDs and the corresponding fraction of each draining HSD grid ID, respectively. These two dictionaries along with a dictionary of the HSD grid ID (*key*) and a numpy array of recharge (*value*) are passed onto the component. The component uses the recharge data from each contributing HSD IDs and generates recharge using a non-parametric method while looping through each node of the RasterModelGrid. Using the other two dictionaries, the recharge at a node is weighted by the upstream contributing fraction from different HSD grids and a 'routed' recharge is calculated for each node (Fig. 1).

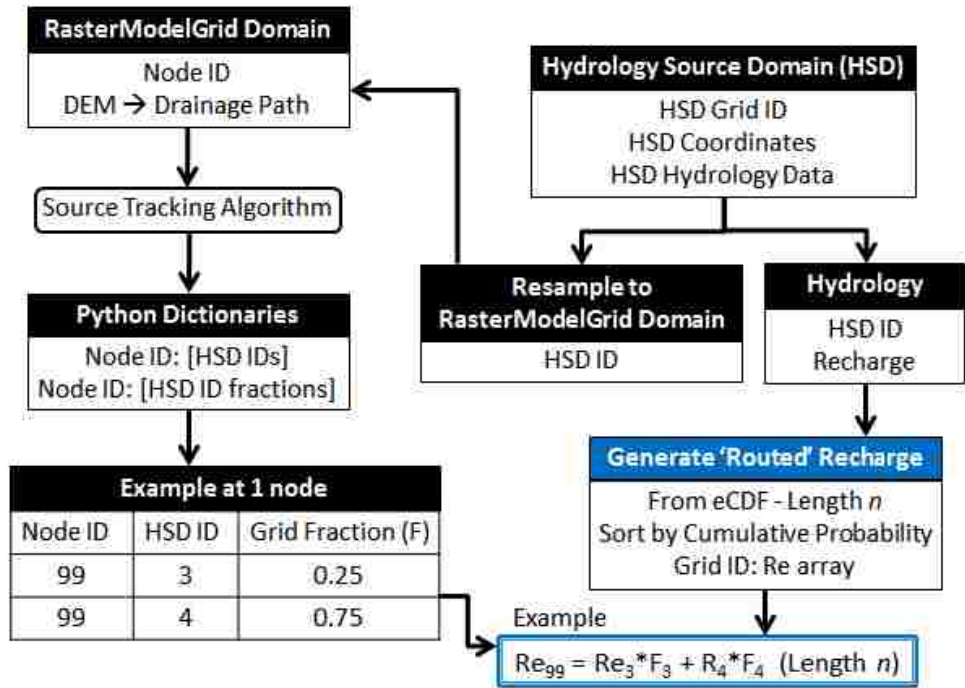


Fig. 1 – Workflow for source routing of recharge when downscaling from macro-scale hydrology to RasterModelGrid. Blue section at bottom right is work being performed inside the LandslideProbability component.

The STA is Landlab utility that traverses a RasterModelGrid, and records all upstream contributing core nodes for each core node. Unique HSD ids that represent the upstream core nodes, for each core node, will be returned as a Python dictionary. For more detailed explanation of the algorithm, refer to STA utility user manual (https://github.com/landlab/pub_strauch_etal_esurf)

3.7. Step 7. Instantiate and run LandslideProbability component

Most Landlab components are structured as a Python class. These classes are imported (as seen in Step 1) and then the user must create an instance of the class as shown below. When the instance of the class is created (e.g., *LS_prob1*), parameters are passed as arguments to the class. All Landlab components take a grid as their first argument. The first argument passes on the grid as named by the user and all subsequent arguments are additional parameters (see section 2.1.) used to control the model behavior. The elegance of Landlab is that all the fields are attached to the grid object and are automatically passed to the component class at once through the 'grid' object. The recharge parameterization and number of iterations are also passed as arguments. Once the component has been instantiated, the component is run to calculate the probability of failure by calling the component's method *calculate_landslide_probability()* in a for loop that performs the calculations at each node. Example syntax are provided below for all four recharge options:

```
# Instantiate and Run the 'LandslideProbability' component
#Uniform
LS_prob1 = LandslideProbability(grid,number_of_iterations=n,
    groudwater_recharge_distribution=distribution1,
    groundwater_recharge_min_value=Remin_value,
    groundwater_recharge_max_value=Remax_value)
LS_prob1.calculate_landslide_probability()
#Lognormal_uniform
LS_prob2 = LandslideProbability(grid,number_of_iterations=n,
    groudwater_recharge_distribution=distribution2,
    groundwater_recharge_mean=Remean,
    groundwater_recharge_standard_deviation=Restandard_deviation)
LS_prob2.calculate_landslide_probability()
#Lognormal_spatial
LS_prob3 = LandslideProbability(grid,number_of_iterations=n,
    groudwater_recharge_distribution=distribution3,
    groundwater_recharge_mean=Remean3,
    groundwater_recharge_standard_deviation=Restandard_deviation3)
LS_prob3.calculate_landslide_probability()
#HSD
LS_prob4 = LandslideProbability(grid,number_of_iterations=n,
    groudwater_recharge_distribution=distribution4,
    groudwater_recharge_HSD_inputs=HSD_inputs)
LS_prob4.calculate_landslide_probability()
```

Probability of failure is calculated at each RasterModelGrid node by solving the infinite slope stability equation for the factor-of-safety index (FS) in a Monte Carlo simulation approach. The equation is solved deterministically by sampling from parameter distributions and calculating the FS for each iteration at each RasterModelGrid node. The probability is determined by the number of iterations where $FS \leq 1.0$, $\text{count}(FS \leq 1.0)/n()$, where n is sample size. The resulting output is a spatially distributed probability of failure over the modeled domain.

This methods within the LandslideProbability class (i.e., the component and not the driver) are described below with code snippets:

calculate_landslide_probability()

- Create arrays for storing output
- Execute a for loop that loops through each node, calculate FS, mean relative wetness, probability of failure, and a histogram of FS values for the last node to check distribution being created.
- Assign mean relative wetness and probability of failure as fields in the RasterModelGrid for later plotting.

```
def calculate_landslide_probability(self, **kwds):
    # Create arrays for data with -9999 as default to store output
    self.mean_Relative_Wetness = -9999*np.ones(self.grid.number_of_nodes,
                                                dtype='float')

    self.prob_fail = -9999*np.ones(
        self.grid.number_of_nodes, dtype='float')
    self.landslide_factor_of_safety_histogram = -9999*np.ones(
        [self.grid.number_of_nodes, self.n], dtype='float')
    # Run factor of safety Monte Carlo for all core nodes in domain
    # i refers to each core node id
    for i in self.grid.core_nodes:
        self.calculate_factor_of_safety(i)
        # Populate storage arrays with calculated values
        self.mean_Relative_Wetness[i] = self.soil_mean_relative_wetness
        self.prob_fail[i] = self.landslide_probability_of_failure
        self.landslide_factor_of_safety_histogram[i] = (
            self.FS_distribution)
        # stores FS values from last loop (node)
    # replace unrealistic values in arrays
    self.mean_Relative_Wetness[
        self.mean_Relative_Wetness < 0.] = 0. # so can't be negative
    self.prob_fail[self.prob_fail < 0.] = 0. # can't be negative
    # assign output fields to nodes
    self.grid['node']['soil_mean_relative_wetness'] = (
        self.mean_Relative_Wetness)
    self.grid['node']['landslide_probability_of_failure'] = self.prob_fail
```

calculate_factor_of_safety()

- This method is called within the previous for loop above. This method generates distributions of the parameters for the individual node and then calculates the FS for the number of iterations (n) specified.
- In the process, this method calculates the relative wetness n times and stores the mean. The mean FS and probability of failure are also calculated.
- The calculated variables and their summary variables are stored in arrays.


```

def calculate_factor_of_safety(self, i):
    # load parameter for node - EXAMPLE
    self.theta = self.grid['node']['topographic_slope'][i]
    # generate distributions to sample from, for some input parameters
    # currently triangle distribution using mode, min, & max
    # Transmissivity (T) - EXAMPLE
    self.Tmode = self.grid['node']['soil_transmissivity'][i]
    Tmin = self.Tmode-(0.3*self.Tmode)
    Tmax = self.Tmode+(0.1*self.Tmode)
    self.T = np.random.triangular(Tmin, self.Tmode, Tmax, size=self.n)
    # recharge distribution based on distribution type
    if self.groundwater_recharge_distribution == 'data_driven_spatial':
        self._calculate_HSD_recharge(i)
        self.Re /= 1000.0 # mm->m
    elif self.groundwater_recharge_distribution == 'lognormal_spatial':
        mu_lognormal = np.log((self.recharge_mean[i]**2)/np.sqrt(
            self.recharge_stdev[i]**2 + self.recharge_mean[i]**2))
        sigma_lognormal = np.sqrt(np.log((self.recharge_stdev[i]**2)/(
            self.recharge_mean[i]**2)+1))
        self.Re = np.random.lognormal(mean=mu_lognormal,
            sigma=sigma_lognormal,
            size=self.n)

# calculate Factor of Safety for n number of times
# calculate components of FS equation
self.C_dim = self.C/(self.hs*self.rho*self.g) # dimensionless cohesion
self.Rel_wetness = ((self.Re)/self.T)*(self.a/np.sin(
    np.arctan(self.theta))) # relative wetness
np.place(self.Rel_wetness, self.Rel_wetness > 1, 1.0)
# maximum Rel_wetness = 1.0
self.soil_mean_relative_wetness = np.mean(self.Rel_wetness)
self.Y = np.tan(np.radians(self.phi))*(1 - (self.Rel_wetness*0.5))
# convert from degrees; 0.5 = water to soil density ratio
# calculate Factor-of-safety
self.FS = (self.C_dim/np.sin(np.arctan(self.theta))) + (
    np.cos(np.arctan(self.theta)) *
    (self.Y/np.sin(np.arctan(self.theta))))
self.FS_store = np.array(self.FS) # array of factor of safety
self.FS_distribution = self.FS_store
count = 0
for val in self.FS: # find how many FS values <= 1
    if val <= 1.0:
        count = count + 1
self.FS_L1 = float(count) # number with unstable FS values (<=1)
# probability: No. unstable values/total No. of values (n)
self.landslide_probability_of_failure = self.FS_L1/self.n

```

4. Exporting, Plotting and Visualization

4.1. Exporting

There are several ways to assess results. Some users may elect to extract results into a dataframe and write the dataframe to a .csv file. This file can then be read and analyzed externally in other Python scripts, 'R', Matlab, etc. Landlab also provides a function to write field assigned to the RasterModelGrid into ASCII files that can be converted to rasters in a GIS program. Code examples for these options are shown below.

```

# %% Export data
# extract data into a .csv file
data_extracted = {'prob_fail': np.array(
    grid.at_node['landslide__probability_of_failure'][grid.core_nodes]),
    'slope_tan': np.array(
    grid.at_node['topographic__slope'][grid.core_nodes]),
    'wetness': np.array(
    grid.at_node['soil__mean_relative_wetness'][grid.core_nodes])}
headers = ['prob_fail', 'slope_tan', 'wetness']
df = pd.DataFrame(data_extracted, index=core_nodes, columns=(headers))
df.to_csv('LS_results.csv') # creates a .csv file with headers
# extract data into a axcii file able to be converted to a raster in ArcGIS
write_esri_ascii('prob_fail.txt', grid, names='landslide__probability_of_failure')

```

4.2. Plotting and Visualizing

After the model is run, both inputs and outputs can be plotted using the matplotlib library. Below is an example for plotting a parameter (slope) assigned to the RasterModelGrid. For more customization options, the matplotlib.pyplot documentation is recommended: http://matplotlib.org/api/pyplot_api.html.

```

# %% Figures & Plots
# fields on grid
plt.clf
plt.figure('Slope (tan theta)')
imshow_node_grid(grid, 'topographic__slope', cmap='pink',
    grid_units=('coordinates', 'coordinates'), vmax=2.,
    shrink=0.75, var_name='Slope', var_units='m/m')
plt.savefig(outdir+'Slope.png', dpi=300)

```

The output for the above code is shown below. This is for a portion of North Cascades National Park Complex in northern Washington (Fig. 2). Black areas are excluded portions of the domain.

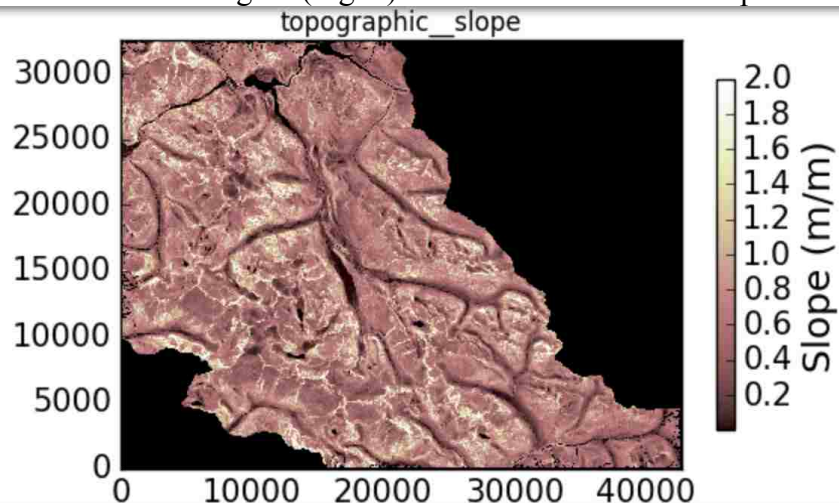
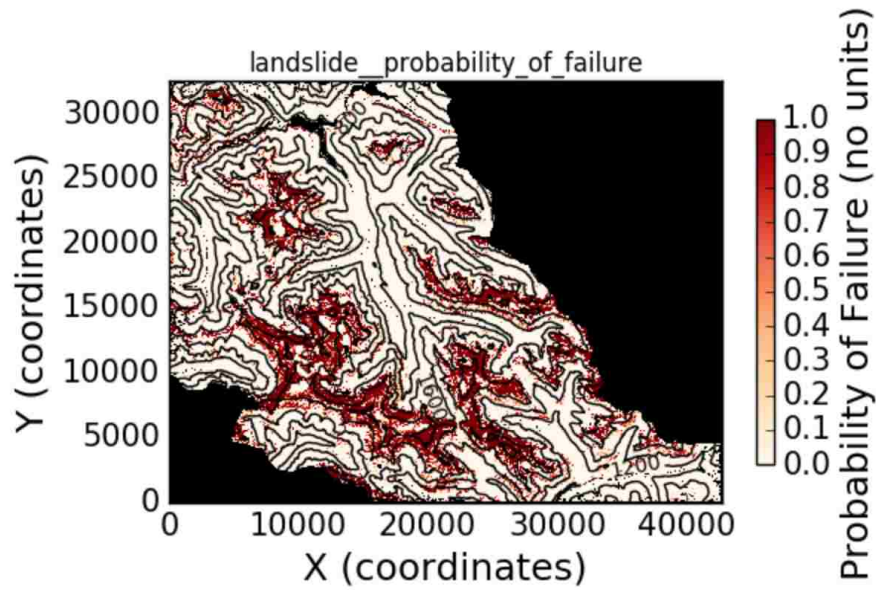


Fig. 2 – Slope (dimensionless) used as an input in the LandslideProbability component.

Adding contours helps interpret the inputs and results. These can be created using the z array containing elevation generated in Step 2 above when creating the RasterModelGrid from a DEM. The example below is the probability of failure estimated the same area above with Monte Carlo simulation (Fig. 3).



```
plt.figure('Probability of Failure')
imshow_node_grid(grid, 'landslide_probability_of_failure', cmap='OrRd',
                 grid_units=('coordinates', 'coordinates'), shrink=0.75,
                 var_name='Probability of Failure', var_units='no units')
elev = grid.node_vector_to_raster(z)
# control contour extent with labels
cs = pylab.contour(elev, extent=[0,42500, 0,32500], hold='on', colors='black')
manual_locals = [(11000,11000), (14000,30000), (20000,8000), (36000,3000)]
pylab.clabel(cs, inline=True, fmt='%1i', fontsize=10, manual=manual_locals)
plt.savefig(outdir+'Prob_failure.png', dpi=300)
```

Fig. 3 – Probability of failure estimated for a portion of the park from the LandslideProbability component. Code used to generate plot is provided below the figure.

5. References

- Cho SE. (2007) Effects of spatial variability of soil properties on slope stability. *Engineering Geology*, 92(3): 97-109.
- El-Ramly H, Morgenstern NR, and Cruden DM. (2002) Probabilistic slope stability analysis for practice. *Canadian Geotechnical Journal*, 39(3): 665-683.
- Hamlet AF, Elsner MM, Mauger GS, Lee S, Tohver I, Norheim RA. (2013) An Overview of the Columbia Basin Climate Change Scenarios Project: Approach, Methods, and Summary of Key Results. *Atmos Ocean*. 51(4): 392-415.
- Hammond C, Hall D, Miller S, & Swetik P. (1992) Level 1 stability analysis (LISA), documentation for Version 2.0. USDA, For. Serv., Moscow, ID, Intermountain Res. Sta. Gen. Tech. Rep. INT-285.
- Hobley DEJ, Adams JM, Nudurupati SS, Hutton EWH, Gasparini NM, Istanbuluoglu E, and Tucker GE. (2017) Creative computing with Landlab: an open-source toolkit for building, coupling, and exploring two-dimensional numerical models of Earth-surface dynamics, *Earth Surf. Dynam.*, 5: 21-46, doi:10.5194/esurf-5-21-2017.
- Jin S, Yang L, Danielson P, Homer C, Fry J, and Xian G. (2013) A comprehensive change detection method for updating the National Land Cover Database to circa 2011. *Remote Sensing of Environment*, 132: 159-175.
- Montgomery DR, and Dietrich WE. (1994) A Physically Based Model for the Topographic Control on Shallow Landsliding, *Water Resources Research*, 30(4): 1153-1171.
- Pack RT, Tarboton DG, Goodwin CN (1998) The SINMAP approach to terrain stability mapping. In: *Proceedings of the 8th international congress of the international association of engineering*

- geology and the environment, Vancouver, British Columbia, Canada, September 21–25, vol 2. AA Balkema, Rotterdam, pp 1157–1165.
- Peckham SD. (2014) The CSDMS standard names: cross-domain naming conventions for describing process models, data sets and their associated variables, in: Proceedings of the 7th International Congress on Environmental Modeling and Software, edited by Daniel P. Ames, Nigel W. T. Quinn, A. E. R., International Environmental Modelling and Software Society (IEMSs), San Diego, California, USA.
- Strauch RL, Istanbuluoglu E, Nudurupati SS, Bandaragoda C, Gasparina N, and Tucker G. (in review). Hydro-climatological approach to predicting regional landslide probability. *Earth Surface Dynamics*.
- USGS. (2014) National Land Cover Data (NLCD) version Marched 31, 2014. National Map Viewer [Accessed November 25, 2014].

Chapter 4. A new approach to mapping landslide hazards: integration of statistical and process-based models in the North Cascades of Washington, U.S.A.

Abstract

We developed a new approach for mapping landslide hazard by integrating probabilities of landslide impact derived from a data-driven statistical approach and process-based model of shallow landsliding. Our statistical approach integrates the influence of seven site attributes on observed landslides using a frequency ratio method. Influential attributes and resulting susceptibility maps depend on the observations of landslides considered: all types of landslides, debris avalanches only, or source areas of debris avalanches. These observational datasets reflect the capture of different landslide processes or components, which relate to different landslide-inducing factors. Slopes greater than 35° are more frequently associated with landslide initiation, while higher landslide hazards at gentler slopes ($<30^\circ$) reflect depositional processes from observations of all landslide types or debris avalanches. Source areas are associated with mid to high elevations (1,400 to 1,800 m), linked to ecosystem transition (e.g., forest to barren), while all landslides types and debris avalanches show increasing frequency in lower elevations ($< 1,200$ m). Slope is a key attribute in the initiation of landslides, while lithology is mainly linked to transport and depositional processes. East (west) aspect is a positive (negative) landslide-influencing factor, likely due to differences in forest cover and associated root cohesion. The empirical map derived from all landslide types is combined with a previously developed physically-based probabilistic map to produce an integrated probabilistic map of landslide hazard for initiation, transport, and deposition processes. We apply our approach in North Cascades National Park Complex in Washington, USA, to provide multiple landslide hazard maps that land managers can use for planning and decision making, as well as educating the public about hazards from landslides in this remote high-relief terrain.

4.1 Introduction

Landslides disrupt aquatic habitats (May et al., 2009; Pollock 1998), damage infrastructure such as roads, utilities, and dams (Ghirotti, 2012; Baum et al., 2008), and harm people (Wartman et al., 2016; Taylor and Brabb, 1986). Landslide hazards are expected to grow globally with growing extremes in the climate (Coe 2016; Haeberli et al. 2016; Crozier 2010). Maps of landslide hazards, quantified as a probability of landslide initiation or impact, are developed in a number of different ways, including various empirical methods that use the location of existing landslides to statistically infer potential instability and process-based models that relate geotechnical properties of hillslopes and hydro-climatic input to landslide susceptibility. While detailed quantitative and categorical climatic, geologic, ecologic, and pedologic information can be used in statistical models, process-based model inputs are more limited to hydrologic and geotechnical properties of soils and plant root cohesion, which are sometimes not sufficient to represent impacts of local geology and microclimate for landslide initiation. To date, data-driven empirical research on landslide hazard mapping (Corominas et al. 2012; Lee 2005; Chung and Fabbri 2003) has been typically conducted independently from hydroclimate-driven modeling of landslides that largely focus on hydrologic controls on landsliding (Wooten et al., 2016; Cevasco et al., 2014). There is need for unifying these two lines of research to provide regional scale

landslide prediction for resource management and hazard mitigation strategies. This need is addressed in the North Cascades region of the state of Washington, USA using field observations and modeling.

Most mountain ranges are susceptible to landsliding due to their steep geomorphology, loose soil development, geology, and high precipitation (Coe 2016). Although advancements in landslide hazard assessment and prediction are improving with more advanced computational ability (Anagnostopoulos et al., 2015; Bellugi et al., 2015, Bordoni et al., 2015; Baum et al. 2014), it continues to be challenging to apply models at large scales for a wide variety of landslide types (van Westen et al., 2006; Corominas et al., 2014). Physically-based models require considerable data on the spatial-temporal characteristics of the landscape and triggering hydrometeorologic events. These models are also usually restricted to a specific type of landslide and can be limited in representing local geologic, soil, and hydrologic conditions that may be difficult to observe and map in the field and parameterize in model theory and relate to triggering mechanisms. On the other hand, while empirical models of landslide potential cannot represent the triggering conditions that drive process-based models, they can help fill in the gap in static conditions that lead to landslide-prone landscapes, such as geological susceptibility, when landslide inventories exist. Linking these physically and empirically-based models can improve the spatial-temporal patterns of landslide hazard at medium to large scales to provide support tools for authorities addressing risk management.

Statistical, empirically-based landslide susceptibility approaches indirectly account for hydrologic and soil mechanistic processes. These models assess the inherent or quasi-static stability of hillslopes derived from statistical associations (e.g., correlations) between site attributes or characteristics and an inventory of past landslides (e.g., Dai and Lee 2002; Gupta and Joshi 1990; Pachauri and Pant 1992; Kirschbaum et al. 2012). These models focus on prevailing conditions that predispose hillslopes to failure (Hungry et al., 2014), typically providing general indices of relative landslide susceptibility or spatial probabilities applicable to the study location and cannot represent causal factors or triggering conditions that change in time (van Westen et al. 2006; Sidle and Ochiai 2006). Empirically-based modeling provides the ability to capture hillslope preconditioning or physical processes that are not represented by simplified process-based approaches by incorporating potential site-specific factors affecting landsliding, but poorly quantified by theory. Outcome of such analyses depend on the completeness of observations, hindering the use of such techniques over large areas where complete inventories are typically lacking. Since empirical models are based on observation of past landslides, the preconditioning relationships are assumed to prevail into the future until an updated study is completed (Lepore et al., 2012).

The Frequency Ratio (FR) method is a commonly used statistical approach to identifying landslide susceptibility and has been found to perform as well as more rigorous statistical approaches such as logistic regression (Hong et al., 2017; Wu et al. 2017; Lepore et al. 2012; Kirschbaum et al. 2012; Lee et al. 2007; Lee and Pradhan 2006). We use this bivariate methodology to relate landslide occurrence to seven surface attributes (SAs) through direct and indirect measures. Slope, curvature, and lithology directly affect the forces and geotechnical properties in surface sediments. Land cover provides a surrogate for root cohesion and topographic wetness index has been used as a surrogate for soil pore water pressure (Borga et al

2002). Elevation can represent the effects of climate, weathering, vegetation, ground motion, and glacial processes, if any, as well as coincide with variability in slope, soil depth, and land use (Sidle and Ochiai 2006). Aspect provides an indication of solar insolation, vegetation type and cover density, snow and ice loading, and soil moisture levels via evapotranspiration (Beatty 1956; Gokceoglu et al. 2005).

We compared the FR empirical landslide assessment to a recently completed physical model (Strauch et al. 2017) to understand the SAs that may predispose a hillslope to failure as well as the landslide hazard patterns developed from these two approaches. The landslide assessment using a physical model was based on the infinite-slope stability model that solves the ratio of stabilizing to destabilizing forces on a failure plane parallel to the land surface. This model predicts the spatial-temporal probability of shallow landslide initiation triggered by rainfall and snowmelt. Building on the advantages from the empirical and physical models, we integrated the two models to develop an integrated map of landslide hazard. The integrated map can be used to identify landslide hazards that may originate from either the initiation of landslides or the transport and deposition (i.e., runout) of the landslide material (Fig. 4.1). Using this approach, we investigate the: (1) pre-conditioning factors, especially lithology, that correlate with mapped landslides, (2) variability in SAs and estimated hazard based on different mapped landslide features, (3) potential mechanisms related to SAs and landslides, and (4) differences from empirical hazard identification and probability of landslide initiation derived from the physical model.



Figure 4.1 - Primary landslide features showing source, transport, and deposition areas illustrated over aerial image from Google Earth taken July 2016. Location in North Cascades National Park Complex about 4 km north of Newhalem, Washington.

This paper describes research designed to address the following questions: 1) How can we quantify relative contributions of local topography, geology, and ecology on landslide frequency and derive spatial probabilities of landsliding using a statistical model? 2) How would

probabilities of landslide initiation derived from empirical observations compare with those derived from process-based models? 3) How can we combine empirical and process-based models for landslide susceptibility to improve the prediction of landslide hazards? The organization of this paper is as follows. Our methodology is discussed in Section 4.2, including the FR method, model application, data compilation, and model integration approach. Section 4.3 details our results of the FR application and susceptibility index as well as various hazard maps developed. We end with some overall concluding thoughts.

4.2 Methodology

4.2.1 Frequency Ratio

We characterized the susceptibility of hillslopes to landslide impact using an empirically-based Frequency Ratio, FR, approach (Lee et al., 2007; Kirschbaum et al., 2012). This bivariate approach relates the spatial data of selected SAs (e.g. slope, lithology, vegetation) and their subcategories (e.g., lithology class, vegetation type) to areas with and without historically identified landslides. Subcategories of each SA can be a categorical variable such as type of lithology or a quantitative variable defined with certain ranges such as slope and aspect. For a given SA, identified by m , and its subcategory, n , $FR_n|SA_m$ is calculated (Eq. 1) as the ratio of the fraction of landslide area in each subcategory ($LA_{SA_{m,n}}$) with respect to the landslide area within the entire study domain, SD , (LA_{SD}), to the area fraction of the selected SA subcategory within the SD ($A_{SD_{m,n}}$) with respect to the area of the study domain (A_{SD}). $FR_n|SA_m$ is essentially an odds ratio, and rearrangement of the terms leads to a density ratio of landslides for the subcategory n of SA m over the landslide density for the SD (Miller and Burnett 2007).

$$FR_n|SA_m = \frac{LA_{SA_{m,n}} / LA_{SD}}{A_{SA_{m,n}} / A_{SD}} \quad (1)$$

The interpretation of FR is as follows (Lepore et al. 2012):

- $FR < 1$: indicates proportionally less landslide area with subcategory n of SA m , than in the entire SD for the same attribute subcategory; hence the odds of a landslide are less in SA m subcategory n than the SD .
- $FR \approx 1$: means there is roughly the same proportion of landslide areas with SA m in subcategory n as in the SD for the same attribute subcategory; thus, the odds of a landslide are the same for the SA subcategory as the SD .
- $FR > 1$: reveals a higher percentage of landslide area with subcategory n of SA m , than in the entire SD for the same attribute subcategory, so there is a propensity or greater odds for failures to occur with this SA subcategory compared to the SD .

A susceptibility index, SI , integrates these FRs and is calculated (Eq. 2) at each grid cell, i , of the SD as the sum of FR values for all SAs and their associated subcategory. SI is a measure that relates local static (or slowly changing) site characteristics to relative frequency of landslides. High SI values indicate an increased frequency of landslides, while low SI values suggest low landslide frequency, within the timeframe of the identified landslides based on the SA considered. Probability of landslide ($P(LS_r|SI_r)$) is derived from SI by binning SI and calculating the ratio of number of grid cells with landslides $N(LS)$ to the number of all grid cells, N , within each SI bin, r , N_r (Eq. 3).

$$SI_i = \sum_m \sum_n FR_n | SA_m \quad (2)$$

$$P(LS_r | SI_r) = \frac{N(LS)_r}{N_r} \quad (3)$$

To calculate spatially continuous empirical probability of landsliding at each grid cell of a DEM, we used the binned SI-based probability estimates. We first developed empirical relationships between SI and $P(LS_r | SI_r)$ for all landslide types or select landslide features and used these empirical functions across the landscape with SI defined at each grid cell to estimate probability of landslide impact at each cell. These probabilities are assumed to represent spatial maps of empirical landslide probability based on the static landscape attributes used in the analysis.

We considered seven SAs in our analysis: slope, elevation, aspect, curvature, land use-land cover (landcover), lithology, and topographic wetness index. We included all SAs to develop empirical models relating SI to landslide probability, similar to Kirschbaum et al. (2012) and Lepore et al. (2012). Our first analysis considered all landslide types together, as is commonly done in multi-factor analyses (Sidle and Ochiai 2006; Ayalew et al. 2004; Carrara et al. 1991). Our second model focused on debris avalanches, including their initiation, transport and deposition areas, as a whole (Fig. 4.1). In a third model, we considered only the source (initiation) areas of debris avalanches, identified as the upper 20% of elevation within mapped debris avalanche polygons. This tiered approach can be used to quantify the relative contributions of different landslide features to overall landslide hazard in a region. We hypothesize that empirical probabilities estimated by relating landslide observations to site attributes that are not directly used in physical models of landslide initiation can be “fused” with physical models to improve predictions of additional landslide processes other than initiation alone.

4.2.2 Model application

4.2.2.1 Study Area

Our study area is within the geographical limits of North Cascades National Park Complex (NOCA) managed by the U.S. National Park Service. NOCA has experienced damaging and disruptive landslides that have impacted infrastructure and disrupted public use of the park. NOCA is approximately 2,757 km², with 93% wilderness (e.g., no motorized or mechanized devices) (DOI-NPS 2012), which is ideal for studying landslides primarily triggered by natural causes. The landscape is rugged (elevation ranging from 100 to 2,800 m) with over 300 alpine glaciers, jagged peaks, and numerous streams. The north-south oriented Cascade Mountains and storms, typically originating from the west, lead to a strong rainshadow effect (Mustoe and Leopold 2014; Roe 2005). Orographic uplift of Pacific Ocean air masses generate a spatial precipitation gradient with an average of 4,575 mm of precipitation falling annually on the highest elevations west of the crest, while lowlands east of the crest receive a mean annual precipitation of 708 mm. Air temperatures vary highly depending on season and elevation with the warmest month typically August and the coldest month is January; average daily high and low is about 25° C and 4° C, respectively, for these months in Newhalem, Washington.

Vegetation in NOCA is dominated by forest, particularly coniferous tree species, up to about 2,000 m (Strauch et al. 2017; Agee and Kertis 1987). A patchwork of shrubs, herbaceous

vegetation, and barren land is found above this elevation common in alpine environments and in the paths of frequent snow avalanches. Above 2,400 m is mostly barren landscape. The underlying geology is composed of a primarily old Mesozoic crystalline and metamorphic rock originating far to the south (Haugerud and Tabor 2009). The landscape has been shaped by Ice Age glaciers, alpine glaciers, rivers, and mountain uplift that continues today (LaHusen et al. 2016; Mustoe and Leopold 2016; Collins and Montgomery 2011; Pelto and Riedel 2001).

Landslide (LS) inventory data are the most requisite information needed for an empirical statistical analysis (Lepore et al. 2012). Landslides were mapped in the park as *mass wasting* landforms during a park-wide landform mapping study by the National Park Service (NPS) scientists at NOCA (Fig. 4.2; Riedel and Probala 2005). Landslides were identified using color stereo-pair 1998 air photos at 1:12,000 scale, 7.5 minute topographic maps, bedrock geology maps, and field investigations (e.g., Riedel et al. 2012). The minimum mapping unit was approximately 1,000 m² except for some smaller slump units. Landslide linework was transferred to a digital format, peer reviewed, and polygons edited into final form in geographical information system (GIS) software using National Agriculture Imagery Program (NAIP) imagery and 10-m DEM. The park-wide landform mapping study identified six different types of mass wasting: rock fall/topple, debris avalanche, debris torrent, slump/creep, (Table 4.1) sackung, and snow avalanche-impacted landforms (SAILs) (Riedel et al.2012). The single sackung mapped in NOCA represents a gravitational spreading or slope deformation, sometimes found near ridge tops. All landslide types were included in the analysis except for SAILs, which are created by snow avalanche impacting unconsolidated sediments rather than slope instability. There are 1618 landslides mapped in NOCA: falls/topples (68%), debris avalanches (17%), debris torrents (10%), slumps/creeps (4%), and one sackung (<1%) (Fig. 4.2; sackung not shown).

4.2.2.2 Study domain and Parameters

We constrained our analysis to soil-mantled landscapes by excluding high elevation areas covered by glaciers, permanent snowfields and exposed bedrock, as well as wetlands and other water surfaces, based on landform mapping and maps of lithology and landcover. We also exclude slopes less than 17° because this slope threshold was found to generally separate colluvial mass wasting and debris transport processes from fluvial processes in this region (Strauch et al. 2017). The area included in the analysis covers about 79% of NOCA's land area.

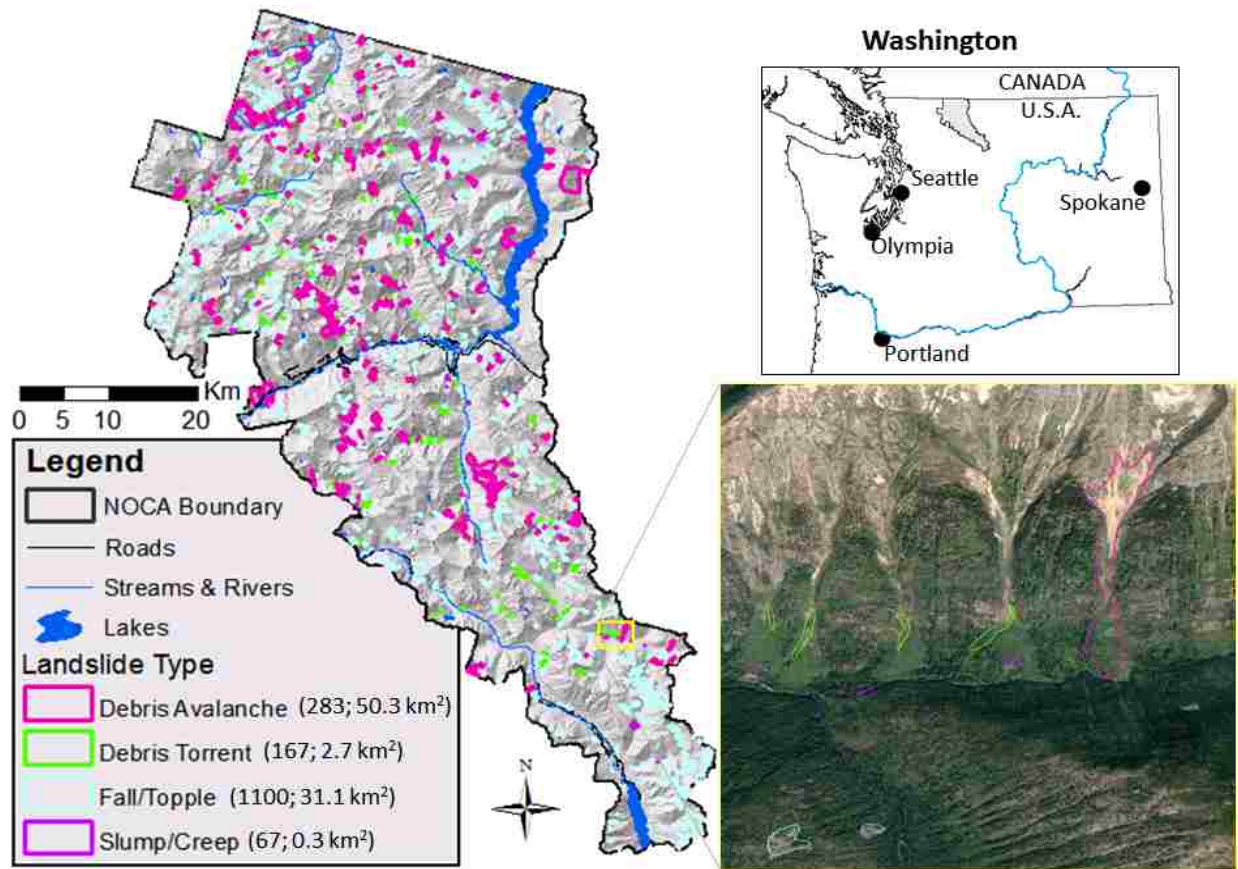


Figure 4.2 - Four landslide types mapped within North Cascades National Park Complex (NOCA) in Washington, U.S.A. The number and their total area of each type is given in parentheses. Insert provides example of mapping over aerial image from Google Earth.

Table 4.1 - Landslides mapped as part of landform mapping study used in hazard analysis

Type	Process	Mapping
Debris Avalanche	Extremely rapid moving mixture of rock and debris, generally originates from glacially-sourced areas, over-steepened valley walls, and in many cases on hydrothermally altered bedrock	Includes headwall scar, path, and deposit
Debris Torrent	Channelized rapid and/or sudden flow of material entraining debris stored in stream channel while moving down slope	Only the deposition areas within a debris cone
Slump and Creep	Slumps - rotational slip of cohesive sediments, usually triggered by undercutting of steep slopes along riverbanks. Creeps - slow movement induced by saturated ground	Mapped where deciduous vegetation brighter on aerial photos, fresh new soil, jackstraw or pistol gripped trees
Rockfall or Rock Topple	Sporadic and shallow detachment of rock falling from bedrock cliffs and rock towers	Mapped where bright and highly reflective with little or no vegetation on aerial photos. Mainly deposition mapped

The seven site attributes (SAs) investigated using the Frequency Ratio (FR) approach as they relate to mapped landslide activity vary across the NOCA study area. Slope, total curvature (Laplacian of elevation), and aspect attributes were derived using ArcGIS from a 30-m digital elevation model (DEM) acquired from National Elevation Dataset (NED) (USGS 2014a). A resolution of 30-m was chosen for comparability with other studies (e.g., Strauch et al. 2017; Lepore et al. 2012). Elevation ranges from 107 to 2794 m with 85% of the park between 500 to 2000 m. Subcategories for elevation were based on 200-m increments with lumping at the ends (e.g., <400 m and > 2200 m). Slope subcategories were set at 5° increments with end subcategories for slopes 17-25°, and >50°. Curvature was divided into three subcategories: convex/diverging, flat, or concave/converging. Aspect (i.e., facing direction of slope) was classified into eight compass orientations (i.e., N, NE, E, SE, S, SW, W, NW). The park's complex topography results in roughly equal distribution among the cardinal and intercardinal directions of aspect; however, the southwest quadrant is slightly more common.

The DEM also provides the information needed to derive a distributed wetness index (Beven and Kirkby 1979; O'Loughlin 1986), calculated as the natural log of the ratio of specific catchment area [L] to sine of local slope. This index has been used for quantifying the contribution of pore-water pressure to destabilizing forces in landslide modeling (e.g., Borga et al 2002; Gokceoglu et al. 2005). Wetness index was divided into 5 subcategories based on 20% quantiles: low, low-medium, medium, medium-high, and high wetness. Landcover was acquired from the 2014 National Land Cover Data (NLCD), which is based on 2011 Landsat satellite imagery (Jin, 2013; USGS, 2014b). We categorized this into forest, shrubland, herbaceous, water, wetland, snow/ice, barren, and developed (e.g., roads, campgrounds). Based on this classification, forest, shrubs, and herbaceous vegetation represent 54%, 15%, and 10% of the park, respectively. Barren and snow or ice combined cover 17%, typically at the high elevations. Water and wetlands cover about 2.5%, while developed is less than 0.5%.

Lithology provides a description of rock and deposits that indicates composition, strength, and age, which can influence the hillslope strength and water redistribution. Washington State Department of Natural Resources (WADNR) provides lithology in its surface geology maps that display rocks and deposits as geologic map units (WADNR 2014). This source of information was chosen because it is available for all of Washington, facilitating future applications. There are 48 lithology map unit types within NOCA. These were aggregated into seven subcategories, based on similarities in origin and generally increasing strength, called: (1) unconsolidated sediment, (2) ultramafic, (3) weak metamorphic foliated, (4) sedimentary rock, (5) hard metamorphic, (6) intrusive igneous, and (7) volcanic/extrusive igneous (Table 4.2). Water and ice were not classified. Both landcover and lithology were rasterized to the same DEM grid resolution using ArcGIS based on the dominant type of attribute in each grid cell. Among the seven types of lithology, hard metamorphic is most common (41% of NOCA), while ultramafic, sedimentary rock, and volcanic/extrusive igneous combined make up less than 5%.

Table 4.2 – Classification of Washington Department of Natural Resources surface geology from generally weaker (1) to stronger (7) material along with aerial percentages within NOCA in parentheses

Class	WADNR Lithology	Class	WADNR Lithology
Unconsolidated Sediments (12%)		Sedimentary Rock (2%)	
1	alluvial fan deposits	4	sedimentary deposits or rocks, undivided
	alluvium		continental sedimentary deposits or rocks
	alluvium, older (e.g., alluvial fans & talus)		marine metasedimentary rocks
	alpine glacial drift, Fraser-age		marine sedimentary rocks
	alpine glacial till, Fraser-age	Hard Metamorphic (41%)	
	glacial outwash, alpine, Fraser-age	5	banded gneiss
	continental glacial drift, Fraser-age		mixed metamorphic and igneous rocks
	mass-wasting deposits		orthogneiss
	mass-wasting deposits, mostly landslides		paragneiss
	mass-wasting deposits, not landslides	Intrusive Igneous (21%)	
	peat deposits	6	acidic (felsic) intrusive rock
	talus deposits		basic (mafic) intrusive rocks
Ultramafic (0.02%)			diorite
2	ultrabasic (ultramafic) rocks (<i>serpentine</i>)		gabbro
Weak Metamorphic Foliated (14%)			granite
3	heterogeneous metamorphic rocks		granodiorite
	hetero. metamorphic rocks, chert bearing		Intermediate intrusive rocks
	marble		Intrusive breccia
	metasedimentary and metavolcanic rocks		quartz diorite
	metasedimentary rocks		quartz monzonite
	metasedimentary rocks, cherty	tonalite	
	metavolcanic rocks	Volcanic/Extrusive Igneous (2%)	
	amphibolite	7	tuffs and tuff breccias
phyllite, low grade	dacite flows		
schist, low grade	rhyolite flows		
--	Water and Ice (7%)		volcanic breccia

4.3 Results and Discussion

4.3.1 Frequency Ratio Analysis

The results of the FR analyses for each site attribute (SA) are presented in Fig. 4.3. We discuss the role of SA starting with debris avalanche source areas as they are hypothesized to represent the initiation processes of shallow landslides that transform into debris avalanches. The SAs that impact shallow landslide initiation could arguably play common controls on the initiation of other types of slope failures. The frequency analysis shows a clear and growing control of local slopes greater than 35° on landslide initiation, which can be considered as the internal friction angle of cohesionless sand (Fig. 4.3c). The source area of debris avalanches is only about 17% of the mapped debris avalanche area and 10% of the whole landslide inventory, which predominantly maps transport and depositional areas. A small debris avalanche source area in steep terrain can lead to large landslide impacts in lower elevations, as the eroded material

travels downhill and deposits in gentler gradients. Thus, the runout zones of debris avalanches and other mapped landslide types cover more area at gentler slopes typical of lower elevations. This process is captured in Fig. 4.3a and Fig. 4.3b where the FR analyses exhibit higher landslide hazard at gentler slopes ($<30^\circ$), more likely associated with transport and depositional processes as well as failure of side slopes along glacially incised U-shaped valleys undercut by fluvial activity. Others have reported clustering of landslide impacts in lower elevations within valleys where hillslopes are steep enough to fail (Megahan et al. 1978; Kelsey 1988; Densmore et al., 1997; Chalkias et al. 2014).

In the study area, local slopes generally increase on average with elevation, particularly above 1,400 m (Strauch et al., 2017). The control of steeper slopes on debris avalanche initiation is supported by the results for elevation where source areas are associated with mid to high elevation (1,400 to 1,800 m) and entire debris avalanches and all landslides types (including deposition) have growing frequency in lower elevations ($< 1,200$ m) with the highest frequency falling in elevations <400 m (Fig. 4.3a, b). Further increase in slopes typically lead to bedrock exposure and barren lands that undergo nonlinear creep processes (Strauch et al., 2017; Gabet 2003; Montgomery 2001; Pack et al., 1998). In addition to steepening slopes, the observed higher frequency of debris avalanche source areas in the mid-to-high elevation range corroborates recent findings of an ecosystem transition control on landslide initiation (Strauch et al. 2017). With the cooling of air temperatures beyond forest ecosystem thresholds, the transition of forest vegetation (predominant alpine conifers) to mixed shrub and herbaceous vegetation types and barren lands with lower root cohesion, lead to higher landslide frequency at debris avalanche source areas (Fig 4.3c). The slope and elevation results, however, are likely influenced by the mapping approach, which was biased in mapping landslide activity on the lower portions of hillslopes that were typically more accessible, and continuous creep and rapid slides in barren subalpine and alpine areas were infrequently mapped.

Developed areas have the highest landcover association with all mapped landslide areas, as well as with debris avalanches, yet no association with debris avalanche source areas. This suggests that development activities, typically at lower elevations in mountains, may be linked to landslides more as an impact from landslides rather than as a causative agent of landslides in this study area. Although dirt roads have been found to disrupt drainage and increase erosion (Croke and Hairsine 2006; Montgomery 1994; Swanson and Dyrness 1974), these impacts are not evident in NOCA based on the mapped landslides. In general, forest and barren landcover show the least landslide activity compared to other landcover (Fig. 4.3). The forest association likely indicates the positive contribution of root cohesion to hillslope stability, whereas the barren landcover type results may indicate the effect of mapping completeness or hillslope processes. The barren results appear counter to the findings of the physically-based landslide model applied at the same location, which found high probability of landslide initiation in barren areas often below retreating glaciers (Strauch et al. 2017). However, the FR approach is normalized by area; thus, a relatively small number of debris avalanche cells within the barren landcover class can lead to low FR values compared to the number of debris avalanche cells within the vegetated areas further downslope where debris avalanches deposit material.

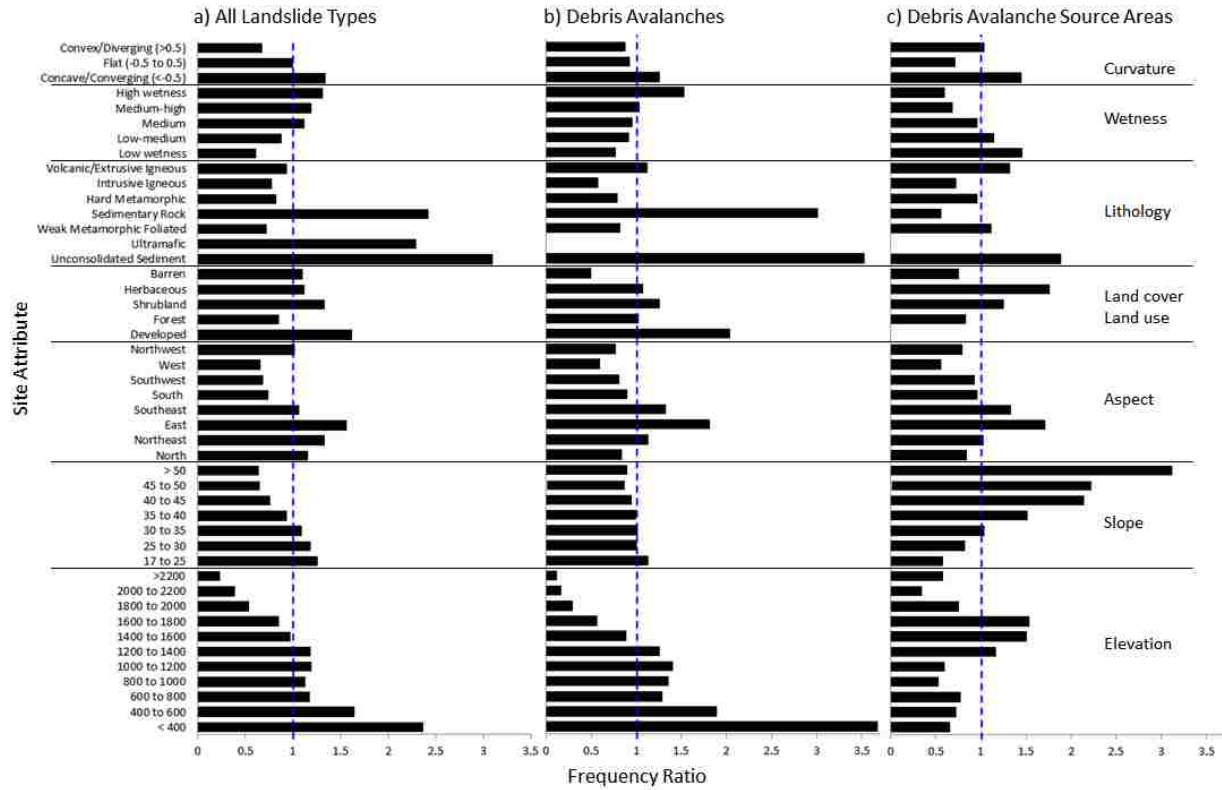


Figure 4.3 – FR value for different bins of seven SAs based on: **a)** all landslide types mapped within the NOCA study domain, **b)** debris avalanche landslide types only, and **c)** source areas of debris avalanches represented by the highest 20% of the mapped debris avalanche. The vertical blue dashed line refers to the FR value of 1.0, denoting when no association is found with mapped landslides.

The sources of debris avalanches are linked to eastern and southeastern aspects; 20% and 15% of source cells by area occur on these aspects, respectively (Fig. 4.3c). Except for western aspects that show the weakest association with landsliding, other aspects show landsliding frequency close to the average frequency in the whole study domain. We suspect that aspect is linked to vegetation and moisture regime, which are physical factors affecting the mechanics of soil strength. East and south exposures have lower forest cover fractions compared to other aspects at mid to lower elevations (< 1,400 m), and forests are largely replaced by barren lands and shrub and herbaceous vegetation as elevation increases (Fig. 4.4). Most source areas of debris avalanches are associated with shrub and herbaceous vegetation types (Fig. 4.3b, c). Other aspects, especially west-facing slopes have higher fraction of forest cover, likely linked to a longer growing season (Evans and Fonda 1990). Lower landslide frequency in western aspects can be a result of higher root cohesion of forest vegetation compared to shrub and herbs. Additionally, perhaps west-facing aspects experience less variable temperatures and moisture regimes or bedrock bedding, jointing, or fracturing conducive to stability compared to other exposures (Carson and Kirby 1972; Fischer et al. 2006). When all landslides are considered, northern slopes exhibit growing landslide association while landslide frequency declines in southeastern slopes (Fig. 4.3a, b). North-facing slopes have been documented to retain more soil moisture than south-facing aspects in northern latitudes (Geroy et al., 2011). Hillslope asymmetry (i.e., steeper slopes depending on aspect) was not found during inspection of average slope on the four primary aspects; however, north-south asymmetry has been found to

demonstrate reversal based on elevation and at 49° latitude, which correspond to the northern edge of NOCA (Poulos et al., 2012). In general, the relatively similar aspect associations for different landslide observation datasets likely indicates the connection of source areas to downstream processes of transport and deposition (Fig. 4.1).

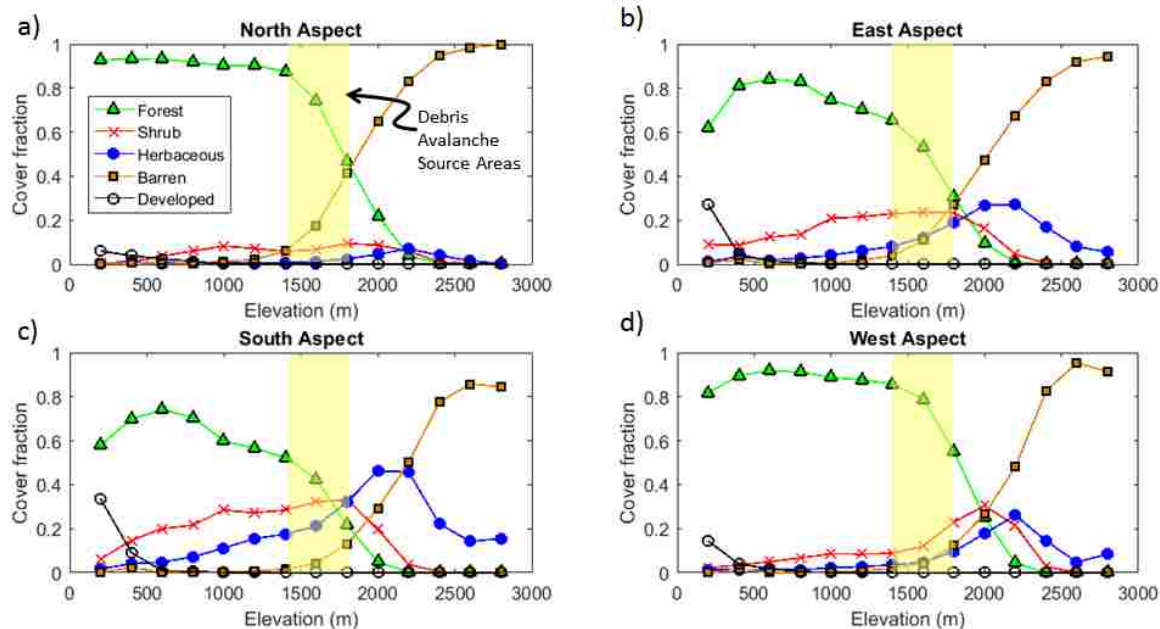


Figure 4.4 - Vegetation cover fraction in NOCA on each aspect, taken as the fraction of vegetation type within each 200-m elevation band. Aspects categorized here as: **a)** north (0° to 45° and 315° to 360°), **b)** east (45° to 135°), **c)** south (135° to 225°), and **d)** west (225° to 315°), covering 23%, 23%, 26%, and 28% of NOCA, respectively. Yellow highlighted area represents the strongest elevation association for debris avalanche source areas.

In our study domain, glacial patterns may also influence slope predisposition to failure, particularly when considering all landslide types. Glaciers preferentially grow on poleward-facing slopes where shade and radiation incidence increase glacier mass balance (Evans 2006) and expose oversteepened slopes after glacier recession, often with minimal vegetation during the first 60 years post deglaciation (Ballantye and Benn 1994; Moore et al. 2008; Pelto 2015; Whelan and Bach 2017; Haeberli et al. 2016). Because of the linkage between aspect and slope, and the influence of these factors on vegetation and moisture, an index representing the solar heating from incident radiation may be a worthwhile attribute to assess landslide frequency. Either the heat load index (McCune et al. 2002) or the diurnal anisotropic heating index (Cristea et al., 2017; Böhner and Antonić, 2009) could be used as a SA in future landslide assessments. It has also been suggested that landslides generally occur on slopes perpendicular to the general physiographic trend of mountains (Gokceoglu et al. 2005). Our finding of a preponderance of landslide initiation on east-facing aspects supports this theory given the north-south orientation of the North Cascades mountain range.

Comparisons among all landslides, whole debris avalanches, and debris avalanche source areas clearly show that unconsolidated sediments, largely derived from transport and depositional processes, have stronger association with landslides than other lithologies followed by sedimentary rock. This strong association is expected given the inclusion of mass wasting landforms in the classification of unconsolidated sediment. The high ultramafic rock association

when considering all landslide types is driven by a single topple/fall occurring in this scarce lithology (<0.02% of NOCA). With the source areas of debris avalanches, all lithologies except for ultramafic rocks produce slides. Widespread observation of debris avalanche source areas in all rock types may indicate a large influence of slope steepness on landslide initiation regardless of lithology. For debris avalanche processes, sedimentary rock is more associated with transport and depositional areas than source areas. Areas without landslide activity were associated with weak metamorphic foliated and intrusive igneous lithology (Fig. 4.3a).

The association of landslides on concave/converging versus convex/diverging topography is relatively consistent among the datasets and generally consistent with literature due to enhanced wetness where vegetative support may be weak in deeper soils (see Hales et al. 2009; Fig. 4.3). High wetness index is associated with landslides for all landslide types as well as entire debris avalanches (Fig. 4.3a, b). This result is intuitive as this index is an indicator of increased soil saturation and surface runoff. In contrast, source areas were correlated with low wetness index (Fig. 4.3c). As previously discussed, source areas are associated with steep slopes and higher elevations, resulting in relatively small specific catchment areas. By definition, wetness index is negatively correlated with slope and positively correlated with specific contributing area. Thus, source areas will have a low wetness index when they are from steep slopes with small contributing areas (i.e., located higher up on hillslopes).

4.3.2 Susceptibility Index

A susceptibility index (SI) is calculated for each grid cell within the study area domain by summing FR for each SA. The resulting spatial distribution of SI is right skewed and bimodal when considering all landslide types as well as debris avalanches (Fig. 4.5a, b). The right skew indicates that there is a small population of grid cells with high SI compared to the majority. The first mode of the distribution ($SI \approx 7.0$) represents average conditions for landslide frequency given that we assess seven SAs. SA subcategories coinciding at the same location can have a substantial influence on the resulting SI. Unconsolidated sediment is often at the base of hillslopes, which coincides with lower elevation. Therefore, the high FR value for settings combining unconsolidated sediment and sedimentary rock lithology with elevation below 400 m largely drives the second (smaller) SI mode on the right. When considering only the source areas of debris avalanche dataset, the right skewness persists, while the shape of the distribution becomes unimodal. This suggests that the high FR subcategories do not coincide locally when examining source areas of debris avalanches (e.g., east and southeast aspects are not necessarily $>50^\circ$). For source areas, there is also a broader difference in the SI mode for all grid cells ($SI=6.5$) and for landslide cells ($SI=7.5$), compared to the two other datasets.

Cumulative distributions for SI, plotted as fraction of area of the study domain less than or equal to an SI value, show higher SI values for a given probability for landslide cells than for the entire study domain (Fig. 4.5). Additional support that these distributions are not equal is provided by the Kolmogorov-Smirnov test, which rejects the null hypothesis of equal distributions at $\alpha < 0.01$. The distributions show that the SI calculated from FR method can differentiate mapped landslide locations.

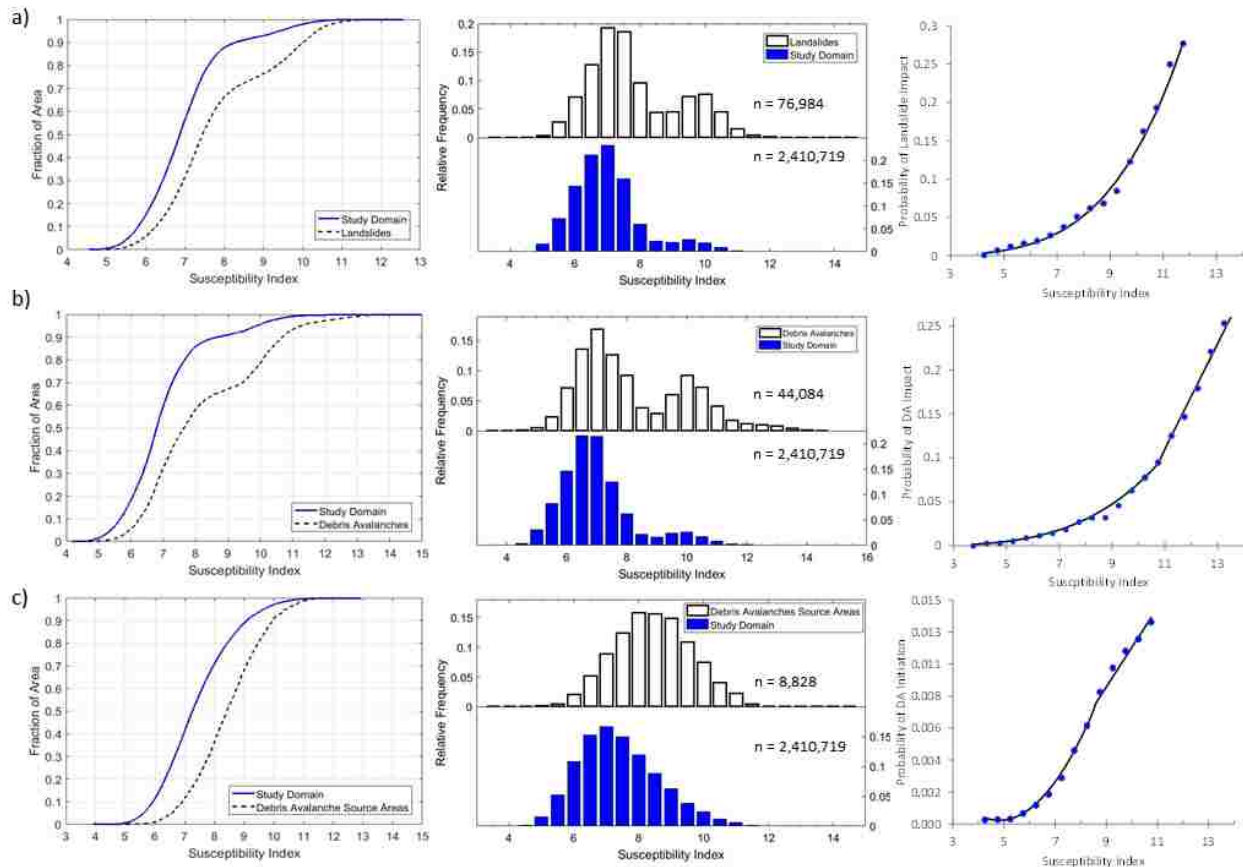


Figure 4.5 – Cumulative distributions (*column 1*) and relative frequency plots (*column 2*) of Susceptibility Index (SI) for all grid cells included in the analysis and the grid cells mapped as part of a mapped landslide. Probability $P(LS_r|SI_r)$ (*column 3*) calculated from the ratio of the number of landslide cells to the number of all cells with each SI bin (0.5 size) with fitted curves. Rows represent three analyses of mapped landslides: **a)** all landslide types, **b)** debris avalanches only, and **c)** debris avalanche source areas.

The probability of landslide impact ($P(LS_r|SI_r)$) calculated from Eq. (3) are shown in the last column of Fig. 4.5. In calculating this probability in each bin, landslide sample sizes of 40 or fewer were aggregated into the previous bin for the highest SI bins (e.g., $SI \geq 11$). In all three cases, $P(LS_r|SI_r)$ increases with SI, supporting the statistical power of this empirical approach. The SI - $P(LS_r|SI_r)$ relation is explained by a power function when all landslide data are used (Fig. 4.5a, *column c*). The other two cases, whole debris avalanche data and debris avalanche source areas, are better represented by piecewise relations that included polynomial and linear fits (all $R^2 > 0.96$). The range of probabilities in all cases vary considerably, and grows with the sample size of the landslide dataset used, leading to maximum probabilities of 0.30, 0.25, and 0.014, for all landslide, debris avalanches, and debris avalanche source areas, respectively. Nonlinear forms in the SI- $P(LS_r|SI_r)$ relations reveal the increased sensitivity of the landslides to relatively few SAs in this additive method. These functions were used to derive continuous empirical probability maps based on SI values assigned to each grid cell of the study domain. Mapped probabilities were limited to the maximum probability from Fig. 4.5.

4.3.3 Model Comparison

A key question of this research was: How can we combine empirical and physically-based models for landslide susceptibility to improve the prediction of landslide hazards? To address this question, we used the spatially distributed modeled probabilities of shallow landslide initiation $P(F)$ by Strauch et al. (2017) in NOCA. Their model solves the infinite slope stability equation coupled to a steady-state topographic flow routing approach using a Monte Carlo simulation that accounts for variable uncertainty. The uncertainty of soil depth in Strauch et al. (2017) was constrained by a soil development model, and subsurface flow recharge was obtained from a regional macro-scale hydrologic model that produced validated historical hydrologic simulations. The modeled probabilities are considered as annual probabilities of shallow landslide initiation (Strauch et al., 2017).

The physical model predicts the initiation of shallow landslides; therefore, we compared the mean probabilities of the physical model with the empirical probabilities developed from debris avalanche source areas. The models were compared on the basis of the SI bins developed for each dataset by averaging the physical model probabilities for grid cells within each SI bin. Through this comparison, our aim was to see how the physical model behaves in relation to the empirical classes of SI. Because the maximum probability was an order of magnitude higher for the physical model than the empirical model, we rescaled both probabilities by dividing by the highest probability from each model, resulting in a maximum normalized probability of 1.0 for each case, to facilitate comparisons between models. The highest mean probability for the physical model is 0.138 at $P(LS_r|SI_r)=8.75$; the highest probability for the empirical model is 0.0137 at $P(LS_r|SI_r)=11.0$ (Fig. 4.6a). Lower empirical probabilities are due to the limitation of landslide observations available in our source area dataset (i.e., small number of cells). In general, the two models are directionally consistent for $SI \leq 9.0$ (Fig. 4.6a, c). Both probabilities increase as SI increases up until about $SI=9.0$, above which the physical model mean probability declines (Fig. 4.6a).

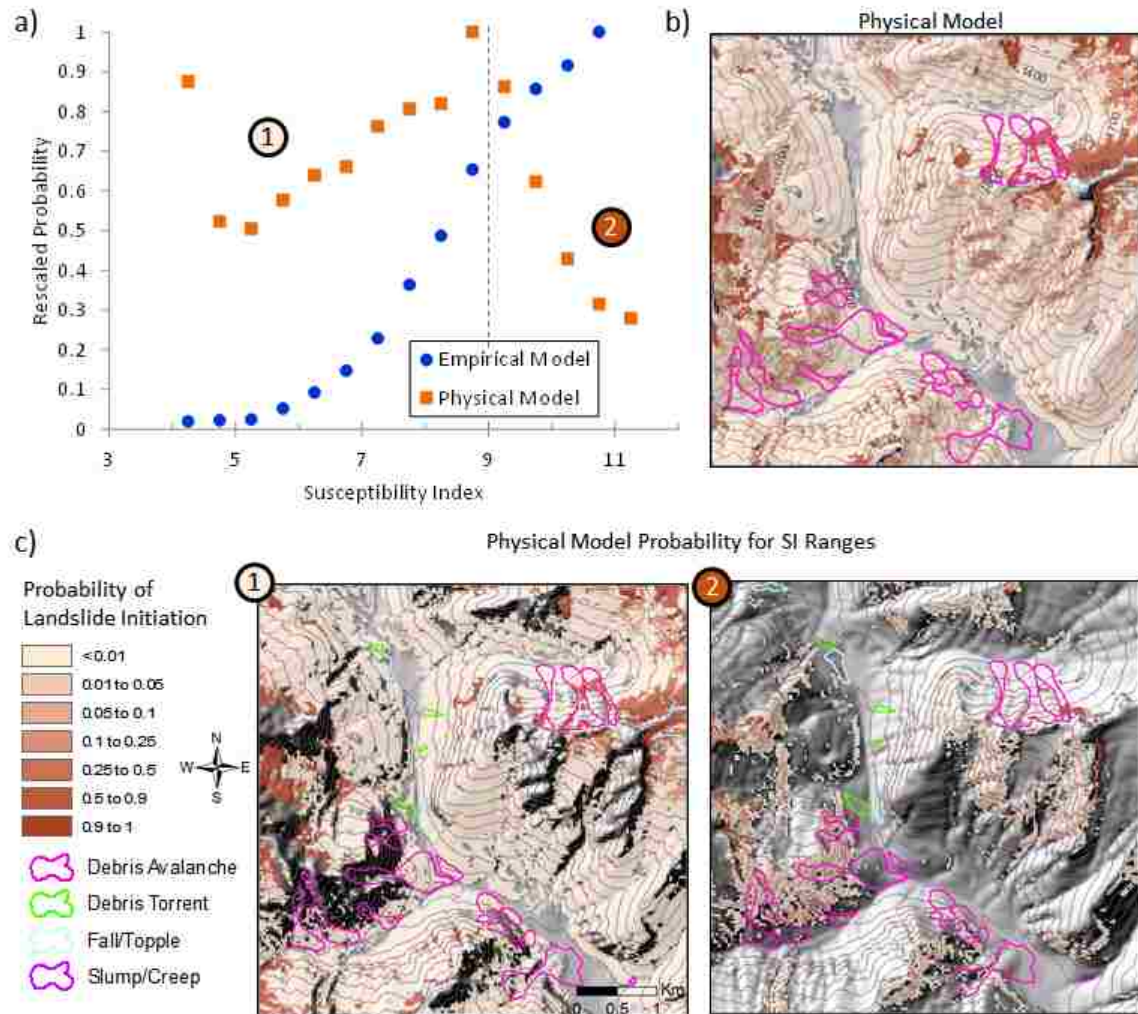


Figure 4.6 - **a**) Comparison of rescaled $P(LS_r|SI_r)$ from empirical model for debris avalanche source areas with the mean probability of landslide initiation $P(F)$ from the physical model within 0.5 size bins of SI (rescaled by dividing by maximum). Portion of NOCA showing: **b**) $P(F)$ from physical model; and **c**) same area showing only $P(F)$ corresponding to the two regions of SI (region 1: $SI \leq 9$; region 2: $SI > 9$, depicted in (a)) overlain on hillshade. Location of the portion of NOCA shown as box in Fig. 4.7.

To elucidate the divergence between probabilities at high SI values, we classified two regions of SI and examined the physical model $P(F)$ (Fig. 4.6b) within each region (Fig. 4.6c). Regions 1 and 2 cover 89% and 11% of the study domain, respectively. Areas in region 1 (Fig. 4.6a), where $SI \leq 9.0$ and physical model probabilities are on average higher than in region 2, have a mix of slopes, but typically are less steep than region 2. The wetness index in region 1 is higher and vegetation is predominantly forest. Lithology is mostly a mix of hard metamorphic and intrusive igneous, with average (i.e., $FR \approx 1$) to low association with observed source areas. Areas where $SI > 9.0$ with relative low probabilities predicted by the physical model (region 2) have steep slopes ($>35^\circ$), low wetness index, and land cover composed of primarily herbaceous vegetation or barren. These characteristics lead to a high empirical SI based on the FR analysis. Lithology is mostly hard metamorphic, an average FR value in the empirical model, but a relatively competent underlying lithology (Riedel et al. 2012), suggesting that lithology may not be significantly related to landslide initiation in region 2.

A potential reason the physical model predicted lower probabilities on average in region 2 may be due to soil depth. Visual examination of overlain attribute rasters show region 2 overlaps with areas that have a thin veneer of soil and steep slopes. The median values of modeled soil depths in region 2 from Strauch et al. (2017) were typically shallow <0.5 m and most areas <0.1 m, generally consistent with the coarse-scale Soil Survey Geographic Database (SSURGO) (DOA-NRCS 2016) soil depth data. Thus, the thin soil may have insufficient mass to fail in the infinite slope model, but empirical evidence suggests that these areas may also be unstable. Other areas in region 1 where soils are also shallow like region 2, but the physical model probabilities are high, have gentler slopes (25 to 35°) than region 2, which could lead to reduced drainage and increased pore-water pressure during rainstorms or snow and ice melt sufficient to induce failure.

The physical model appeared to capture the initiation of landslides for almost 90% of the study domain in region 1 (Fig 4.6a). In region 2, despite the inverse dependence of the mean $P(F)$ to SI, the modeled probabilities of shallow landslide initiation are still nearly an order of magnitude greater than those empirically obtained from observations. Therefore, we hypothesize that physically modeled probabilities for landslide initiation better represent hazards of landslide initiation compared to the empirical-based probabilities obtained from SI, which were largely based on limited observations that may have missed mapping of landslide initiation areas.

In our effort to integrate the two models, next we illustrate the behavior of the mean $P(F)$ in relation to SI obtained from the whole landslide data set. Using the original probabilities (i.e., not rescaled), we found an almost inverse or mirror pattern in the probabilities from the physical and empirical models (both all landslide types and debris avalanches datasets) along the SI range (Fig. 4.7). This pattern suggests that the empirical model is effective at identifying hazard from the transport and depositional regions of landslides, while the physical model captures the initiation areas. Transport and deposition areas are identified through increasing SI driven by high FR values associated with low elevation, gentler slopes, and unconsolidated sediment lithology. Unconsolidated sediment lithology is a strong driver of the highest probability locations for these datasets and is commonly found at the base of valley walls and valley bottoms where deposition occurs.

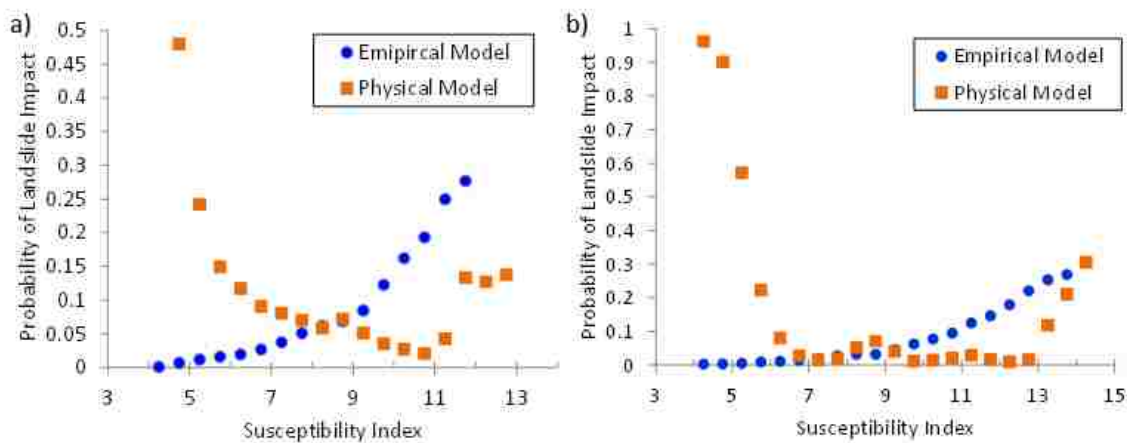


Figure 4.7 - Comparison of probabilities derived from empirical model for: **a)** all landslide types and **b)** debris avalanches overlain with the average probability from the physical model for grid cells within each 0.5 bins of SI.

4.3.4 Landslide Hazard Maps

Hazard maps were made in ArcGIS using the SI to $P(LS_r|SI_r)$ functions described in Sect. 4.3.2 and shown in Fig. 4.5 (*column 3*). In general, the probability of landslide impact declines as the amount of observational information decreases from all landslides (Fig. 4.8a), to debris avalanches (Fig. 4.8b), and debris avalanche source areas (Fig. 4.8c). This pattern reflects the smaller area of observed landslide data used in each case compared to the study domain. When considering all landslides, the highest probabilities are located near the base of valley walls and in topographic depressions or hollows (Fig. 4.8a). The hazard map developed from the empirical model using only debris avalanches (Fig 4.8b) also shows higher probabilities in the valley bottoms, but lower probabilities than the all landslides map at higher elevations in alpine areas where the footprint of debris avalanches is smaller compared to the deposition area, reducing the overall probabilities in the FR approach. Spatial patterns of landslide probabilities obtained from the source areas of debris avalanches (Fig. 4.8c) departs from the other two empirical models with the highest probabilities in middle and upper portions of valley walls, similar to the physical model (Fig. 4.9b).

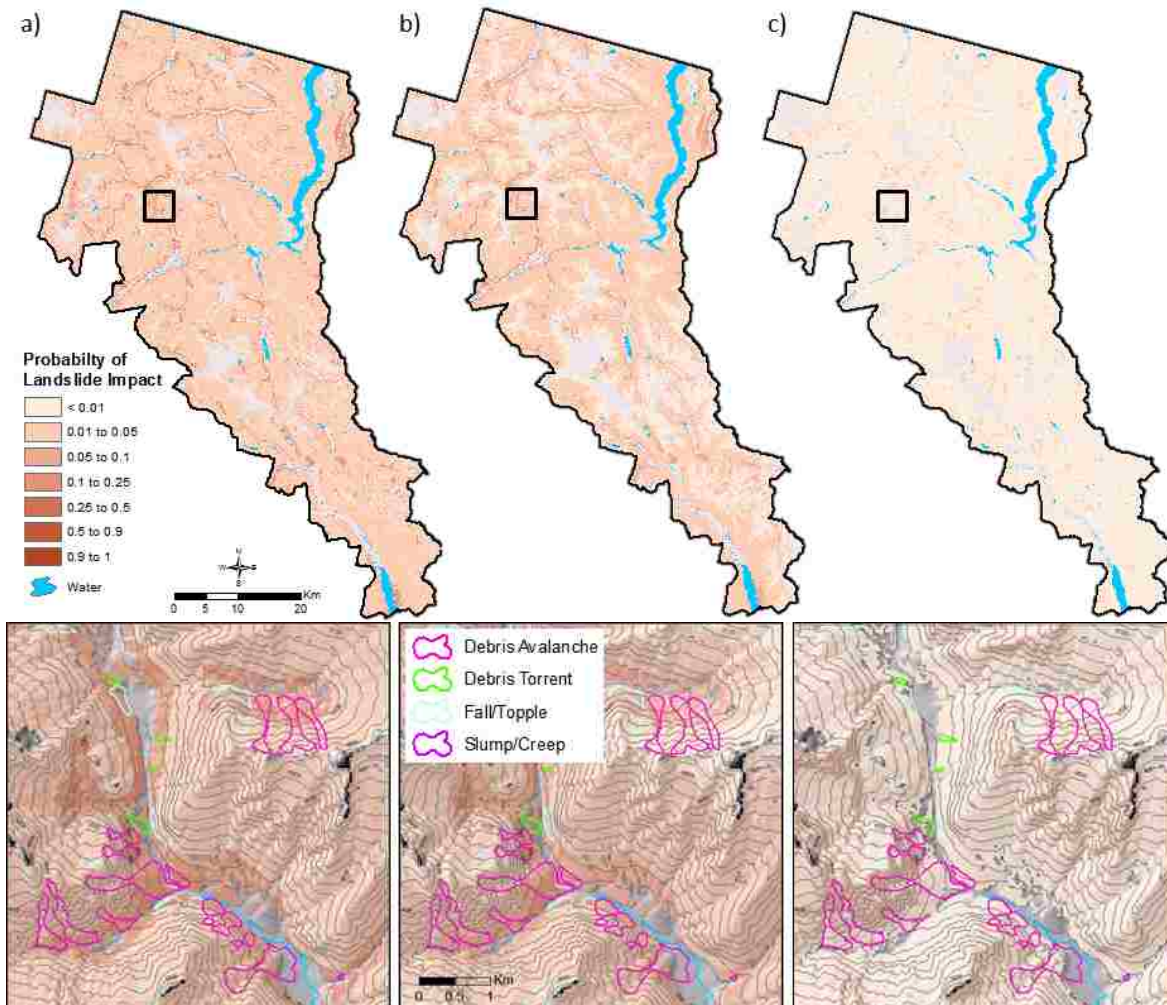


Figure 4.8 – Maps of probability of landslide impact derived from empirical model based on: **a)** all landslide types, **b)** debris avalanches, and **c)** and source areas of debris avalanches. Boxes indicates close-up areas shown below with overlain landslide types on hillshade. Gray areas excluded from analysis.

We developed an integrated landslide hazard map using the empirical model based on all landslides dataset and the physical probabilistic solution of the infinite slope stability model from Strauch et al., (2017) to obtain a probability of landslide impact that integrates initiation, transport, and deposition hazards of landslides. The physical model helps highlight the likely landslide initiation that are masked or missed in the empirical model approach because of the areal dominance and biased mapping of depositional areas. We combined the empirical model (Fig. 4.9a, 4.10a) with the physical model (Fig. 4.9b, 4.10b) by selecting the highest probability from either model within each grid cell that would represent both ends of the landslide hazard spectrum from initiation to depositional impact (Fig. 4.9c, 4.10c).

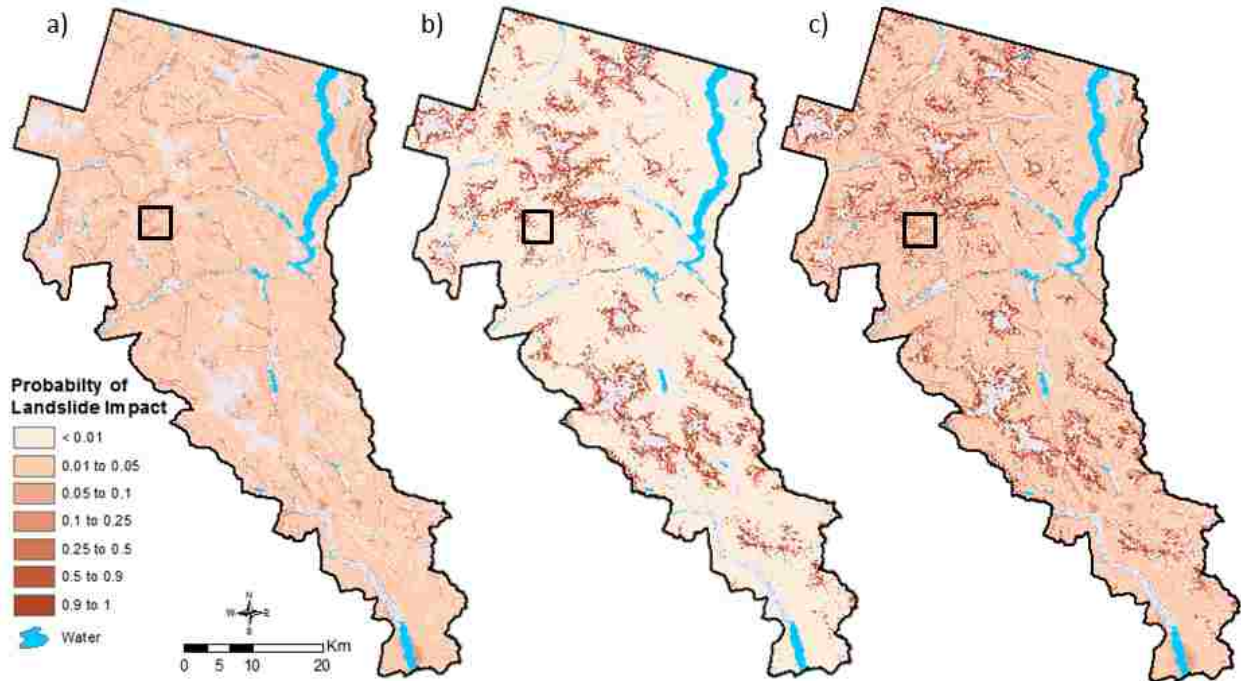


Figure 4.9 – Maps of probability of landslide impact based on: **a)** empirical model of all landslide types, **b)** physical model from Strauch et al. (2017), and **c)** integrated model for the North Cascades National Park Complex. Box indicates close-up locations in Fig. 4.10. Gray areas excluded from analysis and blue areas depict water.

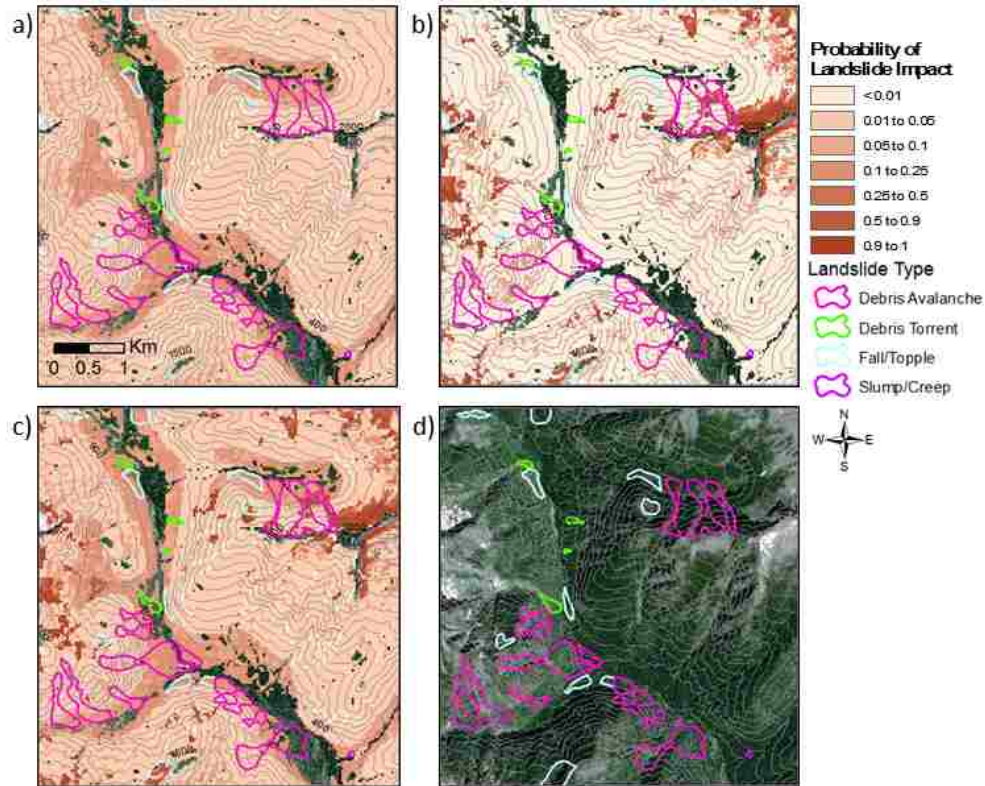


Figure 4.10 - Section of NOCA showing probability of landslide impact from: **a)** empirical model based on all landslide types, **b)** physical model, and **c)** integrated map derived from highest per pixel value from either empirical model (a) or physical model (b) overlain with mapped landslides; **d)** aerial image sourced from World Imagery, Esri Inc.² of same area overlain with landslides. Location shown as box in Fig. 4.9.

The integrated map shows high probability of landslide impacts in the alpine region below receding glaciers as well as at low elevations near the base of hillslopes that are likely deposition zones (Fig. 4.9c, 4.10c). Converging areas or hollows are also relatively higher probability, highlighting where soil and water can accumulate and lead to failure if steep enough and sparsely vegetated. In general, mid-slope valley walls appear to be the least likely to be impacted by landslides. These areas are typically heavily forested in NOCA (Fig. 4.10d), which can increase the root cohesion within the soils. The presence of forest also indicates that landslides are infrequent on much of the mid-slope areas with the exception of transport within narrow channels and snow avalanche tracks. Rocky outcrops are also present along these valley walls over steepened from the last glacial maximum (20 kya) and retaining too little soil for mass wasting processes and thus, have low probabilities.

To investigate the spatial distribution of model probabilities in the study domain and inside landslides, we plot the cumulative distribution of probabilities from the empirical model based on all landslides, the physical model (Strauch et al., 2017), and the integrated model (Fig. 4.11). When comparing between the study domain and inside landslides, the integrated model shows a higher fraction of landslide cells with higher probability than the study area as a whole, indicated

² Images created using ArcGIS® software by Esri. ArcGIS® and ArcMap™ are the intellectual property of Esri and are used herein under license. Copyright © Esri. All rights reserved. For more information about Esri® software, please visit www.esri.com.

by the shift in the cumulative distribution (red line) to the right (Fig. 4.11). The distributions generally show a high portion of the landscape has relatively low probability of landslide impact (<0.2), while a small portion has high probability of impact (>0.8), proportions depend on the model. The empirical model distributions for the study domain and landslides shows that all cells have $P(LS) \leq 0.3$, the model maximum. Of study domain cells, approximately 10% of the study domain has a probability greater than 0.06 and up to this maximum, whereas the same fraction of landslide cells has double the probability (~ 0.12). The integrated and physical model show the same fraction of the study domain above (0.12) and below (0.88) above a probability of 0.25 (Fig. 4.11a). Below this probability, a greater fraction of the physical model has lower probabilities than the integrated model. This reflects the increase in areas of low probability compared to the original physical model probabilities when including the transport and depositional processes captured by the empirical model in an integrated susceptibility map. In both plots (Fig. 4.11), the integrated model spatially expands the landslide hazard. For example, when the empirical model is considered, only 90% of the domain has probabilities less than or equal to 0.08, while the integrated model gives probabilities less than or equal to 0.4 for 90% of the domain. This is a considerable increase in risk of landslides when the two complementary approaches are combined.

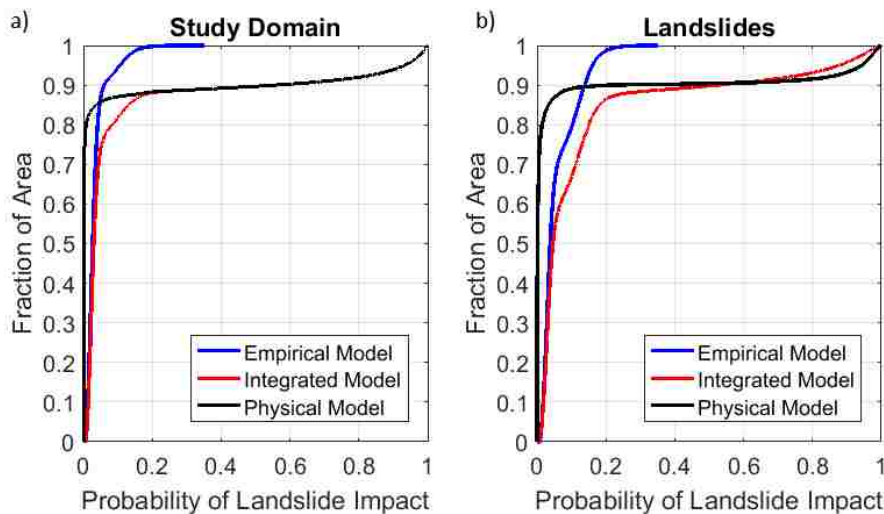


Figure 4.11 - Cumulative distribution of the probability of landslide impact $P(LS)$ for the empirical model using all landslide types (blue), the physical model (black), and the integrated model (red) for: **a)** all grid cells in study domain and **b)** grid cells inside landslides. Data for landslides curve for the physical model in (b) is limited to only debris avalanche source areas.

4.4 Conclusions

Empirically-based probability hazard maps were developed from a statistically-based susceptibility index, which integrated the influence of site attributes on observed landslides based on a frequency ratio approach. Resulting susceptibility depends on the observations of landslides considered: all types of landslides, debris avalanches only, or source areas of debris avalanches. A previously developed physically-based probabilistic map was combined with the empirical map based on all landslide types to produce an integrated overall probabilistic map of landslide hazard for initiation, transport, and deposition processes. The frequency analysis and hazard map development identified several key findings:

- Frequency analysis shows a clear and growing control of local slopes greater than 35° on landslide initiation, while higher landslide hazard at gentler slopes (<30°) reflects depositional processes.
- Debris avalanche source areas are associated with mid to high elevation (1,400 to 1,800 m), while all landslides types and whole debris avalanches have growing frequency in lower elevations (< 1,200 m) with the highest frequency falling in elevations < 400 m.
- Slope is a key attribute for the initiation of landslides, while lithology is mainly tied to transport and depositional processes.
- The transition from subalpine to alpine vegetation and barren lands (e.g., above forestline) with lower root cohesion leads to higher landslide frequency at debris avalanche source areas.
- East (west) aspect is a positive (negative) landslide-influencing factor, likely due to differences in forest cover and associated root cohesion and moisture.
- High association with landslides in developed areas, suggests a disproportionately high disruption of infrastructure compared to other land use-land covers.
- Empirical statistical modeling adjusts the probability of landslide impact based on physical mechanisms controlling landslide initiation by including additional information on factors that influence the landscape susceptibility to failure.

Although the approach is applicable elsewhere, our results from the FR analyses are specific to the region they were developed and may differ in another location with different lithology and landslide inventories. Additionally, the probabilities are likely to change as local conditions change from disturbance such as fire or as climate continues to change. We provide multiple landslide hazard maps for NOCA that land managers can use for planning and decision making, as well as educating the public about hazards from landslides so they can minimize risks from these geohazards.

Acknowledgements

This research was supported by the US National Science Foundation (CBET-1336725, OAC-1450412) and USGS Northwest Climate Science Center. Special thanks to Jon Riedel and Stephen Dorsch of North Cascades National Park Complex for categorizing the lithology, discussing local landslide processes, and providing electronic copies of landslide data and reports.

References

- Agee, J. K., & Kertis, J. (1987). Forest types of the north Cascades National Park Service complex. *Canadian Journal of Botany*, 65(7), 1520-1530.
- Anagnostopoulos, G. G., Fatichi, S., & Burlando, P. (2015). An advanced process- based distributed model for the investigation of rainfall- induced landslides: The effect of process representation and boundary conditions. *Water Resources Research*, 51(9), 7501-7523.
- Ayalew, L., Yamagishi, H., & Ugawa, N. (2004). Landslide susceptibility mapping using GIS-based weighted linear combination, the case in Tsugawa area of Agano River, Niigata Prefecture, Japan. *Landslides*, 1(1): 73-81.
- Ballantyne, C. K., & Benn, D. I. (1994). Paraglacial slope adjustment and re-sedimentation following recent glacier retreat, Fåbergstølsdalen, Norway. *Arctic and Alpine Research*, 255-269.

- Baum, R.L., Galloway, D.L., and Harp, E.L. (2008) Landslide and land subsidence hazards to pipelines: U.S. Geological Survey Open-File Report 2008-1164, 192 p.
- Baum, R.L., Schulz, W.H., Brien, D.L., Burns, W.J., Reid, M.E., and Godt, J.W. (2014). Plenary: Progress in Regional Landslide Hazard Assessment—Examples from the USA, In: *Landslide Science for a Safer Geoenvironment*, Springer International Publishing, 21-36.
- Beatty, C.B. (1956) Landslides and Slope Exposure. *The Journal of Geology*. 64:1.
- Bellugi, D., Milledge, D.G., Dietrich, W.E., Perron, J.T., and McKean, J. (2015). Predicting shallow landslide size and location across a natural landscape: Application of a spectral clustering search algorithm. *Journal of Geophysical Research: Earth Surface*, 120(12): 2552-2585.
- Beven, K. J., & Kirkby, M. J. (1979). A physically based, variable contributing area model of basin hydrology. *Hydrological Sciences Journal*, 24(1): 43-69.
- Böhner, J., & Antonić, O. (2009). Land-surface parameters specific to topo-climatology. *Developments in Soil Science*, 33: 195-226.
- Bordoni, M., Meisina, C., Valentino, R., Bittelli, M., and Chersich, S. (2015). Site-specific to local-scale shallow landslides triggering zones assessment using TRIGRS, *Natural Hazards & Earth System Sciences*, 15(5): 1025-1050.
- Borga, M., Fontana, G.D., and Cazorzi, F.: Analysis of topographic and climatic control on rainfall-triggered shallow landsliding using a quasi-dynamic wetness index. *Journal of Hydrology*, 268(1): 56-71, 2002.
- Carrara, A., M. Cardinali, F. Guzzetti, and Reichenback, P. (1995). GIS technology in mapping landslide hazards. In: Carrara, A. and F. Guzzetti (eds.) *Geographical Information System in Assessing Natural Hazard*. Kluwer, New York, 107-134 pp.
- Carson, M. A., and M. J. Kirkby (1972). *Hillslope Form and Process*, Cambridge Univ. Press, Cambridge, U.K., 475 pp.
- Cevasco, A., Pepe, G., & Brandolini, P. (2014). The influences of geological and land use settings on shallow landslides triggered by an intense rainfall event in a coastal terraced environment. *Bulletin of Engineering Geology and the Environment*, 73(3): 859-875.
- Chalkias, C., Ferentinou, M., & Polykretis, C. (2014). GIS-based landslide susceptibility mapping on the Peloponnese Peninsula, Greece. *Geosciences*, 4(3), 176-190.
- Chung, C. J. F., & Fabbri, A. G. (2003). Validation of spatial prediction models for landslide hazard mapping. *Natural Hazards*, 30(3), 451-472.
- Coe, J. A. (2016). Landslide hazards and climate change: A perspective from the United States. In: *Slope safety preparedness for impact of climate change*, Chapter: 14. (Eds.) K. Ho, S. Lacasse, L. Picarelli. CRC Press, Boca Raton, FL., 479-523 pp.
- Collins, B. D., & Montgomery, D. R. (2011). The legacy of Pleistocene glaciation and the organization of lowland alluvial process domains in the Puget Sound region. *Geomorphology*, 126(1): 174-185.
- Corominas, J., Van Westen, C., Frattini, P., Cascini, L., Malet, J. P., Fotopoulou, S., ... & Pitilakis, K. (2014). Recommendations for the quantitative analysis of landslide risk. *Bulletin of engineering geology and the environment*, 73(2): 209-263.
- Cristea, N. C., Breckheimer, I., Raleigh, M. S., HilleRisLambers, J. and Lundquist, J. D. (2017). An evaluation of terrain-based downscaling of fractional snow covered area datasets based on Lidar-derived snow data and orthoimagery. *Water Resour. Res.*. Accepted Author Manuscript. doi:10.1002/2017WR020799
- Croke, J. C., & Hairsine, P. B. (2006). Sediment delivery in managed forests: a review. *Environmental Reviews*, 14(1), 59-87.
- Crozier, M. J. (2010). Deciphering the effect of climate change on landslide activity: A review. *Geomorphology*, 124(3): 260-267.
- Dai FC, Lee CF (2002) Landslide characteristics and slope instability modeling using GIS, Lantau Island, Hong Kong. *Geomorphology* 42:213–228
- Densmore, A.L., R.S. Anderson, B.G. McAdoo, and M.A. Ellis, (1997). Hillslope evolution by bedrock landslides, *Science*, 275: 369-372.

- Evans, I. S. (2006). Local aspect asymmetry of mountain glaciation: a global survey of consistency of favoured directions for glacier numbers and altitudes. *Geomorphology*, 73(1): 166-184.
- Evans, R. D., & Fonda, R. W. (1990). The influence of snow on subalpine meadow community pattern, North Cascades, Washington. *Canadian Journal of Botany*, 68(1): 212-220.
- Fischer, L., Käab, A., Huggel, C., & Noetzli, J. (2006). Geology, glacier retreat and permafrost degradation as controlling factors of slope instabilities in a high-mountain rock wall: the Monte Rosa east face. *Natural Hazards and Earth System Science*, 6(5): 761-772.
- Gabet, E. J. (2003). Sediment transport by dry ravel. *Journal of Geophysical Research: Solid Earth*, 108(B1).
- Geroy, I. J., M. M. Gribb, H. P. Marshall, D. G. Chandler, S. G. Benner, and J. P. McNamara. (2011). Aspect influences on soil water retention and storage. *Hydrological Processes*, 25, 3836–3842, doi:10.1002/hyp.8281.
- Ghirotti, M. (2012). The 1963 Vaiont landslide, Italy. In: J.J. Claque and D. Stead (eds.) *Landslides: Types, mechanisms and modeling*. Cambridge University Press, NY., 359 pp.
- Gokceoglu, C., Sonmez, H., Nefeslioglu, H. A., Duman, T. Y., & Can, T. (2005). The 17 March 2005 Kuzulu landslide (Sivas, Turkey) and landslide-susceptibility map of its near vicinity. *Engineering Geology*, 81(1): 65-83.
- Gupta, R. P., & Joshi, B. C. (1990). Landslide hazard zoning using the GIS approach—a case study from the Ramganga catchment, Himalayas. *Engineering geology*, 28(1): 119-131.
- Haeberli, W., Schaub, Y., Huggel, C. (2016). Increasing risks related to landslides from degrading permafrost into new lakes in de-glaciating mountain ranges. *Geomorphology*: <https://doi.org/10.1016/j.geomorph.2016.02.009>.
- Hales, T. C., C. R. Ford, T. Hwang, J. M. Vose, and L. E. Band (2009). Topographic and ecologic controls on root reinforcement, *J. Geophys. Res.*, 114, F03013, doi:10.1029/2008JF001168.
- Haugerud, R.A., and Tabor, R.W. (2009). *Geologic map of the North Cascade Range, Washington, US* Department of the Interior, US Geological Survey, 29 pp.
- Hong, H., Chen, W., Xu, C., Youssef, A. M., Pradhan, B., & Tien Bui, D. (2017). Rainfall-induced landslide susceptibility assessment at the Chongren area (China) using frequency ratio, certainty factor, and index of entropy. *Geocarto International*, 32(2): 139-154.
- Hungr, O., Leroueil, S., & Picarelli, L. (2014). The Varnes classification of landslide types, an update. *Landslides*, 11(2): 167-194.
- Jin, S, Yang L, Danielson P, Homer C, Fry J, and Xian, G. (2013). A comprehensive change detection method for updating the National Land Cover Database to circa 2011, *Remote Sensing of Environment*, 132: 159-175.
- Kelsey, H.M. (1988). Formation of inner gorges, *Catena*, 1 5: 433-458.
- Kirschbaum, D.B., R. Adler, Y. Hong, S. Kumar, C. Peters-Lidard, and Lerner-Lam, A. (2012). Advances in landslide nowcasting: evaluation of global and regional modeling approach. *Environ. Earth. Sci.* 66: 1683-1696.
- LaHusen, S. R., Duvall, A. R., Booth, A. M., & Montgomery, D. R. (2016). Surface roughness dating of long-runout landslides near Oso, Washington (USA), reveals persistent postglacial hillslope instability. *Geology*, 44(2): 111-114.
- Lee, S. (2005). Application of logistic regression model and its validation for landslide susceptibility mapping using GIS and remote sensing data. *International Journal of Remote Sensing*, 26(7), 1477-1491.
- Lee S, Ryu J-H, Kim I-S. (2007). Landslide susceptibility analysis and its verification using likelihood ratio, logistic regression, and artificial neural network models: Case study of Youngin, Korea. *Landslides* 4:327–338.
- Lee S, Pradhan B. (2007). Landslide hazard mapping at Selangor, Malaysia using frequency ratio and logistic regression models. *Landslides* 4:33–41.
- Lepore, C., Kamal, S. A., Shanahan, P., & Bras, R. L. (2012). Rainfall-induced landslide susceptibility zonation of Puerto Rico. *Environmental Earth Sciences*, 66(6): 1667-1681.

- May, C.L., Pryor, B., Lisle, T.E., Lang, M. (2009). Coupling hydrodynamic modeling and empirical measures of bed mobility to predict the risk of scour and fill of salmon redds in a large regulated river. *Water Resources Research* 45: W05402.
- McCune, B., & Keon, D. (2002). Equations for potential annual direct incident radiation and heat load. *Journal of Vegetation Science*, 13(4): 603-606.
- Megahan, W.F., N.F. Day, and T.M. Bliss. (1978). Landslide occurrence in the western and central Northern Rocky Mountain physiographic province in Idaho, in *Forest Soils and Land Use: Proceedings of the Fifth North American Forest Soils Conference* (edited by C.T. Youngberg), CSU, Ft. Collins, CO, 116-139 pp.
- Miller, D. J., and Burnett, K. M. (2007). Effects of forest cover, topography, and sampling extent on the measured density of shallow, translational landslides: *Water Resources Research*, v. 43, no. W03433.
- Montgomery, D. R. (1994). Road surface drainage, channel initiation, and slope instability. *Water Resources Research*, 30(6): 1925-1932.
- Montgomery, D.R. (2001). Slope distributions, threshold hillslopes, and steady-state topography. *American Journal of science*, 301(4-5): 432-454.
- Moore, R. D., Fleming, S. W., Menounos, B., Wheate, R., Fountain, A., Stahl, K., ... & Jakob, M. (2009). Glacier change in western North America: influences on hydrology, geomorphic hazards and water quality. *Hydrological Processes*, 23(1): 42-61.
- Mustoe, G. E., & Leopold, E. B. (2014). Paleobotanical evidence for the post-Miocene uplift of the Cascade Range. *Canadian Journal of Earth Sciences*, 51(8): 809-824.
- O'loughlin, E. M.: Prediction of surface saturation zones in natural catchments by topographic analysis. *Water Resources Research*, 22(5): 794-804, 1986.
- Pachauri, A. K., & Pant, M. (1992). Landslide hazard mapping based on geological attributes. *Engineering geology*, 32(1-2), 81-100.
- Pack R.T., Tarboton, D.G., and Goodwin, C.N. (1998). The SINMAP approach to terrain stability mapping. In: *Proceedings of the 8th international congress of the international association of engineering geology and the environment*, Vancouver, British Columbia, Canada, September 21–25, vol 2. AA Balkema, Rotterdam, pp 1157–1165.
- Pelto, M. (2015). *Climate driven retreat of mount baker glaciers and changing water resources*. Springer International Publishing, Switzerland.
- Pelto MS, Riedel J (2001). Spatial and temporal variations in annual balance of North Cascade glaciers, Washington 1984–2000. *Hydrol Process* 15: 3461–3472.
- Pollock, M. M. (1998). Biodiversity, In: R. J. Naiman and R. E. Bilby (eds.) *River Ecology and Management: Lessons From the Pacific Coastal Ecoregion*, Springer-Verlag, New York. 430–452 pp.
- Poulos, M. J., J. L. Pierce, A. N. Flores, and S. G. Benner (2012). Hillslope asymmetry maps reveal widespread, multi-scale organization, *Geophys. Res. Lett.*, 39, L06406, doi:10.1029/2012GL051283.
- Riedel, J., S. Dorsch, and J. Wenger. (2012). *Geomorphology of the Stehekin River watershed: Landform mapping at North Cascades National Park Service Complex, Washington*. Natural Resource Technical Report NPS/NCCN/NRTR—2012/566. National Park Service, Fort Collins, Colorado.
- Riedel, J, and Prohala, J. (2005). Mapping ecosystems at the landform scale in Washington state, *Park Science* 23-2: 37-42.
- Roe, G.H. (2005). Orographic Precipitation. *Annu. Rev. Earth Planet. Sci.*, 33:645–71.
- Sidle, R.C., and Ochiai, H. (2006). *Landslides: processes, prediction, and land use*, Water Resources Monogram 18, American Geophysical Union, Washington DC.
- Strauch, R., Istanbuluoglu, E., Nudurupati, S. S., Bandaragoda, C., Gasparini, N. M., and Tucker, G. E. (2017). A hydro-climatological approach to predicting regional landslide probability using Landlab, *Earth Surf. Dynam. Discuss.*, <https://doi.org/10.5194/esurf-2017-39>, (in review).

- Swanson, F. J., and Dyrness, C. T. (1975). Impact of clear-cutting and road construction on soil erosion by landslides in the western Cascade Range, Oregon, *Geology*, 3: 393-396.
- Taylor, F.A., and Brabb, E.E. (1986). Map showing landslides in California that have caused fatalities or at least \$1,000,000 in damages from 1906 to 1984: U.S. Geological Survey Miscellaneous Field Studies Map, MF- 1867, scale: 1:1,000,000.
- United States Department of Agriculture, Natural Resources Conservation Service (DOA-NRCS). (2016). United States Department of Agriculture. Web Soil Survey. Available from: <http://websoilsurvey.nrcs.usda.gov/>. (Accessed 23 January 2017).
- United States Department of the Interior, National Park Service (DOI-NPS). (2012). Foundation Document, North Cascades National Park Complex, Washington. Available from: https://www.nps.gov/noca/learn/management/upload/North-Cascades-NP-Complex-Foundation-Document_small.pdf (Accessed 23 January 2017).
- United States Geological Survey (USGS). (2014a). National Elevation Data last modified March 6, 2014, National Map Viewer (Accessed 24 November 2014).
- USGS (2014b). National Land Cover Data (NLCD) version Marched 31, 2014, National Map Viewer (Accessed 25 November 2014).
- Van Westen, C.J., Van Asch, T.W., and Soeters, R. (2006). Landslide hazard and risk zonation—why is it still so difficult? *Bulletin of Engineering geology and the Environment*, 65(2): 167-184.
- Wartman, J., Montgomery, D.R., Anderson, S.A., Keaton, J.R., Benoit, J., dela Chapelle, J., and Gilbert, R. (2016). The 22 March 2014 Oso landslide, Washington, USA. *Geomorphology*, 253: 275-288.
- Washington State Department of Natural Resources (WADNR). (2014) *Geologic_unit_poly_100k*. Vector digital data, published June 2010. Division of Geology and Earth Resources, Olympia, WA [Accessed March 27, 2014].
- Whelan, P., & Bach, A. J. (2017). Retreating Glaciers, Incipient Soils, Emerging Forests: 100 Years of Landscape Change on Mount Baker, Washington, USA. *Annals of the American Association of Geographers*, 107(2): 336-349.
- Wooten, R. M., Witt, A. C., Miniati, C. F., Hales, T. C., & Aldred, J. L. (2016). Frequency and magnitude of selected historical landslide events in the southern Appalachian Highlands of North Carolina and Virginia: relationships to rainfall, geological and ecohydrological controls, and effects. In *Natural Disturbances and Historic Range of Variation* (pp. 203-262). Springer International Publishing.
- Wu, Z., Wu, Y., Yang, Y., Chen, F., Zhang, N., Ke, Y., & Li, W. (2017). A comparative study on the landslide susceptibility mapping using logistic regression and statistical index models. *Arabian Journal of Geosciences*, 10(8), 187.